STRATIFICATION AND CIRCULATION PRODUCED BY TURBULENT PLUMES

by

ALAN BUN DUEN WONG

A thesis submitted for the degree of

Doctor of Philosophy

of The Australian National University.

Research School of Earth Sciences

July 1998

Except where mentioned otherwise in the text or in the acknowledgements, the research described in this thesis is my own.

Alan B.D. Wong

Acknowledgements

I would like to thank my supervisors and advisors Dr Ross Griffiths, Dr Ross Kerr and Dr Rick Nunes-Vaz for their encouragement and advice throughout my candidature. Prof Stewart Turner also provided guidance during this time and his assistance is appreciated.

Dr Griffiths, who instigated the project, directed the research towards baroclinic modes in explaining the horizontal motions generated by a plume (chapter 4). I thank Dr James Rottman for allowing me to use his program to calculate the baroclinic normal modes and Dr Graham Hughes for showing me the method to calculate the dissipation of momentum due to viscous effects. I also thank Prof Turner for the many discussions which led to the likening of horizontally spreading downslope plumes to slumping gravity currents (chapter 5).

The research would not have been possible without the technical support of Mr Tony Beasley, Mr Derek Corrigan and Mr Ross Wylde-Browne. Mr Beasley constructed, modified and maintained the various tanks and accessories while Mr Corrigan demonstrated the use of the electronic equipment and software for data collection. Mr Wylde-Browne processed many rolls of film.

It has been a pleasure working in the Geophysical Fluid Dynamics group over the past three and a half years.

Members of the Geophysical Fluid Dynamics Group in December 1995.
Front row, left to right: Andrew Kiss, Alan Wong, Stewart Turner, Karen Buckley, Damien Bright, Ross Wylde-Browne.
Behind: Ross Griffiths, Nathalie Thomas, Derek Corrigan, Alison Leitch, Geoff Davies, Ross Kerr, Mark Jellinek, Tony Beasley, Roberto Weinberg.
I have also had the pleasure of the company of Lynn Bloomfield, Xavier Chavanne, Felicity Chivas, Graham Hughes, Louis Moresi, David Osmond, Sylvie Vergniolle, Ulla Wüllner and Matthew Wells who joined the GFD group between January 1996 and July 1998.

Abstract

This thesis examines the convection produced by turbulent plumes in confined regions. I extend the "filling-box" model of Baines and Turner (1969) to consider (i) the circulation patterns in the box, (ii) plumes that descend slopes, (iii) the interactions of multiple plumes and (iv) the modifications that result from overflows across a sill when the box is divided into two basins. A combination of theoretical models, analytical and numerical solutions and laboratory experiments is used. Each of the four extensions has relevance to processes in the oceanic thermohaline circulation.

The experiments show that when a turbulent plume forms a bottom outflow into a long tank, a series of counterflowing shear layers is generated. These layers are supported by the stable density stratification produced by the plume and are superimposed on the vertical advection and entrainment inflow of the "filling-box" circulation. The timescale for the velocity structure to adjust to changes in forcing is proportional to the time for long internal gravity waves to travel the length of the tank. I interpret these shear layers in terms of internal normal modes.

Models of plumes descending slopes are formulated and extended to include the resulting "filling-box" convection in confined regions. I develop a new streamtube model of the downslope plume that likens the slumping of the plume across the slope to the spreading of gravity currents. Analytical results show that this downslope plume has properties that have the same dependence on distance as those of a plume falling vertically far from side boundaries. Mixing between the plume and the environment depends on the angle of the slope. There is also experimental evidence that if mixing in the plume is thorough, as is the case for highly turbulent plumes on steep slopes in the laboratory, then

the "filling-box" circulation patterns in the environment are similar to those of the vertically-descending plume.

It is known that when two or more buoyancy sources produce well-separated plumes, the source with the largest buoyancy flux produces the plume that gives rise to the "bottom waters" while each plume from a source with a smaller buoyancy flux produces a mid-depth intrusion. I present a model for a number of buoyancy sources filling a single basin and give numerical solutions for the case of two sources. A large-time analytical approximation also shows that the spreading depth of the weaker plume is dependent on the two-thirds power of the ratio of the buoyancy fluxes of the two plumes. Experiments verify these results and also show that shear layers are present. The shear layers, which are primarily forced by the bottom outflow, influence the spreading of each intermediate depth outflow.

I also show that modifications to the plume and environment properties occur when the lower depths of the box are divided by a ridge to form a two-basin filling-box. In this system, each of the basins collects water separately with exchanges between the two basins possible only through an overflow over the ridge. I present numerical solutions which indicate that the inter-basin exchange of water is increasingly restricted as the ridge height grows, resulting in larger differences in the stratifications of the two basins. I also show that, depending on the relative cross-sectional areas of the two basins, the stratifications in the basins may become homogenous and overflows across the sill may reverse in direction.

Contents

1. Introduction **1**

2. Background on Turbulent Plumes and Internal Gravity Waves **4**

2.1 Preliminaries 4

2.2 Turbulent Plumes and Filling-Boxes 6

2.3 Internal Gravity Waves 16

3. Ocean Stratification and Circulation **21**

3.1 The Deep Ocean 21

3.2 Deep Water Formation and Outflows 24

3.3 Other Influences on Thermohaline Circulation 26

3.4 Motivation for the Current Research 28

4. Plume-Driven Shear Layers **29**

4.1 Introduction 29

4.2 Experiments 31

4.3 Results 34

4.4 Normal Modes 44

4.5 Discussion and Conclusion 55

5. Downslope Plumes **58**

5.1 Introduction 58

5.2 Two-Dimensional Downslope Plumes 59

5.3 Three-Dimensional Downslope Plumes 63

5.4 Experiments 69

5.5 Results 72

5.6 Discussion and Conclusion 75

6. Multiple Plume Systems 80

6.1 Introduction 80

6.2 "Filling-Box" Model for Multiple Plumes 80

6.3 Experiments 89

6.4 Results 91

6.5 Discussion and Conclusion 96

7. Two-Basin Systems 102

7.1 Introduction 102

7.2 Methodology 103

7.3 Single-Plume Systems 106

7.4 Two-Plume Systems 111

7.5 Discussion and Conclusion 123

8. Conclusions 125

References 128

Chapter 1

Introduction

In a body of fluid subject to gravity, variations in density lead to buoyancy forces that drive motions responsible for a large range of phenomena known in fluid mechanics. The present study is concerned with density driven flows where buoyant fluid is produced continuously in small, isolated regions and carried away in plumes which have large Reynolds numbers. Turbulent mixing between each plume and the environment occurs and the ensuing convection causes significant modifications to the properties of the plume and its surroundings.

The main aim of the present study is to explore and understand the fundamental dynamics in a small number of situations. These are simplified and idealised models of processes which may be relevant to the oceanic thermohaline circulation. The oceans are on the whole stably stratified with cold, dense waters at the bottom underlying warmer, less dense waters on top. Near the surface, exchanges of heat and fresh water with the atmosphere produce differences in density which can drive circulation between the surface and bottom waters. The sinking of surface waters to abyssal depths is known to occur at several localised regions, while the rising or upwelling to complete this circulation is distributed over most areas of the oceans (Robinson and Stommel, 1959). The deep ocean waters, therefore, originate from the regions of sinking and inherit the water properties there. These properties can be traced as the waters descend and spread to fill the interior of the oceans. It has been estimated that the timescale required for this cycle is 200-1800 years (Stommel and Arons, 1960). Various studies have also been conducted to quantify the changing properties of oceanic deep water sources (for example, Price and

O'Neil-Baringer, 1994) and their subsequent paths in the oceans (for example, Kawase, 1987).

The localised sources of deep water in the oceans have been likened to small sources of buoyancy in a confined region (Killworth, 1977). The convection and stratification produced by a single source of buoyancy in the so-called "filling-box" mechanism are well established (Baines and Turner, 1969; Killworth and Turner, 1982). The plume entrains surrounding water and falls vertically until it reaches its own density level or a horizontal boundary where it spreads out into the box. Convection brings plume water to all depths of the box and establishes a density gradient in the system. This "filling-box" mechanism, incorporating the vertical sinking, spreading of dense water and slow distributed upwelling, is the simplest model of the buoyancy-driven thermohaline circulation. The present study is concerned with extensions to this "filling-box" process to incorporate features of relevance to the oceans.

The approach incorporates both analytical and experimental investigations that complement one another. The established "filling-box" theory is an idealised analytical model in which the environment waters are assumed to be passively upwelled and entrained into the plume. However, the experiments described in chapter 4 show that when a plume produces an outflow in a stratified environment, internal gravity waves excite baroclinic normal modes to generate strong shearing motions in the convection. These shearing motions have little effect on the vertical structure produced by the "filling-box" mechanism and have not been detected by previous researchers. However, the shearing motions are important because they influence the paths taken by water masses circulating through the box. The shearing motions are examined and explained in terms of baroclinic normal modes for the non-linear "filling-box" stratification. The results may have applications in the oceans or enclosed seas, where the distribution of water properties and advection of tracers would be strongly affected if the sinking of deep water masses were to generate similar shear layers.

One of the major differences between oceanic deep water formation or sill overflows and unconstrained vertical plumes is that sinking waters in the oceans do not

fall vertically, but descend along slopes. The slope changes the shape of the plume and reduces mixing with the environment. Models of the downslope plume appear in chapter 5, and show that the properties of downslope plumes exhibit similar dependencies to those of the vertically-descending plumes. These similarities also extend to the "filling-box" process; however, experiments reveal that the slope may lead to a modified circulation pattern in certain situations.

An extension to the "filling-box" model to include a number of buoyancy sources of differing strengths is presented in chapter 6. The spreading depth of each plume is related to the stratification in the box that is produced collectively by all the plumes. Again, experiments validate and complement the theory and also reveal modifications to the spreading depths caused by the overshooting of plumes and the background shearing motions. The results are of interest to the thermohaline circulation, where the depths to which different outflows sink may potentially be predicted in terms of the relative buoyancy fluxes of the various sources driving the circulation.

In chapter 7, I consider the variations in the stratification and plume spreading depths that occur in a filling-box that has been divided into two basins by a vertical barrier. This system represents a simplification of the complex topographies, such as mid-ocean ridges and sills between marginal seas and ocean basins, that influence the oceanic circulation.

It should be noted that there are many other processes that affect the oceanic thermohaline circulation but are not considered in this study. It is not anticipated that any model of ocean circulation will result from the present study, but it is hoped that the extensions to the "filling-box" theory provide some insight into and possibly explain some of the features observed in the oceans. Chapters 2 and 3 review the previous work on turbulent plumes, filling-boxes, internal gravity waves and oceanic thermohaline circulation. Chapter 8 sums up the results presented in chapters 4, 5, 6 and 7.

Chapter 2

Background on Turbulent Plumes and Internal Gravity Waves

2.1 Preliminaries

Buoyancy forces arise when gravity acts in a body of water (or fluid) that contains variations in density in a horizontal plane. Where water of density different to its surroundings is continuously produced in some area, that area is referred to as a source of buoyancy. Gravity accelerates the buoyant water to produce a plume and if velocity and length scales are large enough to give a high Reynolds number, the plume is turbulent. Mixing between it and the surrounding water increases the volume flux and decreases the buoyancy of the plume. The plume ascends or sinks until it reaches water of its own density, or until it encounters a boundary. It spreads out and the turbulence dies as it becomes part of the non-turbulent environment. The convention used in this thesis is that the buoyancy source produces dense water so that the plume descends, but most of the details are also valid for ascending plumes of light water. In an environment that is horizontally bounded, but much wider than the plume itself, the plume is found to fill the environment in an orderly manner (Baines and Turner, 1969). In this situation, the injection of water into the confined environment pushes the overlying water higher and establishes a circulation that fills the environment with plume water. This circulation is known as the "filling-box" convection and establishes a stable stratification in the box (figure 2.1). A review of plume theory appears in §2.2.

In stratified bodies of water, buoyancy forces also act to generate waves. When an initially stable stratification is disturbed and a parcel of water is brought to a new depth

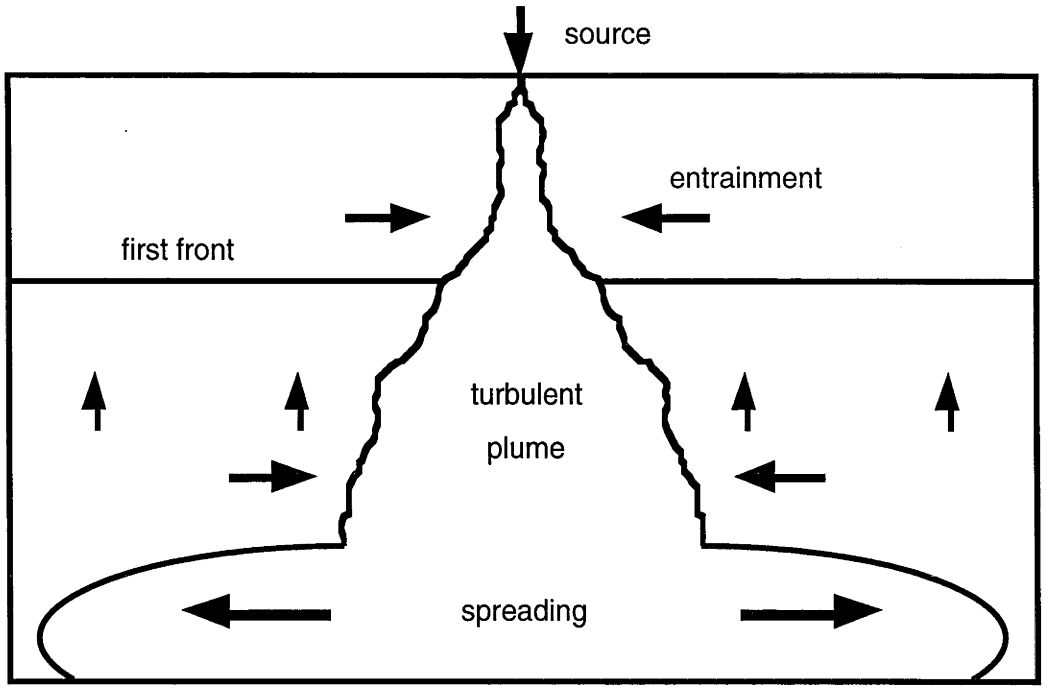

Figure 2.1. The motions in the plume and environment.

where the souroundings are of a different density, buoyancy forces act to accelerate it in the direction of its equilibrium position. For instance, if the parcel is brought higher to less dense surroundings, then the parcel is accelerated down towards its neutral density depth. The resulting motion can overshoot the equilibrium position and oscillate about it to give rise to internal gravity waves. As will be seen in §2.3, energy can propagate through the stratified body and lead to some surprising motions.

In this thesis both the y and z axes are used to represent the vertical coordinate. The y axis increases with height whereas the z axis increases with depth. The former is used for internal gravity wave theory while the latter is used for plume theory, in keeping with the respective directions of axes used in the literature.

Before continuing I present some definitions commonly used throughout this thesis. If g is the acceleration due to gravity, then the buoyancy force per unit mass of an element of water with density ρ in surroundings of density ρ_e is $g(\rho - \rho_e)/\rho_e$. If Q is the volume flux of dense water produced at a buoyancy source, then the (specific) buoyancy flux F of the source is defined as

$$F = g\frac{\rho - \rho_e}{\rho_e}Q.$$

The strength of a density gradient in a stably stratified environment is measured by the buoyancy frequency N. For an axis y which increases with height,

$$N = \left(-\frac{g}{\rho_e}\frac{d\rho_e}{dy}\right)^{1/2}.$$

Finally, the Reynolds number Re gives the relative importance of the inertial forces over the viscous terms in the equation of motion. If U is a typical velocity and L a typical length scale of a fluid with kinematic viscosity υ, then

$$Re = \frac{UL}{\upsilon}.$$

Motions with high Re are turbulent whereas those with low Re are laminar (smooth). Other less commonly used quantities will be defined when they are introduced.

2.2 Turbulent Plumes and Filling-Boxes

2.2.1 Theory

The model of turbulent convection from a localised source was first introduced by Morton et al. (1956). The main assumptions employed in the model are that:

(i) the rate of turbulent mixing (or entrainment) at the edge of the plume is proportional to some characteristic velocity at that depth (Taylor's entrainment hypothesis; Turner, 1986 and 1997),

(ii) the horizontal profiles of mean vertical velocity and density are of similiar form at all depths, and

(iii) the largest local variations of density are small in comparison with the overall density (the Boussinesq approximation).

The plume is assumed to be axisymmetric. At each depth z, its properties in the horizontal plane are averaged to give a top-hat profile. Let ρ_p, R and W be the density, radius and vertical velocity of the plume respectively, ρ_e the density of the surrounding water and ρ_r a reference density, taken to be that of the environment water at the source level. During its descent, the plume entrains surrounding water, thereby increasing in

radius and decreasing in density. The equations representing the conservation of volume, momentum and mass deficiency are

$$\frac{d}{dz}\left(\pi R^2 W\right) = 2\pi ERW,$$

$$\frac{d}{dz}\left(\pi R^2 W^2 \rho_r\right) = \pi R^2 g\left(\rho_p - \rho_e\right) \tag{2.1}$$

and

$$\frac{d}{dz}\left\{\pi R^2 W\left(\rho_p - \rho_r\right)\right\} = 2\pi ERW\left(\rho_e - \rho_r\right).$$

Here, E is the experimentally determined entrainment coefficient (Turner, 1986) and g the gravitational acceleration. For a source that has a buoyancy flux of $F = \pi R^2 W g(\rho_p - \rho_e)/\rho_r$ (evaluated at $z = 0$) which results in a plume that descends through a homogenous environment, Morton et al. (1956) calculated the solution to (2.1) as

$$R = \frac{6}{5} Ez,$$

$$W = \frac{5^{2/3} F^{1/3}}{2^{4/3} 3^{1/3} E^{2/3} \pi^{1/3}} z^{-1/3} \tag{2.2}$$

and

$$g\frac{\rho_p - \rho_e}{\rho_r} = \frac{5^{4/3} F^{2/3}}{2^{2/3} 3^{5/3} E^{4/3} \pi^{2/3}} z^{-5/3}.$$

They also obtained a numerical solution for a plume travelling through a uniformly stratified environment and conducted experiments that verified the theory. Their results were applied to the rise of smoke plumes in the atmosphere.

In the case of a plume descending in a confined environment the model was further developed by Baines and Turner (1969). If the box contains homogenous water initially, the plume reaches the bottom and spreads out in an outflow layer, the top of which forms the "first front", a discontinuity in density distinguishing the overlying homogenous water from water that has passed through the plume. The plume penetrates the first front and entrains water from below, resulting in a progressively denser outflow. A vertical advection is generated in the environment which lifts the first front and establishes a stable stratification in the box, giving rise to the so-called "filling-box"

convection. Equations representing conservation of volume and density in the environment are

$$AV = -\pi R^2 W \tag{2.3a}$$

and

$$\frac{d}{dt}\left(g\frac{\rho_e - \rho_r}{\rho_r}\right) = -V\frac{d}{dz}\left(g\frac{\rho_e - \rho_r}{\rho_r}\right). \tag{2.3b}$$

Here, V is the vertical velocity in the environment and A is the (constant) horizontal cross-sectional area of the box.

For the "filling-box" analysis it is henceforth assumed that buoyancy-driven convection is the dominant transport mechanism in the plume, whereas, far away from the plume, the only motions are those of passive advection. The assumption of a passive environment overlooks strong, active horizontal motions that are described later (chapter 4). However, these motions do not appear to significantly affect the plume or the density gradient it produces. Manins (1979) has also noted that in boxes of small aspect ratio (width/depth < 1.2) an inertial overturning motion is set up by the plume which mixes the environment water from top to bottom. I consider only much wider boxes. I also assume that the smallest horizontal dimension of the tank is larger than the diameter of the plume at the bottom so that the plume does not interact with the side walls of the tank.

The non-dimensionalisation scheme employed to reduce equations (2.1) and (2.3) to their simplest form for analysis is

$$\begin{aligned}
z &= H\zeta, \\
t &= A2^{-4/3}E^{-4/3}\pi^{-2/3}H^{-2/3}F^{-1/3}\tau, \\
R &= 2EHr, \\
W &= 2^{-2/3}E^{-2/3}\pi^{-1/3}H^{-1/3}F^{1/3}w, \\
g\frac{\rho_p - \rho_r}{\rho_r} &= 2^{-4/3}E^{-4/3}\pi^{-2/3}H^{-5/3}F^{2/3}f_p, \\
g\frac{\rho_e - \rho_r}{\rho_r} &= 2^{-4/3}E^{-4/3}\pi^{-2/3}H^{-5/3}F^{2/3}f_e, \\
V &= 2^{4/3}E^{4/3}\pi^{4/3}H^{5/3}F^{1/3}A^{-1}v,
\end{aligned} \tag{2.4}$$

where H is the height of the buoyancy source above the bottom. With these scalings, (2.1) becomes

$$\frac{d}{d\zeta}\left(r^2 w\right) = rw, \tag{2.5a}$$

$$\frac{d}{d\zeta}\left(r^2 w^2\right) = r^2\left(f_p - f_e\right) \tag{2.5b}$$

and

$$\frac{d}{d\zeta}\left(r^2 w f_p\right) = rwf_e, \tag{2.5c}$$

while (2.3) becomes

$$v = -r^2 w \tag{2.6a}$$

and

$$\frac{df_e}{d\tau} = -v\frac{df_e}{d\zeta}. \tag{2.6b}$$

An alternative form of (2.5c) is obtained by combining with (2.5a) to give

$$\frac{d}{d\zeta}\left\{r^2 w\left(f_p - f_e\right)\right\} = -r^2 w\frac{df_e}{d\zeta}. \tag{2.5c'}$$

It should be noted that Baines and Turner (1969) did not use a top-hat profile in their description of the plume, but rather a Gaussian profile defined by

$$w(z,r') = w(z)e^{-r'^2/b^2} \text{ and } g\frac{\rho_p - \rho_e}{\rho_r}(z,r') = g\frac{\rho_p - \rho_e}{\rho_r}e^{-r'^2/b^2}$$

where r' is the radial distance from the centre of the plume and b is a length scale. The Gaussian profile is a more realistic profile since the plume's velocity and buoyancy difference from the environment are maximal in the centre and diminish smoothly to blend into the environment. For reasons that will become clear in chapter 6, I have chosen the simpler top-hat profile. In using the Gaussian profile, the dimensional plume equations (2.1) are slightly different from those stated here (there is a factor of 1/2 in the left hand side of (2.1b) and (2.1c)) and result in a slightly different solution in the homogenous environment (2.2). However, once the equations for the Gaussian profile are non-dimensionalised (using slightly different scalings to (2.4)), the same dimensionless equations (2.5) and (2.6) are obtained.

The dimensionless solution to (2.5) is given by

$$r = \frac{3}{5}\zeta,$$

$$w = \frac{5^{2/3}}{2^{2/3}3^{1/3}}\zeta^{-1/3} \tag{2.7}$$

and

$$f_p - f_e = \frac{2^{2/3}5^{4/3}}{3^{5/3}}\zeta^{-5/3}.$$

Plots of r, w and f_p are given in figure 2.2. In the "filling-box" convection, the environment above the first-front is homogenous. If ζ_f is the position of the first front, then its velocity is given by $d\zeta_f/d\tau = v = -r^2w$. On substituting (2.7) and noting that $\zeta_f = 1$ when $\tau = 0$,

$$\zeta_f = \left(1 + \frac{2^{1/3}3^{2/3}}{5^{4/3}}\tau\right)^{-3/2}. \tag{2.8}$$

The progress of the first front is plotted in figure 2.3.

Baines and Turner (1969) obtained a power series solution to (2.5) and (2.6) in the large-time steady state where the plume's radius, vertical velocity and density difference to the environment do not vary at a given depth, but the plume and environment buoyancies steadily increase with time at all depths. In this description,

$$r(\zeta,\tau) = r'(\zeta),$$

$$w(\zeta,\tau) = w'(\zeta),$$

$$f_p(\zeta,\tau) = f_p'(\zeta) + \tau,$$

$$f_e(\zeta,\tau) = f_e'(\zeta) + \tau,$$

$$v(\zeta,\tau) = v'(\zeta),$$

and on dropping dashes, the equations to be solved are

$$\frac{d}{d\zeta}\left(r^2w\right) = rw, \tag{2.9a}$$

$$\frac{d}{d\zeta}\left(r^2w^2\right) = r^2\left(f_p - f_e\right), \tag{2.9b}$$

$$\frac{d}{d\zeta}\left\{r^2w\left(f_p - f_e\right)\right\} = -r^2w\frac{df_e}{d\zeta} \tag{2.9c}$$

a)

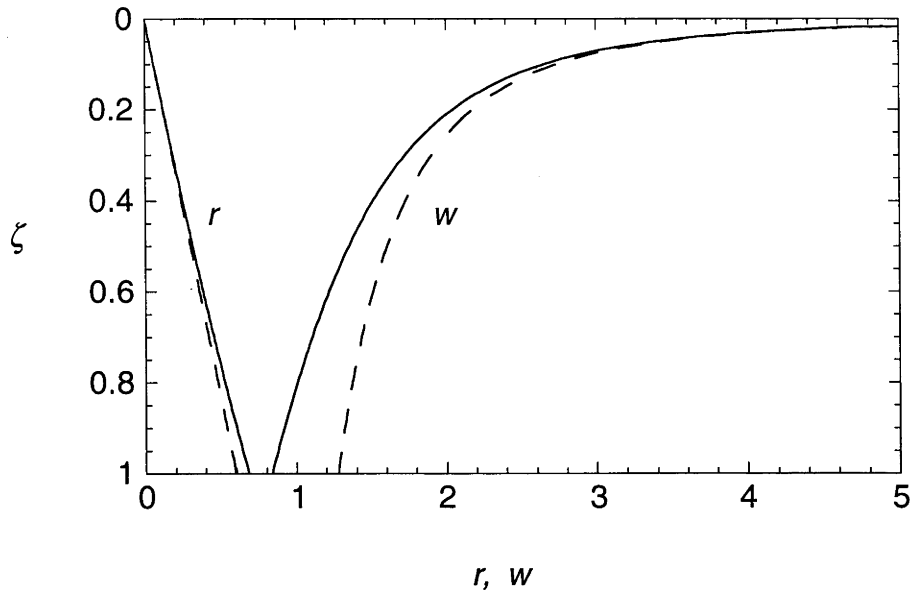

b)

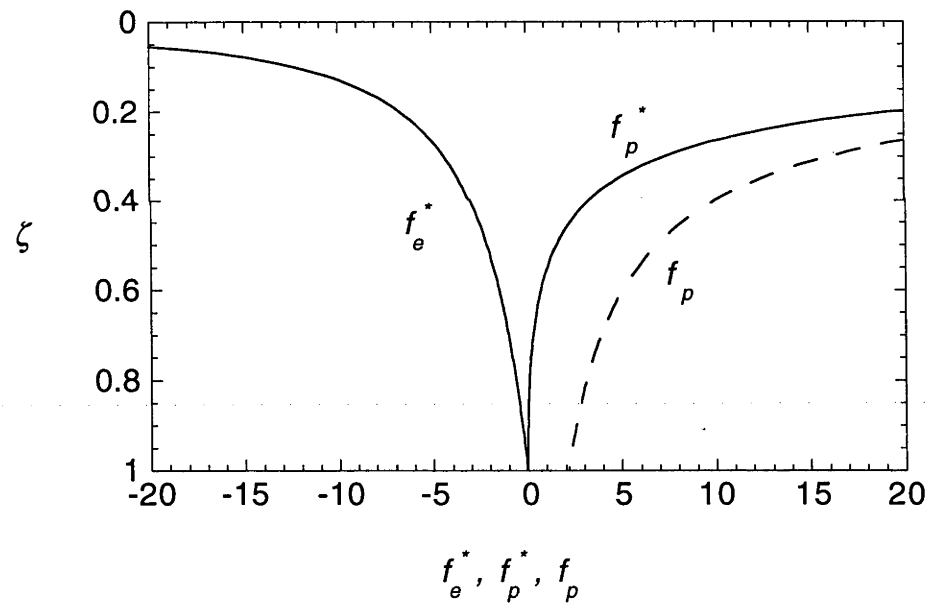

Figure 2.2. Plots of the plume properties for a plume in a homogenous environment (— — — —) and in the large-time steady state of the "filling-box" environment (————). The environment buoyancy for the latter is also plotted. (a) Plots of the plume radius r and velocity w in both environments. (b) The plume buoyancy f_p in the homogenous environment. In the "filling-box" environment, the steady-state plume buoyancy is plotted as an excess compared to the bottom, $f_p^* = f_p(\zeta) - f_p(1)$. Similarly, the steady-state environment buoyancy in the "filling-box" environment is plotted as $f_e^* = f_e(\zeta) - f_e(1)$.

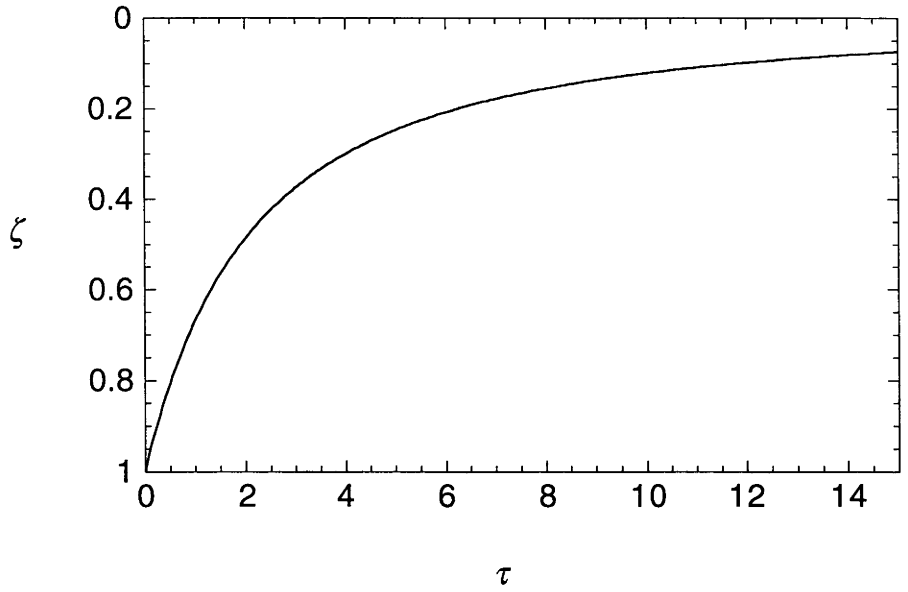

Figure 2.3. The position of the first front ζ_f plotted against time τ for the "filling-box" convection.

and

$$r^2 w \frac{df_e}{d\zeta} = -1. \tag{2.9d}$$

Equations (2.9c) and (2.9d) immediately give

$$\left(f_p - f_e\right) r^2 w = 1 - \zeta \tag{2.10}$$

so that the buoyancy flux falls linearly with depth, as it must if the environment is increasing in buoyancy at a constant rate. At the point source, $r^2 w = 0$ and $rw = 0$, while nearby (small ζ), the solutions to $r^2 w$ and rw are similar to that for an uniform environment (2.7). Power series solutions to $r^2 w$ and rw, calculated from the two equations obtained by substituting (2.10) into (2.9a) and (2.9b), are given by

$$r^2 w = 0.460\zeta^{5/3} - 0.0588\zeta^{8/3} - 0.0100\zeta^{11/3} + \ldots \tag{2.11a}$$

and

$$rw = 0.766\zeta^{2/3} - 0.157\zeta^{5/3} - 0.0366\zeta^{8/3} + \ldots. \tag{2.11b}$$

Both equations converge over the range of integration $0 \le \zeta \le 1$ and together give r and w. A further integration using (2.9d) gives

$$f_e = -\zeta^{-2/3}\left(3.27 - 0.837\zeta - 0.0623\zeta^2\right) + c. \qquad (2.12)$$

Equation (2.12) describes the functional dependence of the environment buoyancy f_e on depth and since f_e depends on how much buoyancy has been added to the system, the equation involves a term c that is linearly dependent on τ. The dependence on τ can be eliminated by considering $f_e^*(\zeta) = f_e(\zeta,\tau) - f_e(1,\zeta)$, that is, a buoyancy compared to the bottom that gives $f_e^*(1) = 0$. Similarly, the plume buoyancy can also be made independent of τ by considering $f_p^*(\zeta) = f_p(\zeta,\tau) - f_p(1,\tau)$. The plots of r, w, f_p^* and f_e^* obtained from (2.10), (2.11) and (2.12) are given in figure 2.2.

Baines and Turner (1969) also described experiments that confirm the theoretical solutions. They also found that as the first front passes through 90% of the tank, the stratification approaches that predicted by (2.12) and therefore the steady state is reached fairly quickly. The concluded that the properties of the plume and filling-box are dependent on the buoyancy flux of the source and not the density of the water coming from the source, so that if there are two or more sources, the one with the largest buoyancy flux will give rise to the bottom waters.

Several studies have extended the knowledge on plumes. The evolution of the stratification was numerically solved by Germeles (1975) while an approximate analytical solution was derived by Worster and Huppert (1982). Killworth and Turner (1982) studied the effect of time-varying buoyancy fluxes on the stratification (see below). Cardoso and Woods (1993) have looked at plumes in pre-stratified filling-boxes. Peterson (unpublished, personal communication) performed a study on two plumes of different strengths, but not using the "filling-box" method of this thesis. His study will be compared to my work on multiple plumes in chapter 6. The convection driven by plumes has also had various practical applications including the cumulus convection in the lower atmosphere (Squires and Turner, 1962), the filling of containers of liquefied natural gas (Germeles, 1975), turbulent flows down sloping boundaries in the oceans (Killworth and Turner, 1982), stratification in magma chambers (Turner, 1980) and ventilation in buildings (Cooper and Linden, 1996; Linden and Cooper, 1996).

2.2.2 The Entrainment Assumption

Central to the analysis of turbulent plumes is the assumption that the rate of entrainment at the edge of the plume is proportional to the vertical velocity at that depth. Although the entrainment constant E is removed in the non-dimensionalisation process through the scalings (2.4), its numerical value is important in making dimensional predictions. The constant itself cannot be obtained theroretically and must be taken from laboratory results (Turner, 1973). For plumes, the best method for measuring E is to measure the first front's progress and compare it to the dimensional form of (2.8). An extensive review of the entrainment assumption is found in Turner (1986).

For vertically-descending axisymmetric plumes, the exact value of E depends on the plume profile used. The relationship between E for top-hat profiles and E_g for the more commonly used Gaussian profile is given by $E_g = 2^{1/2}E$ (Turner, 1973). For the equivalent top-hat profile, Morton et al. (1956) found $E = 0.131$ while Baines and Turner (1969) found $E = 0.141$. Previously, Rouse et al. (1952) had obtained $E = 0.117$ using measurements in air, which is the value Turner (1986) recommended in his review, while Cardoso and Woods (1993) used $E = 0.127$. The differences in E may have resulted from variations in the experimental conditions, but are of little consequence to the theory. In the experiments of chapters 4 and 6, I found best agreement between theory and experimental observations when $E = 0.129 \pm 0.004$.

2.2.3 Time-Varying Buoyancy Sources

Killworth and Turner's (1982) study of plumes from sources displaying time-varying buoyancy fluxes is summarised here because it is related to both the production of deep water sources (chapter 3) and my work on multiple plumes (chapter 6). Their work was motivated by naturally occurring sources of buoyancy where diurnal and seasonal variations existed in timescales much smaller that that required for the stratified environment to be established. The equations used in their model were effectively identical to (2.1) and (2.3). Since the source buoyancy flux varied with time, it was possible that the plume did not reach the bottom during the source's weaker phase

because the stratification established during the maximal phase was too strong. The plume was assumed to spread out at an intermediate depth where it was neutrally buoyant. The system of equations for the time-varying case was solved numerically using a finite-difference method.

In their study, Killworth and Turner (1982) discussed the cases where the buoyancy flux was given by sinusoidal, sawtooth and stochastic functions of time. In each case, they found that the resulting plume and environmental quantities at large times were very similar to the steady-state solution given by Baines and Turner (1969) for a steady source. The maximum value of F in the cycle was the most important parameter in determining the system's properties. A plot of the averaged plume quantities in the sinusoidally varying source case is given in figure 2.4.

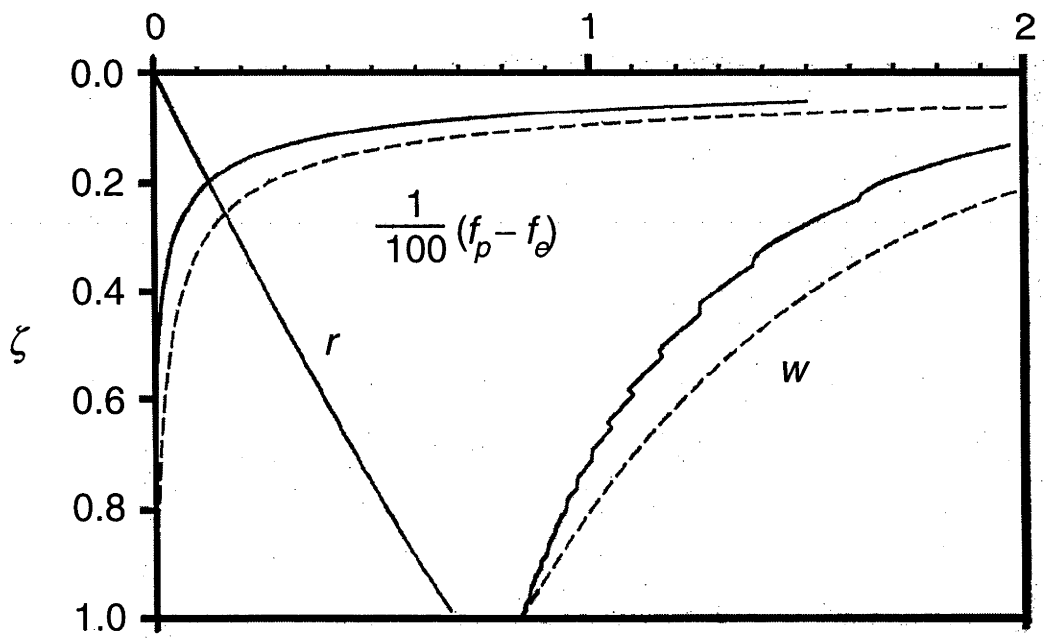

Figure 2.4. The averaged plume radius r, velocity w and buoyancy excess over the environment $f_p - f_e$ in a plume from a source with sinusiodally varying buoyancy flux (————). Also plotted are the equivalent quantities for a steady source (- - - - - - - -). Note that the two plots for r coincide. (Taken from Killworth and Turner, 1982.)

2.3 Internal Gravity Waves

When stably stratified bodies of fluid are disturbed, gravitational forces act on the fluid to generate internal gravity waves. The waves travel through the body and energy can propagate through the stratification. Internal gravity waves are sometimes responsible for phenomena such as the formation of clouds in the atmosphere, and fluctuations of temperature in oceans and lakes. Such waves exist on both the interface of homogenous layers of fluid and in continuously stratified bodies. In this section, I review some of the properties of internal gravity waves in the latter. More complete reviews are given by Acheson (1990), Baines (1995), Lighthill (1978) and Turner (1973).

The fluid is assumed to be inviscid, incompressible and non-diffusive. The equations of motion are

$$\rho\left\{\frac{\partial \boldsymbol{u}}{\partial t}+(\boldsymbol{u}\cdot\nabla)\boldsymbol{u}\right\}=-\nabla p+\rho g$$

$$\nabla\cdot\boldsymbol{u}=0 \qquad (2.13)$$

(Euler's equations) and

$$\frac{\partial \rho}{\partial t}+(\boldsymbol{u}\cdot\nabla)\rho=0.$$

Let the undisturbed (stable) density profile of the fluid be $\rho = \rho_0(y)$ and pressure field $p = p_0(y)$. In the two-dimensional system, small perturbations of the system lead to

$$\boldsymbol{u}=\big(u(x,y,t),w(x,y,t)\big),$$

$$p=p_0(y)+p'(x,y,t)$$

and

$$\rho=\rho_0(y)+\rho'(x,y,t),$$

where u, w, p' and ρ' are small. By applying the Boussinesq approximation and ignoring the quadratic terms in u, w, p' and ρ', (2.13) becomes

$$\rho_0\frac{\partial u}{\partial t}+\frac{\partial p'}{\partial x}=0, \qquad (2.14a)$$

$$\rho_0\frac{\partial w}{\partial t}+\frac{\partial p'}{\partial y}+\rho' g=0, \qquad (2.14b)$$

$$\frac{\partial u}{\partial x}+\frac{\partial w}{\partial y}=0 \tag{2.14c}$$

and

$$\frac{\partial \rho'}{\partial t}+w\frac{\partial \rho_0}{\partial y}=0. \tag{2.14d}$$

The solution to (2.14) consists of modes which are best illustrated in an example given by Prandtl (1952). For $\rho_0 \propto e^{-y/H_0}$ where H_0 is a length scale, $N = (g/H_0)^{1/2}$ is constant. The solution for u and w are then

$$u = A\omega e^{y/2H_0}\cos kx\left(\frac{1}{2H_0 k}\cos my-\frac{m}{k}\sin my\right)e^{i\omega t}$$

and (2.15)

$$w = A\omega e^{y/2H_0}\sin kx\cos my\, e^{i\omega t},$$

where A is the amplitude, k and m the horizontal and vertical wavenumbers and

$$\omega = N\left(\frac{k^2}{k^2+m^2+\frac{1}{4H_0^2}}\right)^{1/2}$$

is the frequency. The solution (2.15) represents a cellular standing wave (figure 2.5) with horizontal and vertical wavelengths $\lambda_h = 2\pi/k$ and $\lambda_v = 2\pi/m$. The pattern can be fitted in a closed rectangular region whose planes coincide with the planes of zero horizontal and vertical motion. There can be an arbitrary number of cells in the horizontal and vertical which gives an infinite number of possible modes. Internal standing waves with a variety of modal structures have been produced in the laboratory by Thorpe

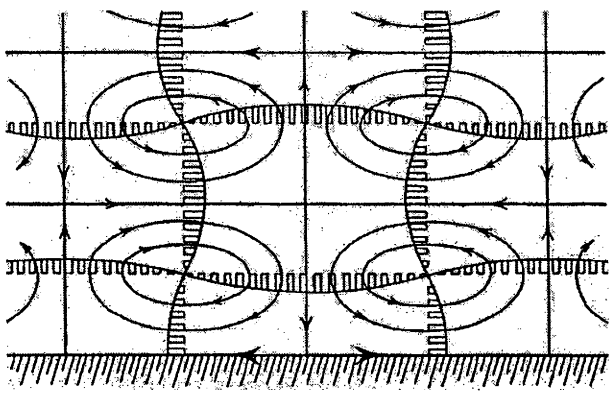

Figure 2.5. Displacements and streamlines in a cellular standing internal gravity wave mode. (From Prandtl, 1952 and taken from Turner, 1973.)

(1968). It will be seen in chapter 4 that a plume outflow at the bottom of a stratified tank excites internal gravity waves that also lead to modal structures.

When the internal gravity waves are propagated from a small localised disturbance, the oscillatory motions are concentrated in bands bounded by "rays" originating at the edges of the source. On elimination of u, p' and ρ', (2.14) reduces to

$$\frac{\partial^2}{\partial t^2}\left\{\frac{\partial^2 w}{\partial x^2}+\frac{\partial^2 w}{\partial y^2}\right\}+N^2(z)\frac{\partial^2 w}{\partial x^2}=0. \tag{2.16}$$

Assuming that w has a wave solution of the form $w=\hat{w}(y)e^{i(kx-\omega t)}$, (2.16) becomes

$$\frac{d^2\hat{w}}{dy^2}+\left(\frac{N^2}{\omega^2}-1\right)k^2\hat{w}=0. \tag{2.17}$$

Wave-like solutions to (2.17) occur only if $\omega < N$ and thus N is the upper limit of frequency for which wave motions can exist in a stratified fluid. (If $\omega > N$ the disturbances decay.) If N is constant and $\hat{w} \propto e^{imy}$ (periodic in y), then the dispersion relation is

$$\begin{aligned}\omega &= N\left(\frac{k^2}{k^2+m^2}\right)^{1/2}\\ &= N\cos\theta,\end{aligned} \tag{2.18}$$

where θ is the angle ($|\theta| \le \pi/2$) between the horizontal and the wavenumber vector $\boldsymbol{k} = (k, m)$. The lines of constant phase are $kx + my$ = constant and with ω defined by (2.18), the phase velocity $\boldsymbol{c}$ is given by

$$\begin{aligned}\boldsymbol{c} &= \left(\frac{Nk^2}{\left(k^2+m^2\right)^{3/2}},\frac{Nkm}{\left(k^2+m^2\right)^{3/2}}\right)\\ &= \left(\frac{N}{|\boldsymbol{k}|}\cos^2\theta,\frac{N}{|\boldsymbol{k}|}\sin\theta\cos\theta\right).\end{aligned} \tag{2.19}$$

Therefore, the lines of constant phase move in a direction perpendicular to themselves. The group velocity $\boldsymbol{c}_g = (\partial\omega/\partial k, \partial\omega/\partial m)$, however, is parallel to the lines:

$$\begin{aligned}\boldsymbol{c}_g &= \left(\frac{Nm^2}{\left(k^2+m^2\right)^{3/2}},-\frac{Nkm}{\left(k^2+m^2\right)^{3/2}}\right)\\ &= \left(\frac{N}{|\boldsymbol{k}|}\sin^2\theta,-\frac{N}{|\boldsymbol{k}|}\sin\theta\cos\theta\right).\end{aligned} \tag{2.20}$$

Thus the phase and group velocities are perpendicular to one another (figure 2.6). For a source generating a disturbance of frequency ω ($\leq N$), the crests and other lines of constant phase stretch radially out from the source at an angle $\theta = \cos^{-1}(\omega/N)$ to the vertical (figure 2.7, where the lines of constant phase are indicated by the light and dark bands). The energy created by the disturbance is propagated at c_g. As the phase and group velocities have horizontal components in the same direction and vertical components in opposite directions, the energy propagation in internal waves has an upward component when the motion of crests has a downward component and vice versa. In figure 2.7, for example, the motion of lines of constant phase perpendicular to themselves is downwards in the upper half of the photograph where the energy is propagating upwards. Only one or two wavelengths are seen because when the crests have travelled a short distance, they leave the region defined by the rays where all the energy is confined.

For slowly varying N, (2.18), (2.19) and (2.20) can be applied locally. The wavefronts bend and change direction according to the stratification. As $\omega \rightarrow N$ ($\theta \rightarrow 0$), the wavefronts bend to approach the vertical and as $\omega \rightarrow 0$ ($\theta \rightarrow \pi/2$), they become horizontal. Rays can also reflect off solid boundaries, but they always retain their angle to the vertical.

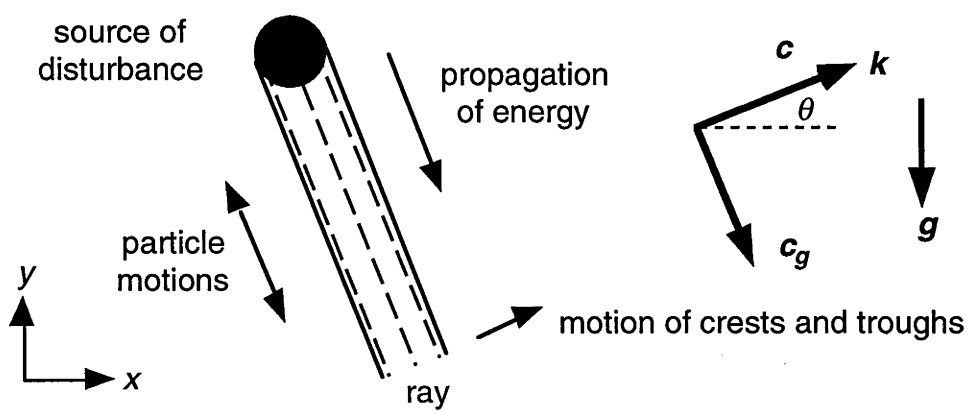

Figure 2.6. For internal waves propagating through a continuously stratified fluid, the wavevector $\boldsymbol{k}$ and phase velocity $\boldsymbol{c}$ are perpendicular to the group velocity $\boldsymbol{c}_g$.

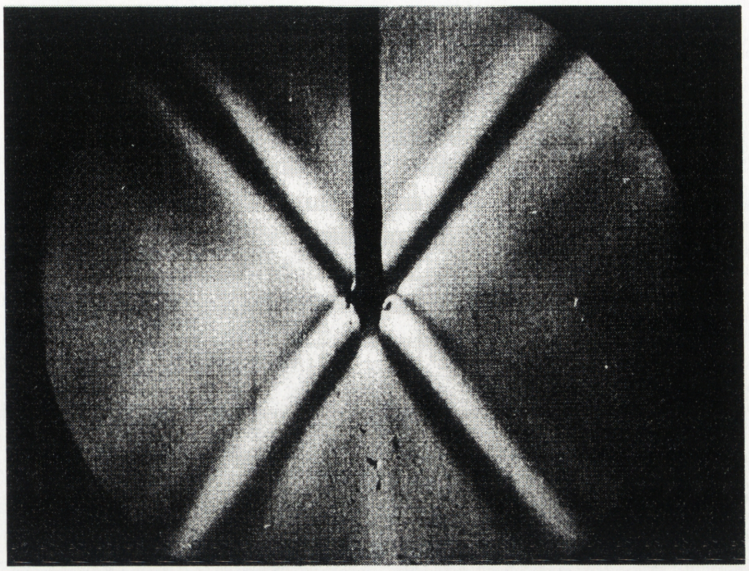

Figure 2.7. The waves generated in an uniformly stratified fluid by the oscillation of a horizontal cylinder at frequency $0.7N$. The oscillatory motions are concentrated in bands bounded by "rays" originating at the edges of the source. (Photograph by Mowbray and Rarity, 1967 and taken from Lighthill, 1978.)

Chapter 3

Ocean Stratification and Circulation

3.1 The Deep Ocean

The structure of the oceans consists of a warm, less dense layer at the surface which progressively changes to a cold, dense interior. As well as temperature gradients, salinity differences also contribute to the average vertical density gradient, but to a lesser extent. Because the ocean exhanges heat and fresh water with the atmosphere at the surface, the surface properties vary according to geographic location and season. Considerable surface currents, generated by frictional stresses with the faster moving atmosphere, carry water masses large distances. In contrast, the bulk of the ocean interior, being insulated from the atmosphere, displays only small spatial variations in its properties and moves at a much slower rate. Between the surface and the interior is the thermocline where water properties, especially temperature, change rapidly with depth.

The density structure of the world's oceans is given in figure 3.1 where the zonal mean cross-section of density with depth is shown. The density is given as σ_θ which represents the density anomaly of sea-water (compared with fresh water) that is brought adiabatically to the surface. The density increases rapidly from the surface through the thermocline but shows only a small increase in the interior below 200 m.

The oceans maintain their stratification through the thermohaline circulation which continually overturns surface and interior waters. The sinking of surface waters to absyall depths is known to occur at several localised regions while the rising is distributed over most areas (Robinson and Stommel, 1959). Water properties indicate that there are only two major sources of deep water over 2000 m - North Atlantic Deep Water (NADW) and Antarctic Bottom Water (AABW). Figure 3.2 shows the temperature and salinity

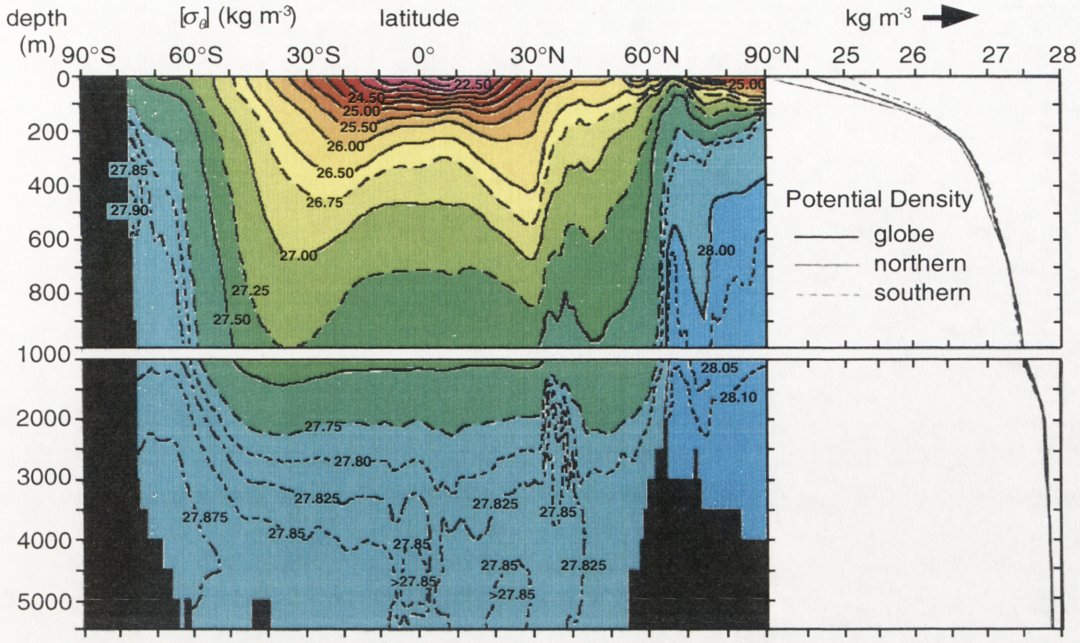

Figure 3.1. The annualised zonal mean cross-section of density (σ_θ) for the top ocean layer 0 – 1000 m and for the layer below 1000 m (after Levitus, 1982). Vertical profiles of the hemispheric and global mean density are shown on the right. (Taken from Peixoto and Oort, 1992, page 192.)

profiles in the Atlantic Ocean along 25°W. The bulk of water in the Atlantic between 2000 m and 4000 m has temperature 2 – 4°C and salinity 34.9 – 35.0 practical salinity units (1 psu equates to one gram of salt per kilogram of sea-water). As it extends southward from the North Atlantic, it is recognised as NADW. In the southern hemisphere, the water below 4000 m is colder and fresher (< 2°C and with salinity < 34.8 psu) and as it originates from the Antarctic it is denoted AABW. A qualitative model of the deep circulation was developed by Stommel (1958) and shown in figure 3.3. It shows the two sources of deep water feeding intense western boundary currents in the Atlantic which spread into the interior through large cyclonic gyres in each hemisphere. The southern gyre also feeds into the Indian Ocean, which in turn feeds into the Pacific Ocean. Upwelling brings water to the shallower depths and inflow into the sources completes the circulation.

Various studies have verified aspects of Stommel's model. A single deep water source in the polar region has been shown in a numerical model to establish a relatively

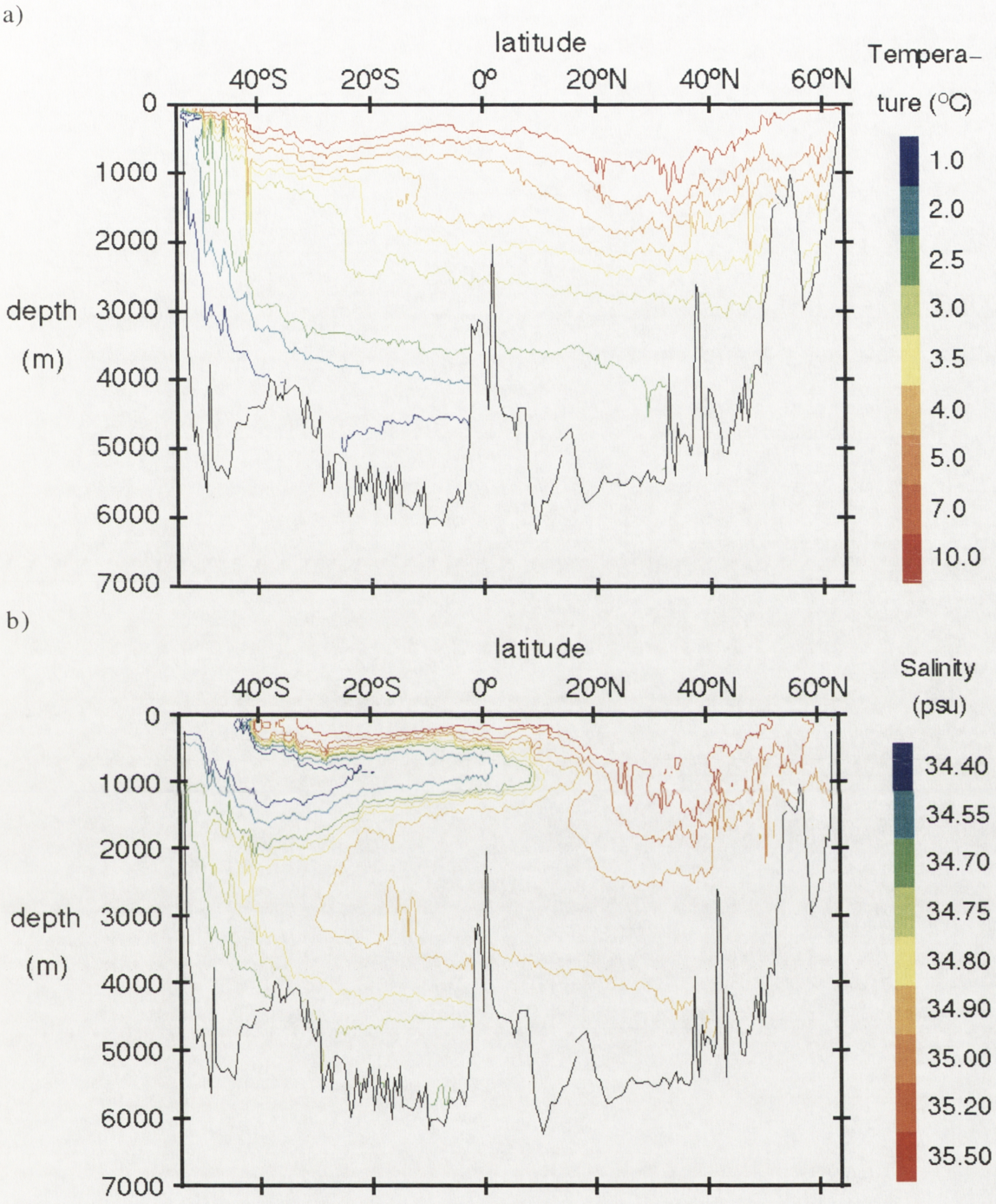

Figure 3.2. The properties of the Atlantic Ocean along 25°W from the sub-polar Antartic to Iceland: (a) temperature and (b) salinity. Note that a mid-ocean ridge intersects this cross-section near the equator so that in the southern hemisphere, the cross-section is west of the ridge while in the northern hemisphere, the cross-section is east of the ridge. (Source: Data from software package "Ocean Atlas" by J. Osborne, NOAA/APEL. The data was taken during July-August, 1988 (*Oceanus*) and February-April, 1989 (*Melville*).)

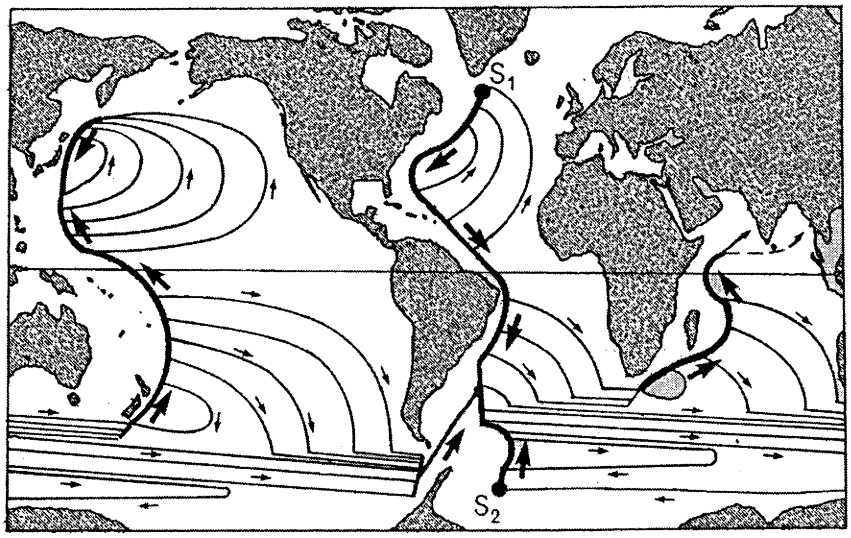

Figure 3.3. Stommel's simplified model (1958) of the deep circulation of the world's oceans. The sources of deep water are S_1 in the North Atlantic and S_2 in the Weddell Sea.

intense boundary current that feeds a cyclonic gyre (Kawase, 1987). It was also shown that the deep western boundary current originating from the source crosses the equator to feed both basins only if the damping associated with upwelling is weak. This is qualitatively consistent with the circulation in the North Atlantic induced by the source in the Norwegian-Greenland Seas. The predominant features of the boundary current and cyclonic gyre were still present when simple bottom topography (in the form of a plateau and a depression) was imposed on the ocean basin (Kawase and Straub, 1991).

3.2 Deep Water Formation and Outflows

Most of the deep and bottom waters of the oceans (depths > 2000 m) and intermediate waters (depths 500 – 2000 m) originate from outflows of marginal seas or continental shelf regions where intense and sustained exchange of heat or fresh water between the surface and the atmosphere causes the density of waters to increase (Warren, 1981). Marginal seas are characterised by being semi-enclosed with a restricted exchange with the open ocean so that they tend to trap dense water. In the present climate, there are four major outflows from marginal seas (Price and O'Neil-Baringer, 1994). Outflows

from the Arctic Ocean passing through the Denmark Strait and from the Norwegian-Greenland Sea through the Faroe Bank Channel contribute to NADW. The Filchner Ice Shelf Overflow feeds into the Weddell Sea and, after being joined by other Antarctic outflows, contributes to AABW. The Mediterranean Sea also produces dense water, which, after mixing with surrounding lighter water, settles in the North Atlantic at depths of only 800 – 1300 m. Other deep and intermediate waters are believed to be formed by convection in open oceans and in adjoining unenclosed seas – for instance, throughout the mid-latitudes of the southern hemisphere and in the Labrador Sea.

Various types of exchanges with the atmosphere cause dense water to be formed. In polar regions such as the Labrador, Norwegian-Greenland and Weddell Seas, ice formation during winter leaves behind cold and highly saline water. In the Mediterranean Sea, net evaporation increases the salinity and hence density of water. In many situations, newly formed dense water sinks to the bottom along slopes and continental shelves. Strong convection from the surface can also bring dense water directly to the bottom in the form of "chimneys" (Killworth, 1979 and 1983). For example, intense surface cooling has been known to cause vertical mixing in regions 10 – 50 km wide and up to 2000 m deep in the north-west Mediterranean and in the Weddell Seas.

In the case of dense water outflows, the exhange between the marginal sea and the open ocean is determined by factors such as hydraulic control, topographic features (for example, the width and depth of the constriction) and even basin scale circulation. In each case, the waters must descend continental shelves and slopes before reaching their final depth (Whitehead, 1989). As the outflows descend to the open ocean, entrainment of surrounding waters alters the properties of the outflow so that the product waters that reach and spread in the open ocean may have very different properties to that of the original source water. A model for the modification of outflow properties has been developed by Price and O'Neil-Baringer (1994). The densities of the source and product waters for the four mentioned outflows are given in table 3.1 (σ_θ and σ_4 are the densities of the water brought adiabatically to the surface and to depth 4000 m respectively). The Mediterranean Outflow is the densest at the source while that of the Filchner Ice Shelf

	Source Water Density	Product Water Density	
	(σ_θ kg m^{-3})	(σ_θ kg m^{-3})	(σ_4 kg m^{-3})
Filchner Ice Shelf Outflow	27.93	27.89	46.20
Denmark Strait Outflow	28.04	27.92	46.07
Faroe Bank Channel Outflow	28.07	27.90	45.88
Mediterranean Sea Outflow	28.95	27.70	44.91

Table 3.1. The four major outflows of dense water into the world's oceans. The source water density σ_θ is the density at the edge of the marginal sea where the water was formed while the product water densities σ_θ and σ_4 are taken from where the outflows are spreading in the ocean. (Source: Price and O'Neil-Baringer, 1994).

Outflow is the least dense. However the product waters of the Mediterranean Outflow is the least dense and hence it spreads at depths of only 800 – 1300 m to form a warm and highly saline intrusion into the North Atlantic (see figure 3.2). The outflows from the Denmark Strait and the Faroe Bank Channels are slightly denser than the Filchner Ice Shelf Outflow when all are brought adiabatically to the surface, but at the depths where these outflows eventually settle in the Atlantic Ocean, Filchner Ice Shelf Water is the densest. Thus NADW is found above AABW in most of the world's oceans.

3.3 Other Influences on Thermohaline Circulation

Besides the buoyancy-driven effects of deep water formation, the circulation of the oceans is also influenced by factors such as rotation, topography and double-diffusive convection. Rotation plays an important role through the Coriolis force, which acts to deflect all large-scale motions in the oceans. The Coriolis force results in large ocean gyres, fronts (regions of anomalously large horizontal gradients in temperature, salinity or density) and its variation with latitude leads to narrow boundary currents. The intense western boundary currents and cyclonic gyres in Stommel's model (figure 3.3) are features of the earth's rotation.

Coriolis forces also affect outflows from regions of deep convection, controlling at least patterns of horizontal flow and possibly having some influence on the overall

density stratification in the ocean interior. Laboratory experiments have shown that the manner in which turbulent plumes spread in a tank is changed when the tank is subjected to rotation (Pierce and Rhines, 1996). Water from deep convection often escapes from the sinking region through the frictional effects of gyres and eddies and also through boundary currents (Send et al., 1996). For instance, the Mediterranean Outflow turns northwards after leaving the Strait of Gibraltar, where the Coriolis force is balanced against the continental slope (Price et al., 1993).

Apart from side boundaries such as continental slopes, topographic barriers impede the flow of water between ocean basins. For instance, the Atlantic mid-ocean ridge separates the Atlantic Ocean into eastern and western basins below approximately 4000 m. Properties associated with AABW, which feeds into the bottom of the western basin, are not found in the eastern basin because AABW is prevented from spreading directly into the eastern basin by the ridge (see figure 3.2 where the colder and fresher AABW of temperature $< 2°C$ and salinity < 34.8 psu is found only in the western basin south of the equator on 25°W). In contrast, properties associated with NADW are found in both basins because NADW spreads at depths close to the ridge and can therefore spill into both basins.

The major properties of sea water which contribute to density differences are salt (sodium chloride) and heat. Diffusion of these two components occurs at different rates, leading to instabilities when waters of different temperature and salinity are placed next to one another. In order for vertical instabilities to develop in the oceans, the vertical salt gradient necessary is only 1/100 that of temperature (when both are compared in density units) and this is satisfied over many regions (Schmitt, 1994). Such instabilities lead to "salt-fingering", the rising and falling of water in thin columns, and "thermohaline layering", where well mixed layers of water are separated by sharp interfaces. Salt fingers and layering have been observed, for example, at the bottom of the Mediterranean Outflow (Magnell, 1976) and layering has been recorded in the Arctic Ocean (Neal et al., 1969).

3.4 Motivation for the Current Research

The research to be presented in the following chapters is aimed at achieving a better understanding of the processes involved in the large-scale ocean circulation. As oceanic deep water sources are buoyancy driven and their outflows mix with surrounding water, they are in many ways similar to buoyancy sources and plumes in filling-boxes. Indeed, the oceanic density profile (figure 3.1) shows strong gradients near the surface that weaken to smaller gradients in the interior, and there is at least a qualitative resemblence between the oceanic density profile and the stratification produced by a turbulent plume in a filling-box (Killworth and Turner, 1982; see also plot of f_e^*, figure 2.2b). As outlined in chapter 1, this thesis presents, in the following chapters, extensions to the previous work on plumes in filling-boxes. While the extensions do not produce a new model of ocean convection (indeed, some important aspects such as rotation and double-diffusion in plume-driven convection are not considered at all), it is hoped that the more thorough understanding of plumes in filling-boxes will further advance knowledge of the ways in which buoyancy-driven convection affects the oceans.

Chapter 4

Plume-Driven Shear Layers

4.1. Introduction

Most studies of turbulent buoyant plumes have focused on the plume flow itself, with relatively little attention paid to associated motions in the plume surroundings. The "filling-box" process described in chapter 2 has generally been studied in boxes having lengths and widths comparable to the water depth and the theoretical analysis has assumed motions outside the plume to be small. In this chapter, I report experiments which show that in long tanks, a series of strong counterflowing shear layers is established in the stratification produced by the "filling-box" mechanism. I present evidence that the layers are produced by internal gravity wave normal modes excited by the plume outflow. They are similar in structure to columnar modes generated by intrusions into density gradients (Manins, 1976) or by the slow horizontal motion of obstacles in density gradients (Bretherton, 1967).

In the "filling-box" model described by equations (2.1) and (2.3), the outflow layer at the bottom has been found to occupy one-quarter the water depth from the source (Manins, 1979). The motions outside the plume and bottom outflow layer are assumed to be dominated by vertical advection and by horizontal entrainment into the plume. The large-time dependence on depth of the vertical advection velocity V can be calculated from theoretical predictions of the dimensionless plume volume flux r^2w (2.11a), which is converted to V using (2.6a) and (2.4). The model assumes that the entrainment volume per unit depth into the plume is $2\pi REW$ at all depths. For an axisymmetric plume far from all side-walls this provides the horizontal velocity that is attributed to entrainment and directed radially into the plume. In the experiments reported below the plume is also

placed near one end of a long channel in order to constrain the flow in the environment far from the plume to be two-dimensional. (Experiments indicate that the flow in the environment is approximately two-dimensional at a distance of about two plume radii from the axis of the plume.) The entrained water is assumed to be sourced evenly from across the horizontal cross-section of the tank so that the horizontal volume transport increases linearly from zero at the end of the tank opposite the plume to $2\pi REW$ at the plume edge. Thus if B is the width, L the length of the tank and x the distance from the plume end, then the horizontal velocity U attributed to entrainment is

$$U = -2\pi ERW\frac{(L-x)}{BL}. \tag{4.1}$$

(The negative sign indicates that entrainment velocities are directed towards the plume.) The scaling between U and its dimensionless equivalent $u = -rw$ can be calculated from (2.4) as

$$U = 2^{4/3}\pi^{2/3}E^{4/3}F^{1/3}H^{2/3}B^{-1}L^{-1}(L-x)u. \tag{4.2}$$

The dimensionless inflow velocity u is plotted in figure 4.1. Although the entrainment driven velocities increase with depth, they should still be weaker than the velocities in the outflow layer moving away from the plume. This is because the outflow layer only occupies about one-quarter the total depth, yet its volume flux must balance the total entrainment volume flux of the upper three-quarters of the tank.

Thus in the "filling-box" model, the horizontal velocities in the environment are expected to form a fast outflow layer at the bottom directed away from the plume and a slower moving layer above in the opposite direction. In §4.2 and §4.3, I describe experiments that show the circulation pattern consists of many more layers. In §4.4, these layers are compared with theoretical solutions for normal modes of internal gravity waves. Brief comparisons with other systems that show related flow structures and conclusions are given in §4.5.

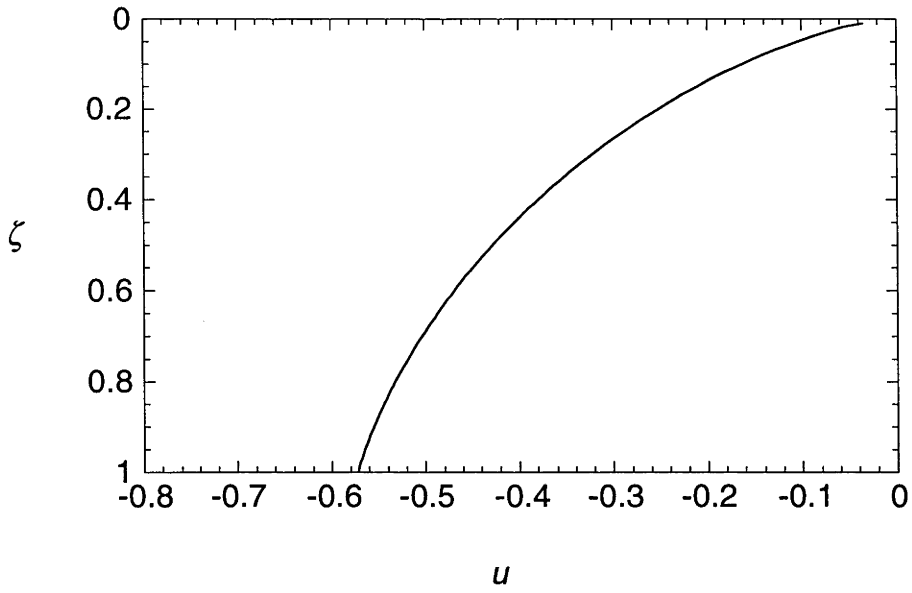

Figure 4.1. The far-field horizontal velocity u induced by entrainment into a plume (4.2) under the assumption of a dynamically passive environment in the "filling-box" model. Negative values of u indicate velocity towards the plume.

4.2. Experiments

In the experiments a dense salt solution was released at a steady rate through a small nozzle just below the free surface of a tank of water. The nozzle, about 6 mm in diameter, was wide enough to ensure that the velocity and momentum of the released water was small so that the source approximated a pure buoyancy source. The nozzle was positioned near one end of the tank and equidistant from three side walls. A peristaltic pump maintained a constant flux of salt water through the nozzle. A typical flow rate used in the experiments was 0.385 $cm^3\ s^{-1}$ with salt solution densities ranging from 1090 to 1180 kg m^{-3}. Two tanks were used. The first was 1.1 m long, 0.3 m wide and 0.24 m deep while the second was 2.0 m long, 0.2 m wide and 0.4 m deep. The nozzles were positioned at various depths to give effective depths of 0.16 m and 0.235 m in both tanks and additionally, 0.3 m and 0.38 m in the larger tank.

Horizontal velocities far from the plume were measured by dropping crystals of potassium permanganate into the tank. As they descended to the bottom, the crystals dissolved to produce a vertical dye line. Horizontal velocities were calculated by

measuring the distortion of this dye line in a short period of time. The short time interval was crucial to ensure the dye did not reach the end walls and also to minimise errors due to the simultaneous upwelling of the water. The movement of the dye line was recorded on video. A grid of lines with 1 cm spacing on the front of the tank allowed measurements of dye displacement correct to 0.5 cm from the video recording.

Conductivity profiles and time records at a fixed point were measured by a four-head conductivity probe (MSCI 5201 manufactured by Precision Measurement Engineering, USA). Simultaneous thermistor measurements (GB38P12 manufactured by Fenwal Electronics, USA) provided a temperature correction for the conversion of conductivity to density using the equations of Ruddick & Shirtcliffe (1979). Fractional density changes of less than 10^{-7} could be detected.

In addition to experiments starting with a homogenous tank that revealed the velocity structure at large times, twelve experiments were conducted to study the evolution of the flow starting from a plume-stratified tank at rest. In these experiments, the plume was run for up to four hours. Within the first hour the first front approached the level of the source and the density profile approached the asymptotic shape. (Because vertical advection velocities decay with height, the first front did not actually reach the level of the source until a much later time.) Conductivity profiles as well as measurements at a fixed point were taken both before and after the asymptotic state had been reached. The plume was later turned off and the motions in the stratified tank allowed to come to rest. The plume was then restarted and the subsequent redevelopment of the horizontal velocity profile monitored. The parameters of each experiment are given in table 4.1 along with three timescales: $\overline{N}^{-1}$ (where $\overline{N}$ is the depth-averaged buoyancy frequency at large times), $t_w = L/\overline{N}H$, the timescale for long waves to travel the length of the tank, and $t_a = 33.7A/H^{2/3}F^{1/3}$, the time for vertical advection of water in the "filling-box" environment. The advection time is derived from the non-dimensionalisation for t given in (2.4) and is the time predicted by the theory for the first front to reach $\zeta = 0.1$.

	Experimental parameters		Timescales			Results	
Number	Tank dimensions	Buoyancy flux	$\overline{N}^{-1}$	$L/\overline{N}H$	$33.7A/H^{2/3}F^{1/3}$	Time for layers to develop	Oscillation period of layers
	$L \times W \times H$ (m)	(10^{-7} m^4 s^{-3})	(s)	t_w (s)	t_a (s)	t_e (s)	t_o (s)
4.1	2.0 × 0.2 × 0.16	6.81	1.96	24.5	5200	300 ± 60	1620 ± 120
4.2	2.0 × 0.2 × 0.235	6.81	3.28	27.9	4030	360 ± 60	2040 ± 120
4.3	2.0 × 0.2 × 0.30	6.81	4.55	30.2	3420	420 ± 60	2280 ± 60
4.4	2.0 × 0.2 × 0.38	6.81	6.22	32.8	2910	480 ± 60	2640 ± 60
4.5	2.0 × 0.2 × 0.16	3.34	2.49	31.1	6600	360 ± 60	2220 ± 60
4.6	2.0 × 0.2 × 0.235	3.34	4.17	35.3	5100	480 ± 60	2010 ± 90
4.7	2.0 × 0.2 × 0.30	3.34	5.77	38.3	4330	450 ± 60	2280 ± 60
4.8	2.0 × 0.2 × 0.38	3.34	7.88	41.5	3700	600 ± 60	2280 ± 60
4.9	1.1 × 0.3 × 0.16	6.81	1.96	13.5	4290	150 ± 30	2400 ± 300
4.10	1.1 × 0.3 × 0.235	6.81	3.28	15.4	3320	180 ± 30	2430 ± 270
4.11	1.1 × 0.3 × 0.16	3.34	2.49	17.1	5440	180 ± 30	2190 ± 210
4.12	1.1 × 0.3 × 0.235	3.34	4.17	19.4	4210	210 ± 30	2130 ± 60

Table 4.1. Parameters and results for the experiments.

4.3. Results

4.3.1 The Layers

The most striking observation was that the stratified environment produced by a turbulent plume supported a strong and persistent series of layers. These layers appeared as dominant features in the profiles of horizontal velocity, as seen in figure 4.2a, but corresponded to extremely small perturbations in the density gradient. Hence I call these shear layers in order to distinguish them from density layering. Figure 4.3 shows characteristic horizontal velocity profiles in the middle of the tank in three experiments. At the bottom of the tank the outflow layer thickness was approximately one-quarter of the tank depth. Immediately above the outflow layer there was a layer of similar thickness moving towards the plume. In the upper half of the tank there were several layers. Both the vertical scales and the magnitudes of the horizontal velocities in the shear layers generally decreased with height. At the centre of the third and fifth layers from the bottom, as defined by local velocity extrema, the water was almost stationary. Between these two layers there was a region of moderate flow towards the plume. At the third

(a)

(b)

Figure 4.2. (a) A photograph of a typical experiment (in a 1.1 m tank). Potassium permanganate crystals dropped into the tank left an initially vertical line of dissolved dye in the water. As this dye line moved passively in the water, it revealed the shear layers generated by the plume outflow. The tracer was also used to measure the horizontal displacement for determining the velocity profile. (b) A streak photograph of a typical experiment.

velocity extremum (ζ = 0.3 to 0.4), the velocity oscillated slowly from positive to negative, so that the flow was at times away from the plume. A streak photograph (figure 4.2b) not only shows the shear layers but also indicates that the horizontal velocities heading towards the plume decrease with increasing horizontal distance from the plume.

Another view of this previously unexpected velocity structure is obtained by subtracting the predicted horizontal inflow velocity due to entrainment from the measured velocity (figure 4.3b). Layers can be defined as the water lying between zeroes of the horizontal velocity difference $u - u_e$.

At the end of the tank away from the plume, I also observed a concentrated upwards flow from the bottom outflow layer that fed the return flow towards the plume in the second layer. This existed because the uniform vertical advection distributed over the area of the box at the top of the outflow layer was insufficient to accommodate the total volume flux supplied to the layer by the turbulent plume. The same process continued to operate to some extent above the second shear layer with a tendency for the horizontal volume flux in each layer to partly reflect from the end walls and return in the next layer.

It should be emphasised that water elements did not necessarily traverse the tank from end to end during their residence time in each layer. The distributed vertical advection of water "short-circuited" the paths. For example there was little horizontal flow (relative to the tank) in the third layer, yet if a thin layer of water was dyed, this dyed water was seen to migrate upwards through this layer. Thus those water particles which were not entrained into the plume migrated upwards through the series of shear layers, experiencing an oscillatory horizontal velocity.

4.3.2 Long Period Oscillations

At large times after the stratification had developed the system did not reach a steady state but instead continued to support slow oscillations. As the first front approached $\zeta = 0.1$, the number of shear layers oscillated between four and five. Later when the first front had reached $\zeta = 0.05$, the number of layers oscillated between five and six. In a rare instance, seven layers were observed. However, the maximum number

a)

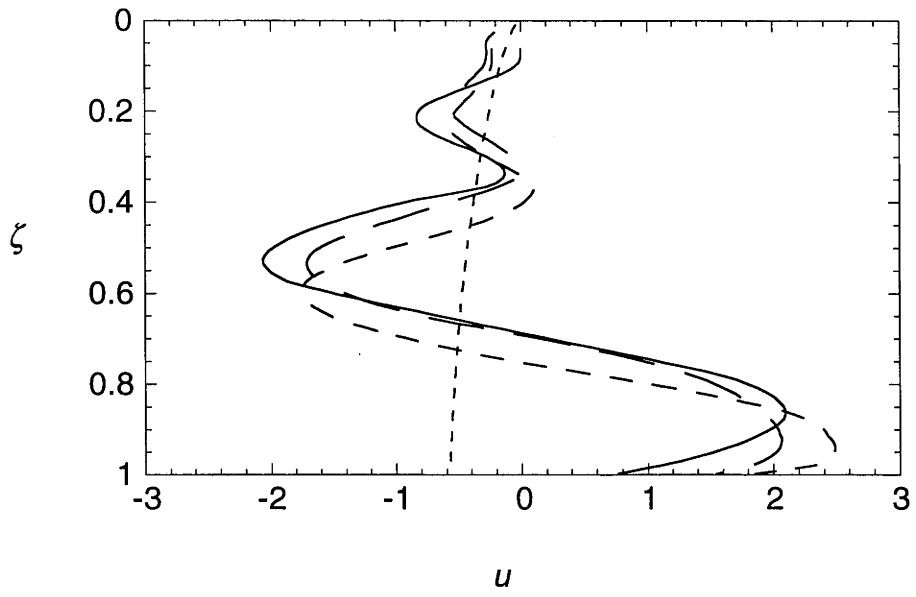

b)

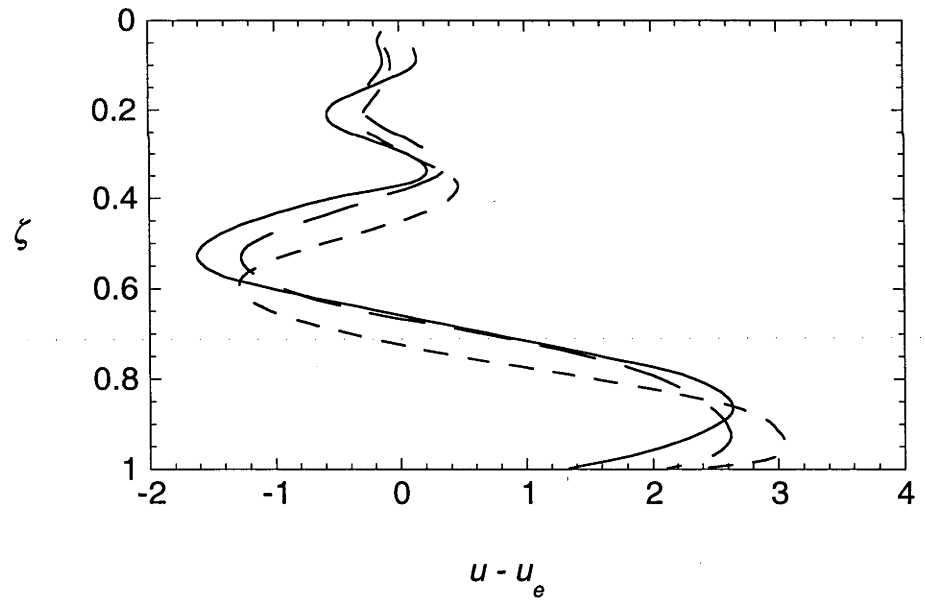

Figure 4.3. Sample horizontal velocity profiles measured in the middle of the tank in three experiments listed in table 4.1: ———— experiment 4.10; —— —— experiment 4.4; — — — — experiment 4.2. (a) The measured velocities u and predicted two-dimensional entrainment velocity u_e (- - - - - - - -) relative to the tank and (b) the difference $u - u_e$. Negative velocities are towards the plume.

of layers typically observed was six. The horizontal velocity profiles obtained during a fluctuation from five to four layers and back are shown in figure 4.4.

Velocity fluctuations (corresponding to the changing number of layers), were most visible in the region $0.15 < \zeta < 0.45$. At these depths the positions of the extrema in horizontal velocity shifted, resulting in large velocity fluctuations at a given depth. Indeed, in some cases, the velocity at a given depth fluctuated between two values that were close to local velocity maxima of opposite signs.

As expected in buoyancy-driven flows, fluctuations in horizontal velocity were accompanied by oscillations in the density field. In the absence of internal waves and shear layers, the "filling-box" solution predicts that the density increases linearly with time at a fixed point. However, conductivity measurements at a fixed point showed that the density oscillated about this linear trend. An example is shown in figure 4.5, where I plot the density at $\zeta = 0.25$ as a function of time (figure 4.5a) and the deviations from the best fit linear trend (figure 4.5b) for experiment 4.10. The period of oscillation t_o (listed in table 4.1) was measured from the density records for the asymptotic state for each experiment. The periods were all of the order of $(0.3 - 0.9)t_a$ and $(50 - 200)t_w$.

4.3.3 Shear Layer Establishment in Existing Stratification

After the tank had been stratified the plume was turned off and the motions allowed to decay. The plume was later restarted and horizontal velocity profiles were taken at regular intervals. In twelve experiments, the pattern of development of the layers was the same. A sequence of profiles from one run is shown in figure 4.6. At small times (figure 4.6a), the stratified water above the outflow layer began to move away from the plume and a broad region in the upper half of the box moved towards the plume. Ignoring the effects of stresses imposed by the rigid (no-slip) bottom and the partly rigid (free-slipping) surface at the top, this motion resembled the second baroclinic mode (found in §4.4 for the "filling-box" density profile). The position of the inflow velocity maximum shifted down with time and a third shear layer soon formed at the top (figure 4.6b). It will be seen below that the motion at this stage appeared to be dominated by the

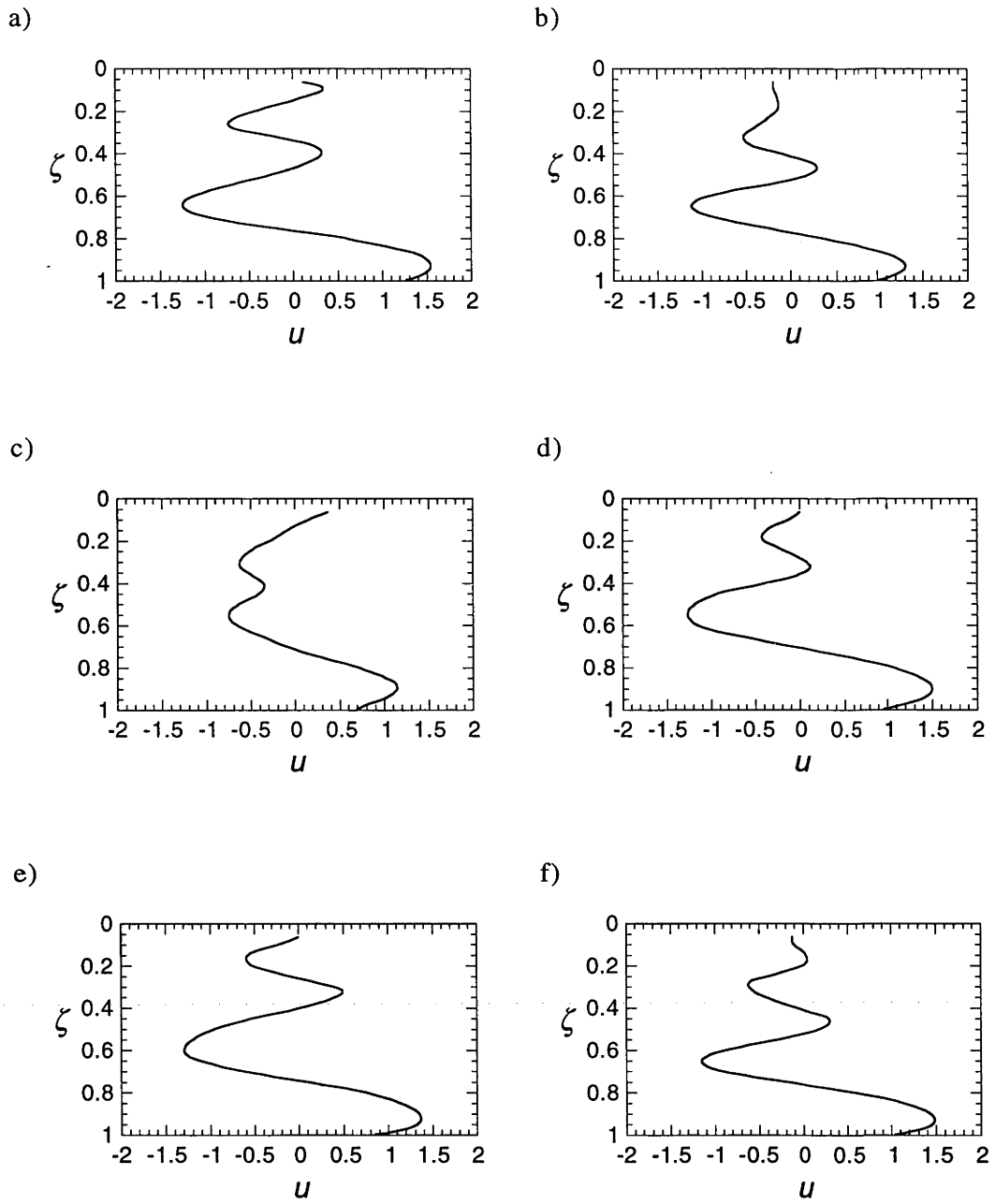

Figure 4.4. Horizontal velocities at eight minute intervals during experiment 4.10 (table 4.1) showing the transition between a five-layered system and a four-layered system and back. (a) 62 min, (b) 70 min, (c) 78 min, (d) 86 min, (e) 94 min and (f) 102 min after start.

a)

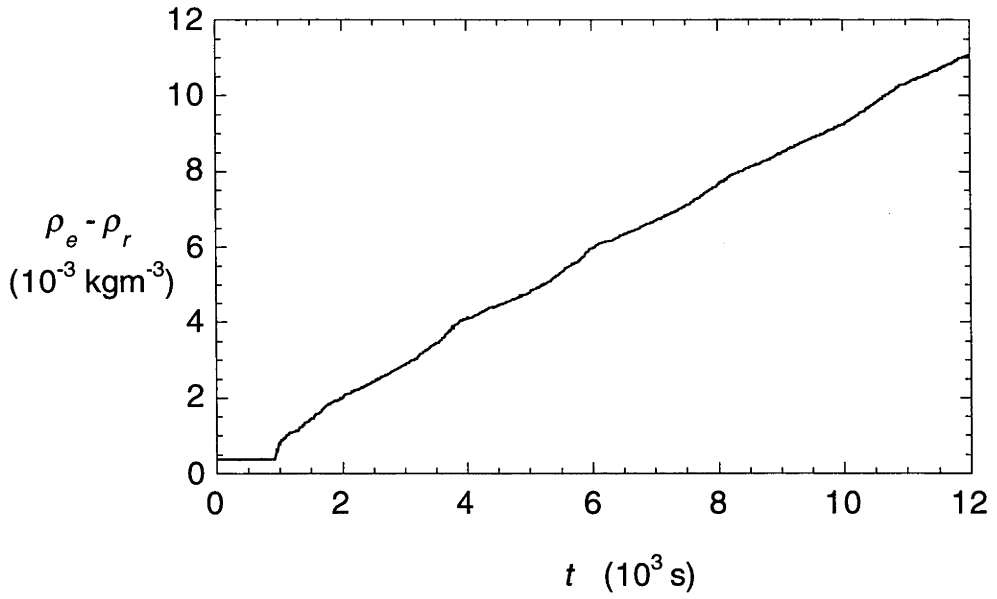

b)

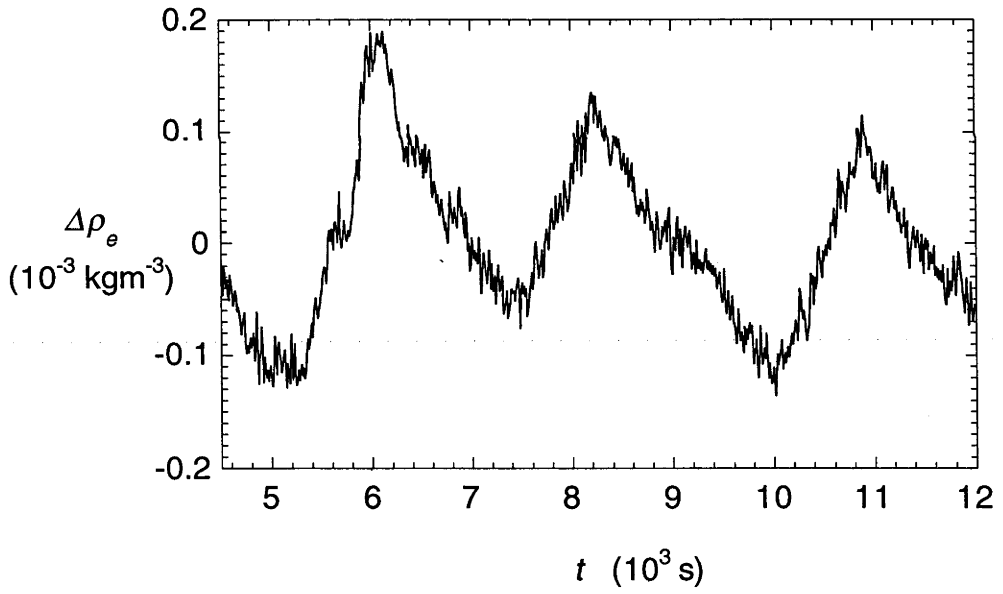

Figure 4.5. The density $\rho_e - \rho_r$ determined from the conductivity probe fixed at 0.175 m from the bottom (ζ = 0.25) in experiment 4.10. The first front passed the probe at $t \approx 900$ s. (a) The density variation is approximately linear with time long after the first front has passed the probe. (b) Deviations $\Delta\rho_e$ from the linear trend in (a) show low frequency periodic oscillations.

third baroclinic mode. Additional vertical structure continued to develop in the velocity profile, consistent with the appearance of higher baroclinic modes being excited by the bottom outflow, until the velocity profile reached that in figure 4.6f. The time required for the development of the baroclinic structure was much shorter than the period of the persistent low-frequency oscillations. Hence the structure in figure 4.6f was a quasi-steady state. The dominant vertical length scale of the velocity profile appeared to be set by the depth of the plume outflow.

I estimated timescales for the establishment of the shear layers by measuring the time t_e taken for the third velocity extremum (from the bottom) to migrate down to the level $\zeta = 0.28$ and for the fourth extremum to reach $\zeta = 0.12$ (the state in figure 4.6e). A plot of t_e against t_w, each normalised by $\overline{N}^{-1}$, (figure 4.7a) shows that the time for the development of the shear layers was proportional to the travel time of internal waves. (Note that both the travel times of internal waves along the length and up through the height of the box are proportional to $L/\overline{N}H$.) The data are well described by a straight line passing through the origin, $t_e = (12.6 \pm 0.8)\ L/\overline{N}H$. Most of the variance in this result, however, can be attributed to the effects of the third independent timescale, t_a. A plot of t_e against t_a, each normalised by t_w, (figure 4.7b) shows that $t_e/t_w = (15.8 \pm 0.5) - (0.0172 \pm 0.003)\ t_a/t_w$. Thus the normalised establishment time was weakly dependent on the advection time, becoming longer for more rapid "filling-box" ventilation. Establishment timescales that are 12 to 15 times the $L/\overline{N}H$ scale are consistent with the dominance of higher baroclinic modes which have smaller phase speeds. For instance, if the total water depth is replaced by $H/4$, the dominant vertical scale of forcing, then t_e indicates that these higher modes traverse the length of the tank only a few times before the quasi-steady flow is established.

In order to place the rate of vertical advection in perspective, it should be noted that the establishment of the quasi-steady shear layers required a time of the order of one-tenth the advection timescale, which is also the time required for the tank to be refreshed with new plume water. This is illustrated in figure 4.8, which shows the distribution of water from the plume at a time approximately t_e after the restart. The dyed water of the

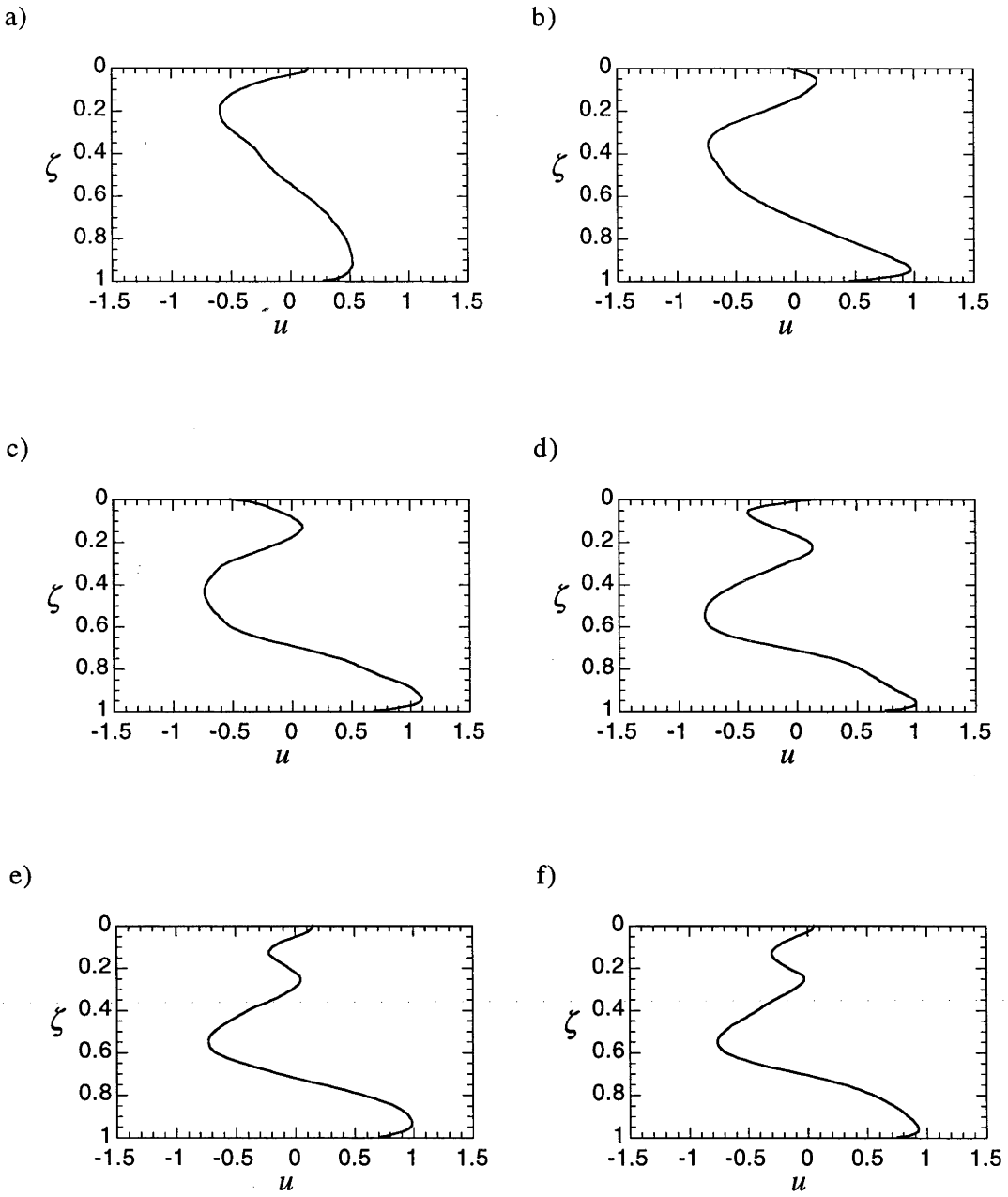

Figure 4.6. The evolution of the baroclinic modes and development of shear layers in a stratified tank initially at rest. These horizontal velocity profiles were taken (a) 2 min, (b) 4 min, (c) 6 min, (d) 8 min, (e) 10 min and (f) 12 min after restarting the plume in experiment 4.8. The establishment of the velocity structures in all the experiments showed the same behaviour, differing only in the time taken to reach the quasi-steady state in (f).

a)

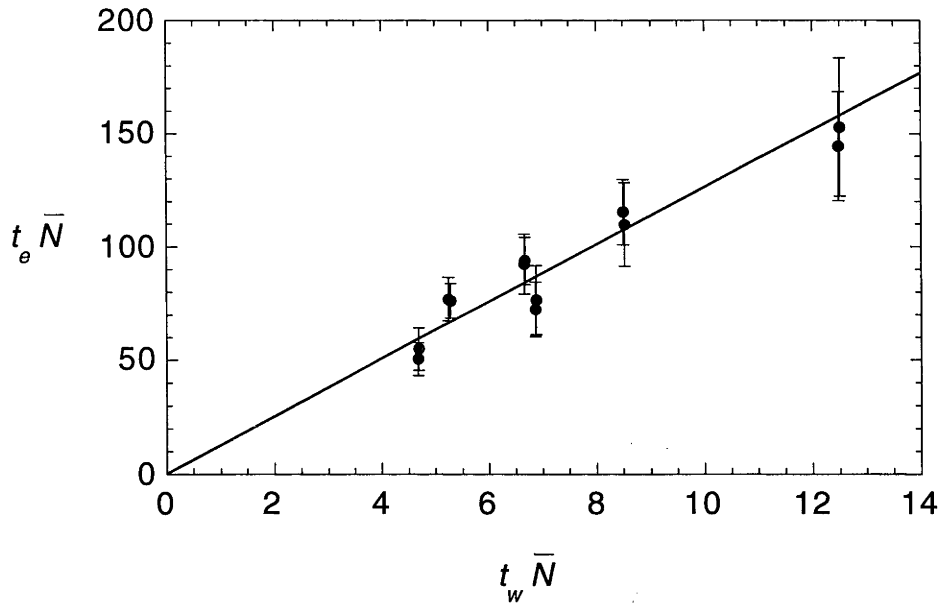

b)

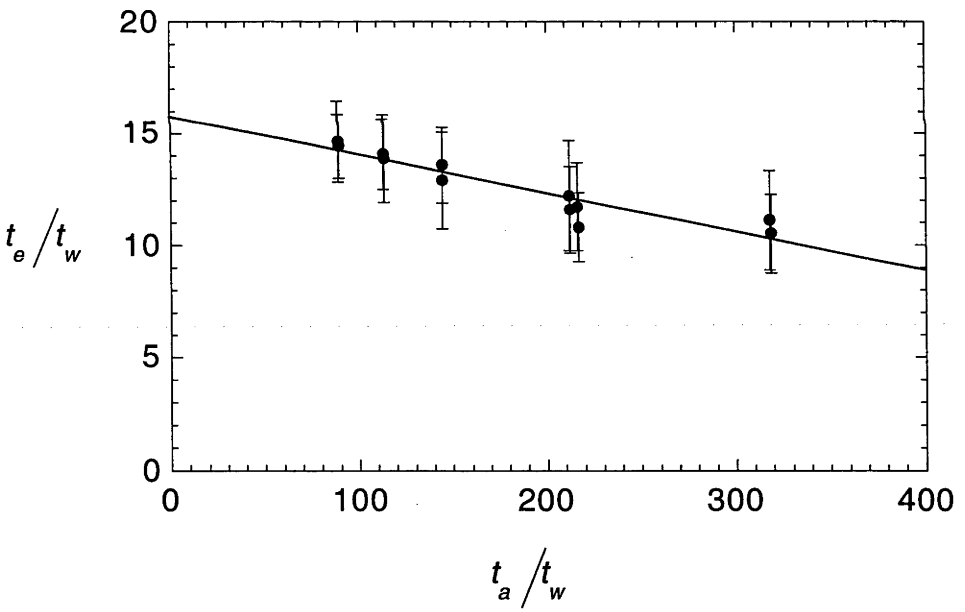

Figure 4.7. Time t_e taken for the velocity structure to evolve to that shown in figure 4.6e. (a) t_e is plotted against t_w, the timescale for long internal waves to travel the length of the tank, both non-dimensionalised by $\overline{N}^{-1}$. (b) t_e is plotted against t_a, the timescale for vertical advection in the "filling-box" model, both non-dimensionalised by t_w. Note that in (a) the abcissa reduces to $t_w \overline{N} = L/H$.

restarted plume had only advected to $\zeta = 0.65$ (and the vertical velocity decays rapidly with height, 2.11a), whereas the velocity structure was already approaching the final quasi-steady state.

4.3.4 The Circulation

The circulation pattern could be broadly divided into three regions. The plume outflow occupied the bottom quarter of the tank ($0.75 < \zeta < 1$) and was a region dominated by convection. The outflow was a gravity current which was not greatly influenced by wave motions in the overlying stratified water. Under the conditions of the experiments, it was also a turbulent layer.

In the experiments, the dimensionless thickness of the outflow layer did not vary significantly despite large variations in the dimensions of the tanks. If the outflow was homogenous, then given the same tank depth and source buoyancy flux, one might expect that the thickness of the outflow layer from a plume would decrease with tank width. However this was not the case (see figure 4.3, where the outflow in experiment 4.2 in a 0.2 m wide tank was actually slightly thinner than that recorded for experiment 4.10 in a 0.3 m wide tank). A possible explanation is that the plume produced water with a range of densities so that the lightest plume water had the same density as the environment water at approximately $\zeta = 0.75$. Thus the least dense plume water started to spread near $\zeta = 0.75$ and the denser plume water below to give a relatively constant dimensionless outflow thickness for all the experiments.

Figure 4.8. The shear layer structure had already developed throughout the tank by the time the dyed outflow from a restarted plume in a previously established density gradient had been advected to $\zeta = 0.65$.

The central region of the water column ($0.15 < \zeta < 0.75$) was dominated by baroclinic modes generated by internal gravity waves and comprised at least three velocity extrema. The motions in this region were laminar and less rapid than in the underlying plume outflow from which they derived their energy. The plume outflow set the dominant vertical scale corresponding to four to six shear layers in the whole tank. This central region experienced the greatest effects of entrainment into the plume. The entrainment velocity opposed the flow in the third shear layer from the bottom and reduced its velocity to almost zero relative to the tank. The region also exhibited the greatest low frequency time-variability in horizontal motion, with periodic reversals in direction and accompanying fluctuations in the density gradient at some depths.

The region very close to the surface ($0 < \zeta < 0.15$) was characterised by a small horizontal velocity towards the plume. The amplitude of horizontal motion associated with the baroclinic modes was smaller at these depths than was the motion u_e caused by entrainment into the plume, even though $u_e \rightarrow 0$ at the surface. This was the region where both the buoyancy frequency and vertical wavenumber in the velocity field (see §4.4) was largest. The velocity structure was also the most variable with time. In the experiments it was sometimes unidirectional and at other times two or three distinct velocity extrema were evident, corresponding to counterflowing shear layers superimposed on the entrainment flow toward the plume.

4.4. Normal Modes

4.4.1 Inviscid Baroclinic Normal Modes

For the "filling-box" density profile defined by (2.12), the first eight baroclinic modes were calculated numerically, neglecting the effects of viscosity and the relatively small velocities associated with entrainment and vertical advection. In this and the following section, x is the distance along the tank, y the height from the bottom, and u and w the usual velocities. With ρ' and p' small perturbations of the density and pressure field respectively, the equations of motion are exactly the same as in (2.14). Following Gill (1982), w and p' can be separated into

$$w = \hat{h}(y)\tilde{w}(x,t) \qquad \text{and} \qquad p' = \hat{p}(y)\tilde{\eta}(x,t).$$

Here, $\hat{h}$ and $\hat{p}$ are the vertical displacement and pressure respectively while $\tilde{w}$ has units of inverse time and $\tilde{\eta}$ is dimensionless. With these variables and using the hydrostatic approximation, (2.14) is separated and reduced to

$$\frac{d^2\hat{h}}{dy^2} + \frac{N^2}{c_n^2}\hat{h} = 0, \tag{4.3a}$$

$$c_n^2 \rho_0 \frac{d\hat{h}}{dy} = \hat{p}, \tag{4.3b}$$

$$\frac{\partial \tilde{w}}{\partial t} - c_n^2 \frac{\partial^2 \eta}{\partial x^2} = 0 \tag{4.3c}$$

and

$$\tilde{w} = \frac{\partial \tilde{\eta}}{\partial t}, \tag{4.3d}$$

where c_n is a separation constant. There is an infinite sequence of descending eigenvalues c_n, each of which corresponds to an eigenfunction (normal mode) with the relevant boundary conditions being rigid, but free-slipping top and bottom. The solutions to $\hat{h}$ and $\hat{p}$ are calculated numerically from (4.3a) and (4.3b). Meanwhile, (4.3c) and (4.3d) indicate that $\tilde{\eta}$ satisfies the wave equation. A solution to $\tilde{\eta}$ and $\tilde{w}$ has the form

$$\tilde{\eta} = A\sin(kx + \omega t)$$

and (4.4)

$$\tilde{w} = A\omega\sin(kx + \omega t),$$

where the frequency ω is related to the horizontal wavenumber k by $\omega^2 = c_n{}^2 k^2$. Note that k (and hence ω) depends on the length of the tank and the horizontal mode of the waves. The horizontal velocity is also separable in the form

$$u = \frac{\hat{p}(y)}{g\rho_0(y)}\tilde{u}(x,t)$$

and can be calculated from the solution to (4.3). For an infinitely long tank where the frequency is zero, $\tilde{w}$, $\tilde{\eta}$, and $\tilde{u}$ do not vary with time so that for fixed x, the horizontal velocity is proportional to $\hat{p}(y)/g\rho_0(y)$. Figure 4.9 gives the functional dependence of u on the dimensionless depth ζ for the first eight modes in this situation. It shows that for

the nth mode there are $n + 1$ shear layers (or velocity extrema) whose thicknesses decrease toward the top of the tank. However, the very small vertical scales of motion near the top of the stratification are expected to be removed by effects of viscosity and I focus on the region $0.05 < \zeta < 1$, where for $4 \leq n \leq 8$, the nth mode has $n - 1$ velocity extrema.

In the experiments the modes that were excited most strongly at asymptotically large times were those that had vertical length scales at the bottom of the tank similar to the plume outflow depth. The measured horizontal velocity profiles (figure 4.3) in the region $0.1 < \zeta < 1$ are qualitatively similar to the velocity structures of the sixth, seventh and eighth inviscid modes except that the amplitudes of the horizontal velocities increase with height in the latter. In particular, the third and fourth horizontal velocity extrema of the $n = 7$ mode lie at $\zeta = 0.35$ and $\zeta = 0.19$, consistent with the experimental observations. This mode also corresponds to six shear layers, as was commonly observed. In contrast, the structures of the lower modes ($n = 1$ to 4) were seen only at short times after the plume was started in the pre-established stratification (§4.3.3). The observations were therefore consistent with the early appearance, particularly in the upper half of the water column, of the most rapidly propagating lower modes and with the later appearance of the slower propagating modes that were the most strongly excited. On the other hand, the measured horizontal velocities decay with height, whereas the calculated baroclinic modes have amplitudes that increase with height as a result of the nonlinear density gradient. The difference can be attributed to effects of viscous dissipation which act most strongly on the smaller vertical scales characteristic of the higher baroclinic modes and in the upper, more highly stratified levels of the box. I look more closely at viscous effects in the next section. Side-wall dissipation in the long channels will further contribute to this decay.

For each normal mode, (4.3c) indicates that the eigenvalue c_n is the wave speed for the associated x- and t-dependent oscillations of u and w. It is assumed that the mode of oscillation in the horizontal is the fundamental mode having wavenumber $k = \pi/L$. The

a)

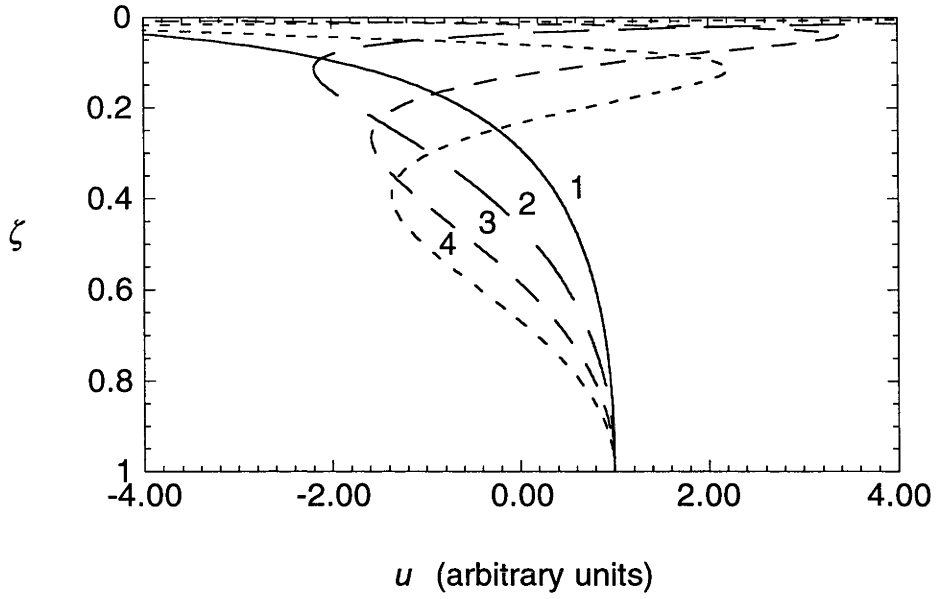

b)

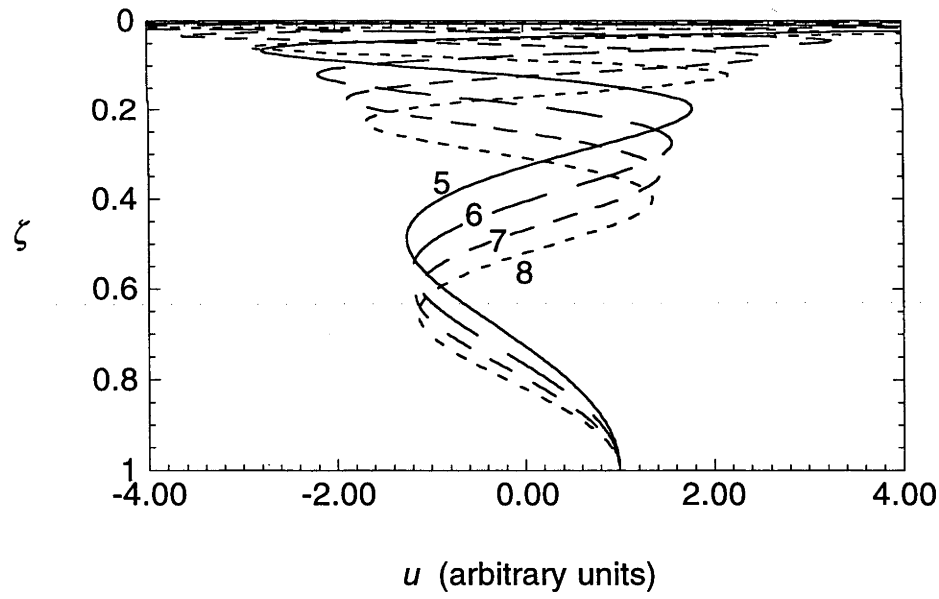

Figure 4.9. Inviscid baroclinic normal modes calculated for the plume stratification (2.12). (a) The first four modes and (b) the next four modes. The horizontal velocities have been normalised to give the same value at the bottom.

period T_n of oscillation in each normal mode can then be calculated. Table 4.2 gives the values of c_n and T_n for each of the first eight normal modes for the conditions of experiment 4.10. It shows that the modes excited most strongly (the experiments indicate that these are $n = 6, 7, 8$) have periods of approximately five to seven minutes. Beating periods between the sixth and seventh modes and between the seventh and eighth modes are approximately 70 and 95 minutes respectively. The beating period is approximately twice the oscillation period of layers t_o observed in the experimental velocity fields. This suggests that the low-frequency oscillations seen in the circulation involved a nonlinear interaction of two consecutive normal modes.

The above analysis for normal modes in a box of finite length predicts that the horizontal velocities (after subtracting that due to entrainment into the plume) should oscillate in direction (4.4). This was not observed because the bottom outflow from the plume must remain approximately constant in time. Only after the plume was stopped were the motions seen to sometimes reverse. Thus the horizontal velocity structure of figure 4.9, calculated for an infinitely long tank, is expected to be qualitatively valid for finite tanks provided the plume outflow is maintained.

Mode	Eigenvalue	Period of horizontal oscillations
n	c_n (m s^{-1})	T_n (s)
1	0.0331	66.4
2	0.0203	109
3	0.0140	157
4	0.0106	208
5	0.00843	261
6	0.00701	314
7	0.00600	367
8	0.00525	419

Table 4.2. The eigenvalues and periods of horizontal oscillations for the first eight normal modes of experiment 4.10.

4.4.2 Effects of Viscosity on Horizontal Velocities

In this section I examine how viscosity modifies the baroclinic modes. Again, I disregard the entrainment of water into the plume and the vertical advection of the environment. I assume that a disturbance at the bottom of the tank supplies the energy required to develop and sustain the horizontal velocities of the baroclinic normal modes. The energy is transported vertically by waves propagated from the bottom while the momentum of the horizontal flow is slowly dissipated through viscous effects. In the analysis of this section I calculate how fast energy is dissipated and predict how the velocities should decay with height.

From the inviscid solution, it is clear that the vertical scale of the shear layers decreases with height because of increasing buoyancy frequency $N(y)$. Let $h(y)$ represent a vertical scale equivalent to half the vertical wavelength of the wave in the dominant mode. Thus $h(y)$ is approximately the thickness of the shear layer at y, but as $h(y)$ is a continuous function which decreases monotonically with y, it will, in general, not represent the exact thickness of the shear layer at a given height.

I now estimate the vertical speed of energy propagation c_{g_y} (see §2.3) in the ray extending upwards and toward positive x from a disturbance at the bottom. With internal waves, the frequency ω remains unchanged along a ray so that, if $\theta(y)$ represents the angle between the horizontal and the wave vector $\boldsymbol{k}(y) = (k(y), m(y))$, then

$$\omega = N(y)\cos\theta(y) = N(y)\frac{k(y)}{|\boldsymbol{k}(y)|} = N(y)\frac{k(y)}{\left(k^2(y)+m^2(y)\right)^{1/2}} = \text{constant}.$$

Here, the vertical wavenumber $m(y) = -\pi/h(y)$ (the negative sign is for the upward propagating ray). I assume that only the fundamental mode is important in the horizontal (to satisfy the boundary conditions at the side walls) so that the horizontal wavenumber $k(y) = \pi/L$. Because horizontal scales are much larger than vertical scales ($k(y) << |m(y)|$), this suggests that $\omega \approx N(y)k(y)/|m(y)|$ is approximately constant. Therefore, at any height y,

$$N(y)h(y) \approx N_0 h_0, \tag{4.5}$$

where $N_0 = N(0)$ and $h_0 = h(0)$. It also follows that

$$m(y) \approx -\frac{\pi N(y)}{N_0 h_0}$$

and from (2.20),

$$c_{g_y}(y) = -\frac{N(y)}{|k(y)|}\sin\theta(y)\cos\theta(y) \approx \frac{N(y)k(y)}{m^2(y)} \approx \frac{N_0^2 h_0^2}{\pi L N(y)}. \qquad (4.6)$$

Therefore, (4.5) and (4.6) indicate that if h_0 and $N(y)$ are known, then estimates for $h(y)$ and $c_{g_y}(y)$ can be deduced immediately. For the other ray extending upward towards negative x where $k(y) = -\pi/L$, $c_{g_y}(y)$ is also calculated as (4.6).

The horizontal velocity profiles of the inviscid baroclinic normal modes exhibit oscillatory behaviour. The experiments also indicated that the amplitudes of the velocities decayed with height. Therefore I assume that the horizontal velocity is of the form of an attenuated sinusoidal function

$$u(y) = A(y)\sin\left(\frac{\pi}{h(y)}y\right), \qquad (4.7)$$

where $A(y)$ and $h(y)$ vary slowly in y relative to $u(y)$. Equation (4.5) gives $h(y)$; to find $A(y)$, Batchelor (1967, p152) implies that the rate of work done by viscous forces is

$$W = \rho_0 \upsilon \frac{\partial u_i}{\partial x_j}\left(\frac{\partial u_i}{\partial x_j} + \frac{\partial u_j}{\partial x_i}\right)$$

$$\approx \rho_0 \upsilon \left(\frac{\partial u}{\partial y}\right)^2, \qquad (4.8)$$

where υ is the kinematic viscosity. I consider the evolution of energy K per unit mass as it propagates vertically with the group velocity c_{g_y}. Equation (4.8) then gives

$$\frac{DK}{Dt} \approx \frac{\partial K}{\partial y}\frac{dy}{dt} = -W = -\rho_0 \upsilon \left(\frac{\partial u}{\partial y}\right)^2$$

and thus

$$c_{g_y}\frac{\partial K}{\partial y} = -\rho_0 \upsilon \left(\frac{\partial u}{\partial y}\right)^2. \qquad (4.9)$$

Consider one shear layer of vertical lengthscale $h(y)$. As $A(y)$, $h(y)$ and $c_{g_y}(y)$ vary much more slowly in y compared with $u(y)$, I introduce a long lengthscale y' over which $K(y')$, $h(y')$, $A(y')$ and $c_{g_y}(y')$ change significantly and a short lengthscale y over which only $u(y)$ varies significantly. To obtain an expression for the variation of $A(y')$, I

integrate (4.9) over a shear layer of depth $h(y')$ and obtain

$$c_{g_z}\frac{\partial}{\partial y'}\int_{h(y')}K=-\rho_0\upsilon\int_{h(y')}\left(\frac{\partial u}{\partial y}\right)^2.$$

With $K = 1/2\ \rho_0 u^2$, this gives the energy change due to viscosity in a shear layer as

$$c_{g_y}\frac{\partial}{\partial y'}\int_{h(y')}\frac{1}{2}\rho_0 A^2(y')\sin^2\left(\frac{\pi}{h(y')}y\right)dy\approx-\rho_0\upsilon\int_{h(y')}A^2(y')\cos^2\left(\frac{\pi}{h(y')}y\right)\left(\frac{\pi}{h(y')}\right)^2dy,$$

which may be rearranged to give

$$\frac{\partial}{\partial y'}\left\{A^2(y')h(y')\right\}\approx-\frac{2\upsilon\pi^2}{c_{g_y}h(y')}A^2(y').$$

Using (4.5) and (4.6) and dropping dashes, this becomes

$$\frac{\partial}{\partial y}\left(\frac{A^2(y)}{N(y)}\right)\approx-\frac{2\upsilon\pi^3L}{N_0^4h_0^4}A^2(y)N^2(y), \tag{4.10}$$

to which the solution for the amplitude function $A(y)$ is

$$A^2(y)\approx C\,N(y)\exp\left\{-\frac{2\upsilon\pi^3L}{N_0^4h_0^4}\int N^3(y)dy\right\}, \tag{4.11}$$

where C is a constant of integration. The definition of y gives $\zeta = (H - y)/H$ so that the power series expansion (to three terms) for $N(y)$ obtained from (2.4) and (2.12) is

$$N(y)=\frac{F^{1/3}}{2^{2/3}E^{2/3}\pi^{1/3}H^{4/3}}\left\{2.18\left(\frac{H-y}{H}\right)^{-5/3}+0.279\left(\frac{H-y}{H}\right)^{-2/3}+0.0831\left(\frac{H-y}{H}\right)^{1/3}+\ldots\right\}^{1/2}$$

$$=\frac{F^{1/3}}{2^{2/3}E^{2/3}\pi^{1/3}H^{4/3}}n\left(\frac{H-y}{H}\right),$$

where

$$n\left(\frac{H-y}{H}\right)=1.48\left(\frac{H-y}{H}\right)^{-5/6}+0.0945\left(\frac{H-y}{H}\right)^{1/6}+0.0251\left(\frac{H-y}{H}\right)^{7/6}+\cdots$$

and hence

$$\int N^3(y)dy=\frac{F}{4E^2\pi H^3}\left(2.15\left(\frac{H-y}{H}\right)^{-3/2}+1.24\left(\frac{H-y}{H}\right)^{-1/2}-0.408\left(\frac{H-y}{H}\right)^{1/2}+\cdots\right)+c.$$

The solution (4.11) for the amplitude $A(y)$ can be expressed in dimensionless form $a(y) = A(y)/A(0)$ as

$$a(y) \approx \left(\frac{N(y)}{N_0}\right)^{1/2} \exp\left\{-\frac{\upsilon\pi^3 L}{N_0^4 h_0^4}\int_0^z N^3(y^*)dy^*\right\}$$

$$\approx \left(\frac{n\left(\frac{H-y}{H}\right)}{n(1)}\right)^{1/2} \exp\left\{\frac{\upsilon\pi^3 L}{H^3}\frac{2^{2/3}E^{2/3}\pi^{1/3}H^{4/3}}{F^{1/3}}\left(\frac{H}{h_0}\right)^4 \frac{1}{n^4(1)}\left(2.98 - 2.15\left(\frac{H-y}{H}\right)^{-3/2}\right.\right.$$

$$\left.\left. -1.24\left(\frac{H-y}{H}\right)^{-1/2} + 0.408\left(\frac{H-y}{H}\right)^{1/2} + \cdots\right)\right\},$$

or equivalently, using the dimensionless depth ζ,

$$a(\zeta) \approx 0.791\left(1.48\zeta^{-5/6} + 0.0945\zeta^{1/6} + 0.0251\zeta^{7/6} + \cdots\right)^{1/2} \exp\left\{\frac{\upsilon\pi^3 L}{H^3}\frac{2^{2/3}E^{2/3}\pi^{1/3}H^{4/3}}{F^{1/3}}\right.$$

$$\left.\frac{H^4}{h_0^4}\left(0.455 - 0.328\zeta^{-3/2} - 0.189\zeta^{-1/2} + 0.0623\zeta^{1/2} + \cdots\right)\right\}. \qquad (4.12)$$

For the plume experiments, the thickness of the plume outflow layer is approximately one quarter of the depth of the tank. However h_0 must be greater than the observed thickness of the plume outflow layer because $h(y)$ is a monotonic decreasing function for increasing height. Figure 4.10 gives plots of $a(\zeta)$ for the parameters of experiment 4.10 with h_0/H = 0.25 and 0.35. It will be seen below that the estimate h_0/H = 0.35 produces a horizontal velocity profile with a bottom layer that has thickness close to $H/4$.

In order to show the significance of the increasing buoyancy frequency with height I also give an approximate solution $A_1(y)$ to (4.10) that assumes $N(y) = N_0$. This solution, expressed as $a_1(y) = A_1(y)/A_1(0)$, is

$$a_1(y) = \exp\left\{-0.625\frac{\upsilon\pi^3 L}{H^3}\frac{2^{2/3}E^{2/3}\pi^{2/3}H^{4/3}}{F^{1/3}}\frac{H^4}{h_0^4}\frac{y}{H}\right\} \qquad (4.13)$$

and has the same dependence on the parameters of the experiment and h_0/H as $a(y)$. Figure 4.10 gives plots of (4.13) as a function of the dimensionless depth ζ for the parameters of experiment 4.10 using h_0/H = 0.25 and 0.35.

As expected, both the energy attenuation function $a(\zeta)$ and its approximation $a_1(\zeta)$ show that horizontal velocities decay with height. The rapid decay rate for smaller vertical scales is due to greater loss of energy in shear layers of smaller thickness, where the

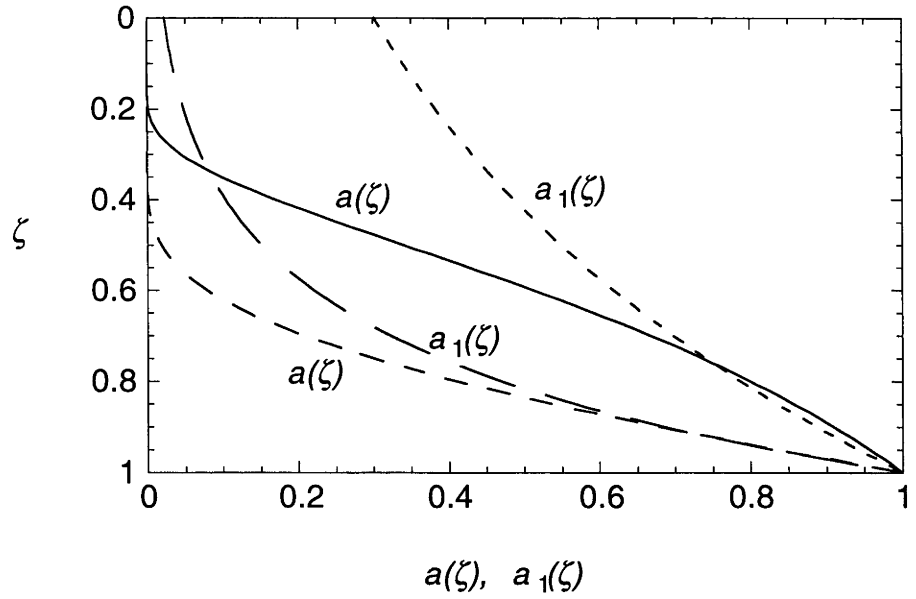

Figure 4.10. The normalised velocity attenuation function $a(\zeta)$ from (4.12) and the approximation $a_1(\zeta)$ from (4.13) for the parameters of experiment 4.10 and using two estimates of h_0/H. For $a(\zeta)$: h_0/H = 0.25 (— — — —), h_0/H = 0.35 (————————) and for $a_1(\zeta)$ h_0/H = 0.25 (—— ——), h_0/H = 0.35 (- - - - - - - - -).

velocity gradients are larger. The increase in buoyancy frequency with height also contributes to more rapid attenuation through a corresponding decrease in vertical scale; figure 4.10 shows that $a(\zeta)$ decays more rapidly than $a_1(\zeta)$.

Plots of $u(\zeta)/A_{\zeta=1} = a(\zeta)\sin(\pi H(1-\zeta)/h)$ are given in figure 4.11 for h_0/H = 0.25 and 0.35 to show the shape of the horizontal velocity profile expected for experiment 4.10. The horizontal velocity profile corresponding to h_0/H = 0.35 more closely resembles that observed in figure 4.3. Note that the predicted thickness of the plume outflow layer is a quarter of the total depth. The profile also contains velocities that have decayed significantly within the depth of the tank and has approximately six shear layers, consistent with the experiments.

Both (4.12) and (4.13) are, however, extremely sensitive to h_0/H since very small changes in h_0/H can result in noticeably different attenuation rates. Although smaller values of h_0/H result in a faster decay of $a(\zeta)$, the rate of attenuation is also dependent on

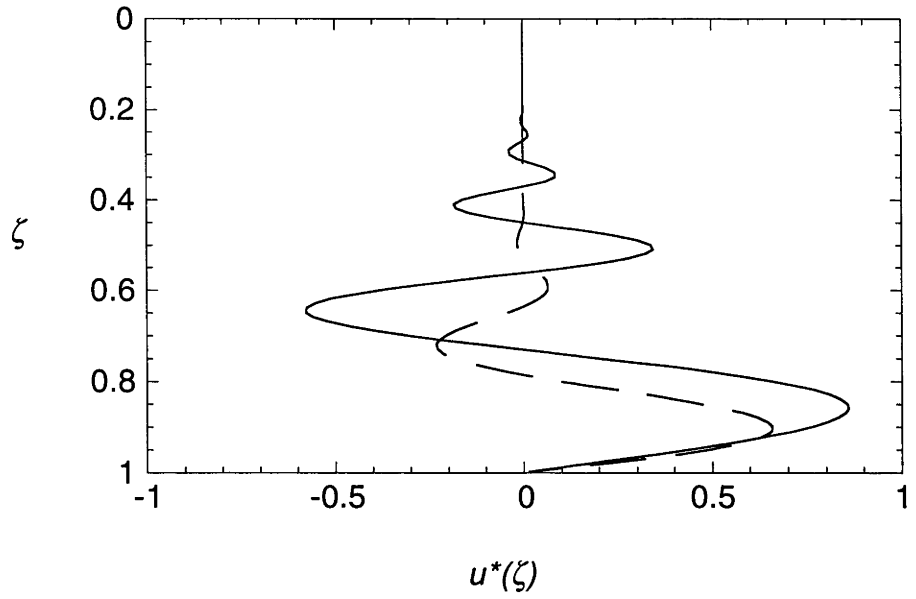

Figure 4.11. The normalised horizontal velocity $u^*(\zeta) = u(y)/A(0)$ for the parameters of experiment 4.10 as given by (4.7) and using the attenuation function (4.12). Two values of h_0/H are used: — — — — for $h_0/H = 0.25$ and ———— for $h_0/H = 0.35$.

the dimensionless parameter

$$s = \frac{\upsilon\pi^3 L}{H^3} N_*^{-1},$$

where $N_* = F^{1/3}2^{-2/3}E^{-2/3}\pi^{-1/3}H^{-4/3}$, the scaling factor for N. Larger values of s give increased attenuation rates with height, so that longer tank lengths, smaller tank depths and weaker buoyancy fluxes (resulting in weaker stratification) should result in greater decay of velocity. In the experiments, s lies in the range of 0.0209 to 0.0617 with the exception of experiments 4.1 and 4.5 where it is larger (up to 0.112). Except for experiments with very small depths (H = 0.16 m), where the horizontal velocities were noted to decay quickly in comparison with the other experiments, no clear trend in attenuation rates was seen. Given the sensitivity of $a(\zeta)$ to h_0/H, perhaps any such trends in the attenuation rate were hidden by possible small variations in h_0/H between experiments.

The effects of plume entrainment and vertical advection in the environment can now be qualitatively discussed. At shallow depths, where the horizontal velocities attributed to waves are in magnitude smaller than or comparable to the entrainment velocity, the water may be seen as a single region moving slowly towards the plume and therefore fewer layers are detected. In addition, vertical advection in the environment is likely to transport layers upwards, reducing the apparent attenuation rate of the horizontal motions. These features may be factors in the discrepancy between the calculated horizontal velocities of figure 4.11 and the observed velocity of experiment 4.10 in figure 4.3a.

4.5 Discussion and Conclusion

4.5.1 Comparisons With Other Shear Flows

The horizontal shear layers found in the plume experiments show similarities to the circulation observed in several other systems. Imberger, et al. (1976) studied experimentally and numerically the two-dimensional flow resulting from the withdrawal and intrusion of fluid from mid-depth in an uniformly stratified tank. They studied a variety of cases based on a parameter $R = Q(NL^2/\upsilon)^{2/3}/NL^2$, which is the product of the Froude number and one-third power of the Grashof number (Q is the volume flux per unit width). For the case where $R > 1$ (supercritical flow dominated by buoyancy and inertia with relatively unimportant viscous effects) they showed that convection was the dominant force behind the flow and that internal waves propagated vertically until the induced flow was equal and opposite to their phase velocity. Manins (1976) studied intrusions into a linearly stratified fluid for $100 < Re < 500$ (where Re is the Reynolds number). These intrusions were governed by an inertia-buoyancy balance and the horizontal velocities above and below the intrusion showed an alternating layer structure in which each of the layers had the same thickness. For comparison, in the present experiments I evaluate $R \sim 10$ (based on the volume flux at the base of the plume and the depth-averaged buoyancy frequency) and $Re \sim 400$ (based on the velocity and depth of the plume outflow layer). Hence it confirms that near the bottom, the "filling-box" flows

are dominated by inertia and buoyancy and are in the same regime as the previous studies of intrusions. However, the value of Re is sufficiently small that viscosity is important in the upper levels where N is much greater.

Stratified flows with very small Froude numbers give qualitatively similar behaviour. For example, Martin and Long (1968) studied the equations describing the flow induced by a thin, flat plate moving slowly and horizontally through a uniformly stratified fluid, resulting in the generation of columnar modes or "upstream wakes". Viscosity played an important part in this flow and the disturbance produced an alternating layer structure with amplitudes decreasing away from the plate, similar to the flow in the experiments. In a related problem, Bretherton (1967) studied the flow generated by a cylinder moving slowly in the horizontal through a stratified fluid. At a large distance ahead of the obstacle a broad velocity profile appeared first due to the arrival of rapidly propagating long wavelength internal gravity waves. Some time later, the arrival of slower waves of short vertical wavelength produced a "plug flow" confined to the vertical extent of the obstacle with velocity reversals above and below. The equivalent Froude number for the experiments here is $16Q/\overline{N}H^2 \sim 0.6$ (based on the outflow height $H/4$). Thus the conclusion in §4.4.2, that viscosity is a strong controlling influence in the upper levels of the water column as a consequence of the increased buoyancy frequency, is consistent with previous studies of viscous upstream columnar wakes.

4.5.2 Conclusion

The stratified environment produced by a turbulent plume supports a series of shear layers superimposed on the steady vertical advection and entrainment-driven horizontal flow into the plume. These layers are the result of a continuous excitation of baroclinic normal modes having vertical length scales set by the depth of the turbulent outflow from the dense plume. The baroclinic modes are established on the timescale for the propagation of internal waves through the box and develop rapidly compared to the ventilation of the box by vertical advection and the rate of change of the "filling-box" stratification in its transient stages. Under the laboratory conditions the gravity current

outflow from the base of the plume is characterised by a moderate-to-low Froude number. Given the large increase in buoyancy frequency towards the top of the "filling-box" density gradient, the conditions imply that viscosity becomes a controlling influence on the upward momentum flux and causes the amplitude of horizontal velocities in the shear layers to decrease with increasing height from the base. At large times, when the stratification has achieved its constant shape, the baroclinic modes also undergo a very low frequency oscillation between the five-layer and six-layer states (dominated by modes n = 6 and 7, respectively). It is speculated that this oscillation may be linked to the superposition and beating of two or more baroclinic modes, but its precise nature has not been determined.

The presence of the shear layers is an interesting aspect of the "filling-box" convection. Although they have little effect on the stratification in that the density surfaces are tilted only slightly in connection with the horizontal motion, the circulation pattern will have large implications for the transport of individual water particles and tracers in the system. For example, tracers released from a source at a fixed depth in the water column, or a mid-depth outflow from a second plume produced by a smaller buoyancy flux, will spread laterally under the control of interior flows driven by the strong plume. The mid-depth outflow from a second plume is considered in chapter 6.

Chapter 5

Downslope Plumes

5.1. Introduction

In many practical situations plumes are unable to descend vertically because they encounter sloping floors. The dense outflows from marginal seas often flow down continental slopes beneath less dense water (Price and Baringer, 1994). Katabatic winds in the atmosphere occur when air cooled by contact with a cold ground flows downhill. Much of the theoretical work that models these flows involves two-dimensional (line) plumes placed on a slope (for example, Ellison and Turner, 1959; Smith, 1975; Baines, 1997). Britter and Linden (1980) have also examined the head of a plume travelling down a slope and found that it moved at a slower speed compared with the following flow. This chapter is only concerned with the flow behind the head. Mixing between the plume and the environment occurs only at the upper interface, where entrainment of environment water increases the depth (thickness) of the plume. However if the buoyancy source generating the plume is localised and the plume is not constrained by any side-walls, then the plume can also spread across the slope as it flows downhill. Both the depth and width increase and its structure is three-dimensional. This plume description is similar to those in streamtube models of downslope flows where the current takes the shape of a long pipe that has changing dimensions along the current (see Smith, 1975 or Emms, 1997). The three-dimensional downslope plume can be regarded as a generalisation of both the two-dimensional downslope plume and the vertically-descending axisymmetric plume.

The downslope flows in nature may be combinations of the two-dimensional and three-dimensional cases, depending on the topography of the system. Downslope

plumes, whether two- or three-dimensional, differ from vertically-descending plumes in that their interactions with environment water are mainly restricted to only one side of the plume. The mixing processes in downslope flows are still under active research. In many geophysical applications, downslope flows are also affected by the earth's rotation which acts to turn the flow and can result in boundary currents across the slope. The effects of rotation have been incorporated in the streamtube models of Smith (1975) and Emms (1997). However, the present study ignores rotation and the plume descends along the slope at all times. This non-rotating downslope plume is an extension to the vertically-descending plume described in chapter 2.

The two-dimensional downslope plume without rotation is reviewed and extended to a "filling-box" model in §5.2, followed by a new model of the three-dimensional downslope plume in §5.3. Experiments to test the predictions of the three-dimensional plume model are described in §5.4, with the results for a limited number of experiments on 30° and 45° slopes given in §5.5. Discussions on the model and the work required to expand the study into a comprehensive study of non-rotating downslope flows are given in §5.6.

5.2 Two-Dimensional Downslope Plumes

The two-dimensional downslope plume is assumed to be generated by a line source of buoyancy on a frictionless plane that is bounded on both sides by vertical walls. Let the plane be inclined at an angle θ to the horizontal. The plume has a constant width and is uniform across the slope. Let D be the depth (or thickness) of the plume in the plane perpendicular to the slope, W the downslope velocity, ρ_p the plume density, ρ_e the environment density and ρ_r a reference density, with s the distance down the slope and t the time. Ellison and Turner (1959) deduced that because the sloping floor causes the mixing zone of the plume to be also inclined (and not vertical as in the ordinary plume), there will be a change in the value of the entrainment coefficient. They defined a Richardson number

$$Ri_0 = g\left(\frac{\rho_p - \rho_e}{\rho_r}\right)\frac{D\cos\theta}{W^2}, \tag{5.1}$$

which is a measure of the stabilising effect of the density gradient relative to the shear over the cross-section of the plume. They asserted that, provided the Reynolds number is sufficiently large and the density differences between the plume and its surroundings are small, the entrainment coefficient E is a function only of Ri_0. The Richardson number is equal to the inverse square of the internal Froude number.

The equations for a two-dimensional downslope plume representing the conservation of volume, momentum and density excess are

$$\frac{d}{ds}(DW) = EW, \tag{5.2a}$$

$$\frac{d}{ds}\left(DW^2\right) = Dg\left(\frac{\rho_p - \rho_e}{\rho_r}\right)\sin\theta \tag{5.2b}$$

and

$$\frac{d}{ds}\left\{DWg\left(\frac{\rho_p - \rho_e}{\rho_r}\right)\right\} = -DW\frac{d}{ds}\left(g\frac{\rho_e - \rho_r}{\rho_r}\right). \tag{5.2c}$$

Ellison and Turner (1959) also included terms in (5.2b) for the frictional drag of the slope and the pressure force on the plume layer due to its changing depth. The slope is assumed to be frictionless in this study while the pressure force was shown to be relatively unimportant. They also included coefficients representing arbitrary velocity and density profiles in the plume; in the present study, a top-hat profile has been used.

For a plume descending into a homogenous environment, the right hand side of (5.2c) vanishes. It follows from (5.1) and (5.2) that

$$\frac{dD}{ds} = 2E - Ri_0\tan\theta \tag{5.3a}$$

and

$$\frac{D}{3Ri_0}\frac{dRi_0}{ds} = E - Ri_0\tan\theta. \tag{5.3b}$$

For a given θ, there is a particular value of Ri_0 called the normal value, Ri_n, for which the right hand side of (5.3b) vanishes to give a constant Richardson number and entrainment coefficient $E = Ri_n\tan\theta$. Ellison and Turner (1959) asserted that if $Ri_0 < 1$ and different

from Ri_n at the start, then the flow adjusts rapidly to the "normal" state where $Ri_0 = Ri_n$. Thus if the flow starts too slowly, then gravity accelerates it and if it starts too fast, then increased mixing occurs and it slows down. Thus for these downslope plumes, Ri_0 attains Ri_n in a short distance and E is constant for the rest of the slope. In this homogenous environment, the solution to (5.2) can be found as

$$D = Es,$$

$$W = E^{1/3} F^{1/3} \sin^{1/3}\theta$$

and (5.4)

$$g\left(\frac{\rho_p - \rho_e}{\rho_r}\right) = E^{-2/3} F^{2/3} \sin^{-1/3}\theta \, s^{-1},$$

where $F = DWg\,(\rho_p - \rho_e)/\rho_r$ is the buoyancy flux of the source at $s = 0$. An interesting feature of this solution is that the downslope velocity is constant.

Experiments were performed by Ellison and Turner (1959) to measure $E(Ri_0)$ using two methods. The first established E from measurements of the changing volume flux of a jet of initially fresh water flowing on the surface of a body of salt solution while the second measured E similarly from observations of a salt solution flowing down the sloping floor of a channel beneath fresh water. Both showed that E falls off rapidly as Ri_0 increases. The second series of experiments also established the relationship between θ and E (figure 5.1).

In a finite box, the outflow of a downslope plume displaces the environment upward and establishes a stratification. The equation representing the vertical advection of the environment and change in environment buoyancy is

$$\frac{\partial}{\partial t}\left(g\frac{\rho_e - \rho_r}{\rho_r}\right) = \frac{DW\sin\theta}{L}\frac{\partial}{\partial z}\left(g\frac{\rho_e - \rho_r}{\rho_r}\right), \tag{5.5}$$

where z ($= s\sin\theta$) is the vertical distance from the source and L is the length of the box. It is assumed that L is large so that, despite the slope, the box length is approximately independent of z.

The mixing processes are not well understood for downslope plumes in stratified environments. The Richardson number is also expected to vary downslope because of

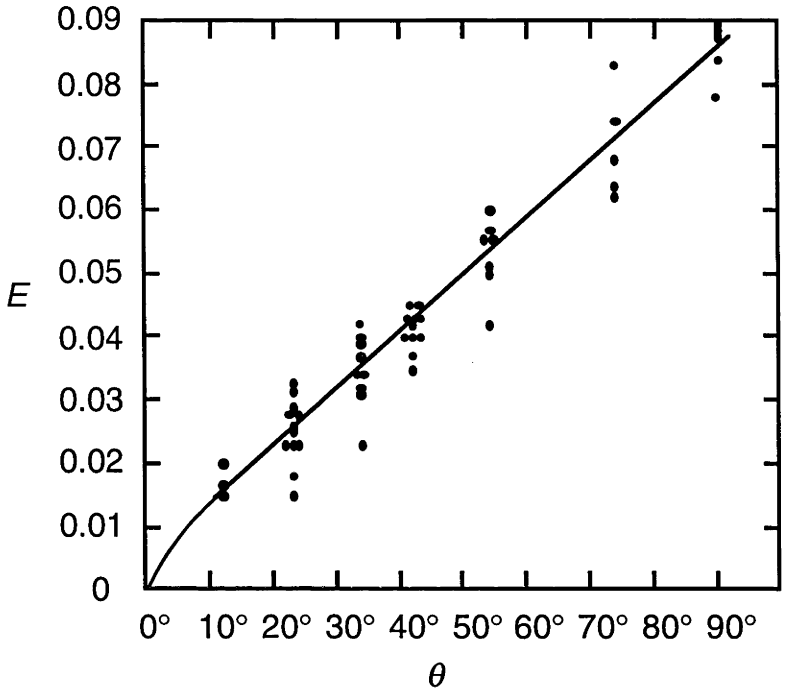

Figure 5.1. The entrainment coefficient for a two-dimensional inclined plume as a function of slope θ (taken from Ellison and Turner, 1959).

the changing density of the environment and hence will result in changes to the entrainment coefficient. A simplification used by Killworth (1977) and Baines (1997) in a stratified environment assumed that E is constant for a given slope. Baines (1997) found that this assumption was broadly consistent with his experimental observations. If it is assumed that E is constant in the "filling-box" case, then the scalings

$$\begin{aligned} z &= s\sin\theta = H\zeta, \\ t &= E^{-2/3}F^{-1/3}L\sin^{-1/3}\theta, \\ D &= EH\sin^{-1}\theta\, d, \\ W &= E^{-1/3}F^{1/3}\sin^{1/3}\theta\, w, \\ g\left(\frac{\rho_p-\rho_r}{\rho_r}\right) &= E^{-2/3}H^{-1}F^{2/3}\sin^{2/3}\theta\, f_p, \\ g\left(\frac{\rho_e-\rho_r}{\rho_r}\right) &= E^{-2/3}H^{-1}F^{2/3}\sin^{2/3}\theta\, f_e \end{aligned} \tag{5.6}$$

can be used to reduce (5.2) and (5.5) to their dimensionless form

$$\frac{d}{d\zeta}(dw) = w, \tag{5.7a}$$

$$\frac{d}{d\zeta}\left(dw^2\right) = \left(f_p - f_e\right)d, \tag{5.7b}$$

$$\frac{d}{d\zeta}\left\{dw\left(f_p - f_e\right)\right\} = -dw\frac{df_e}{d\zeta} \tag{5.7c}$$

and

$$\frac{\partial f_e}{\partial \tau} = dw\frac{\partial f_e}{\partial \zeta}. \tag{5.7d}$$

Equation (5.7) is identical to that found by Baines and Turner (1969) for vertically-descending line plumes. They presented power series solutions to (5.7) in the asymptotic case where d, w and $f_p - f_e$ are constant at a given ζ, but f_p and f_e increase linearly with time for all ζ. The solution to three terms is given by

$$d = \zeta + 0.125\zeta^2 + 0.0688\zeta^3 + \ldots, \tag{5.8a}$$

$$w = 1 - 0.25\zeta - 0.0563\zeta^2 + \ldots, \tag{5.8b}$$

$$f_p - f_e = \zeta^{-1} - 0.875 - 0.0906\zeta + \ldots \tag{5.8c}$$

and

$$f_e^* = f_e(\tau,\zeta) - f_e(\tau,1) = -0.142 + \log_e \zeta + 0.125\zeta + 0.0172\zeta^2 + \ldots. \tag{5.8d}$$

The quantities d, w, f_p^* $(=f_p(\zeta) - f_p(1))$ and f_e^* are plotted in figure 5.2.

5.3. Three-Dimensional Downslope Plumes

When a downslope plume is generated by a localised source of buoyancy and is not constrained by side-walls, both the width and depth (thickness) change with distance from the source. It is assumed that the plume has a rectangular cross-section with width $2R$, height H and the other variables as defined for the two-dimensional downslope plume (figure 5.3). The streamtube models of Smith (1975) and Killworth (1977) linked the width and depth of the plume together as the cross-sectional area of the plume; however, in this model the width and depth are allowed to vary separately. The equations representing conservation of volume, momentum and buoyancy deficit are

a)

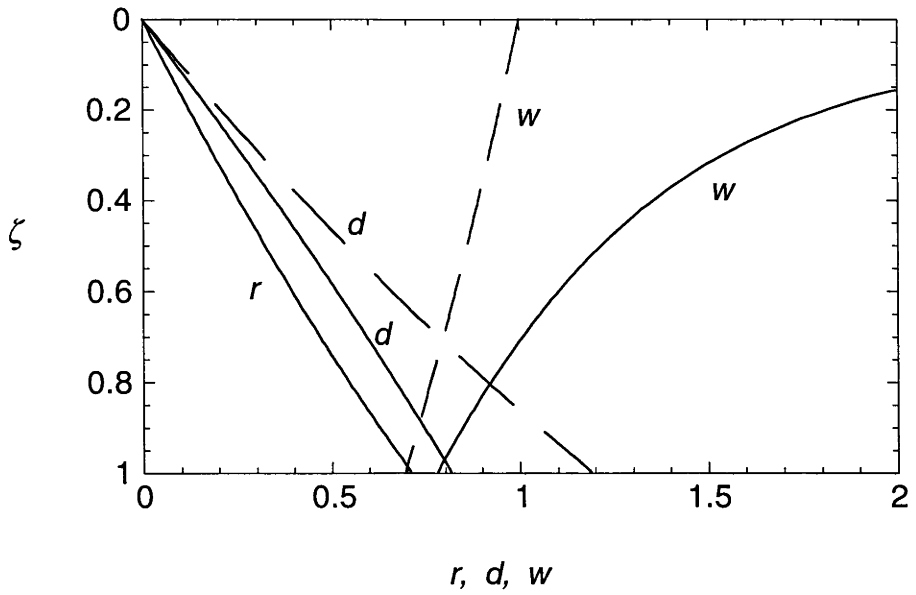

b)

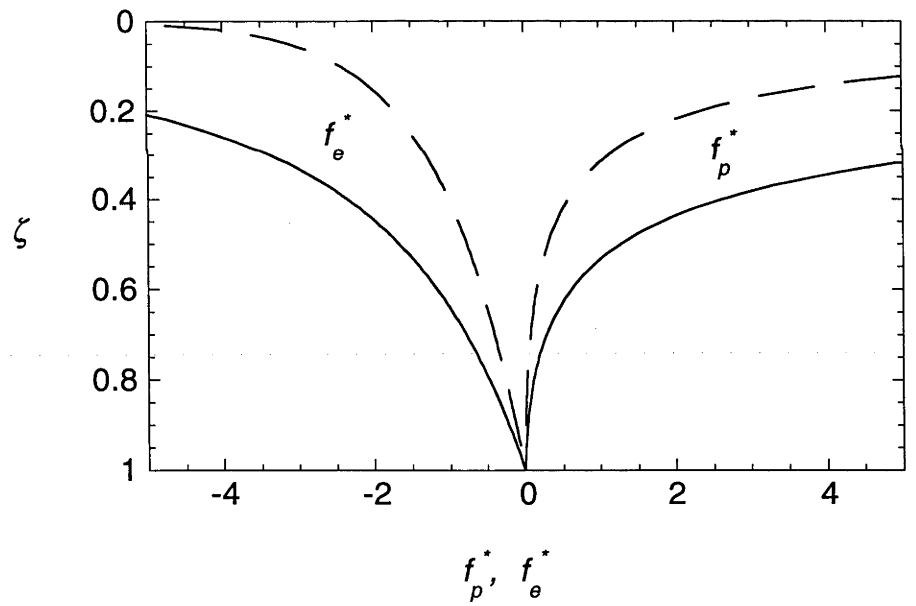

Figure 5.2. The plume properties in the large-time steady state for the two-dimensional (—— ——) plume given by (5.8) and for the three-dimensional (————————) plume given by (5.15). (a) The dimensionless plume width r (three-dimensional case only), depth d and vertical velocity w. (b) The dimensionless plume and environment buoyancies relative to the bottom f_p^* and f_e^* respectively.

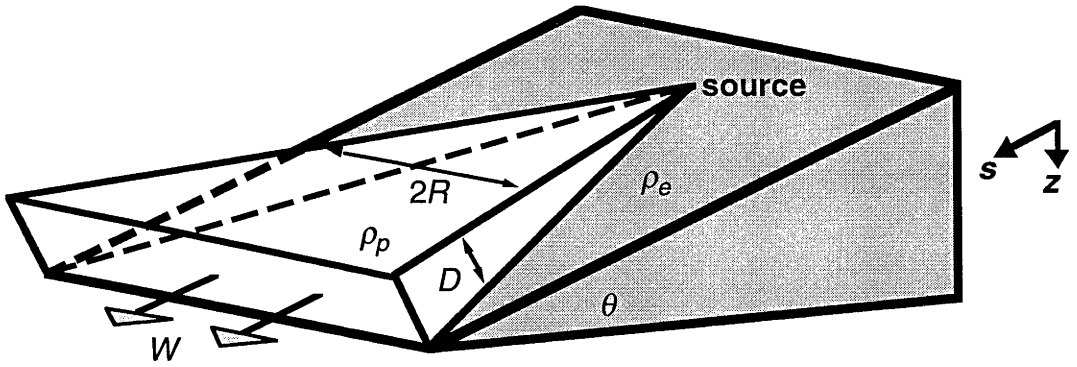

Figure 5.3. The variables used in the theory of a three-dimensional downslope plume: plume half width R, depth (perpendicular to the slope) D, downslope velocity W, plume and environment densities ρ_p and ρ_e.

$$\frac{d}{ds}(2RDW) = 2REW \tag{5.9a}$$

$$\frac{d}{ds}\left(2RDW^2\right) = 2RDg\frac{\left(\rho_p - \rho_e\right)}{\rho_r}\sin\theta \tag{5.9b}$$

and

$$\frac{d}{ds}\left\{2RDWg\left(\frac{\rho_p - \rho_e}{\rho_r}\right)\right\} = -2RDW\frac{d}{ds}\left(\frac{\rho_e - \rho_r}{\rho_r}\right). \tag{5.9c}$$

When the plume is travelling straight down the slope, the increase in width of the plume can be likened to a volume of dense water slumping across the slope in a manner similar to a gravity current (Turner, personal communication). With $g\cos\theta$ the component of gravity responsible for the slumping across the slope, the equation describing the increase in plume width is given by

$$\frac{dR}{dt} = \left(2g\cos\theta\,\frac{\rho_p - \rho_e}{\rho_e}D\right)^{1/2}$$

(Turner, 1973), or equivalently,

$$W\frac{dR}{ds} = \left(2g\cos\theta\,\frac{\rho_p - \rho_e}{\rho_e}D\right)^{1/2}. \tag{5.10}$$

The Richardson number is likely to vary along the slope, but if it assumed that a normal value of Ri_0 is again approached within a short distance of the source, then the entrainment coefficient is effectively constant for a given slope. The solution to (5.9) and

(5.10) in the homogenous environment is then given by

$$R = \frac{2^{3/2} E^{1/2} \cos^{1/2}\theta}{5^{1/2} \sin^{1/2}\theta} s, \tag{5.11a}$$

$$D = \frac{3E}{5} s, \tag{5.11b}$$

$$W = \frac{5^{1/2} F^{1/3} \sin^{1/2}\theta}{2^{3/2} E^{1/2} \cos^{1/6}\theta} s^{-1/3} \tag{5.11c}$$

and

$$g\frac{\rho_p - \rho_e}{\rho_r} = \frac{5F^{2/3}}{6E\cos^{1/3}\theta} s^{-5/3}. \tag{5.11d}$$

Here $F = 2RDWg(\rho_p - \rho_e)/\rho_r$ is the buoyancy flux of the source and is evaluated at $s = 0$. Both the width and depth of the plume are proportional to the distance down the slope and so the behaviour is similar to the vertically-descending axisymmetric plume, where the radius is proportional to the depth. However in the downslope plume, the height and width have different constants of proportionality. Figure 5.4 gives plots of R, D, W and $g(\rho_p - \rho_e)/\rho_r$ from (5.11) for the parameters of an experiment on a 30° slope (experiment 5.1 where $F = 6.64 \times 10^{-6}$ m^4 s^{-3} and $E = 0.0748$; see §5.4 and §5.5). For this case, R is much larger than D.

The entrainment coefficient may be linked to Ri_0 by substituting the solution (5.11) into (5.9a) and (5.9b) to give

$$E = \frac{5}{4} Ri_0 \tan\theta.$$

However, this does not automatically imply that the entrainment constant for a three-dimensional downslope plume is 1.25 times that of the two-dimensional case where $E = Ri_0 \tan\theta$. The normal values of Ri_0 to which the plume approaches rapidly are different in the two cases.

In a filling-box, the equation representing vertical advection in the environment is

$$\frac{\partial}{\partial t}\left(g\frac{\rho_e - \rho_r}{\rho_r}\right) = \frac{2RDW\sin\theta}{A}\frac{\partial}{\partial z}\left(g\frac{\rho_e - \rho_r}{\rho_r}\right), \tag{5.12}$$

where A is the cross-sectional area of the tank and is assumed to be large so that it is effectively constant with z. If it is again assumed that E is constant for a given slope in

a)

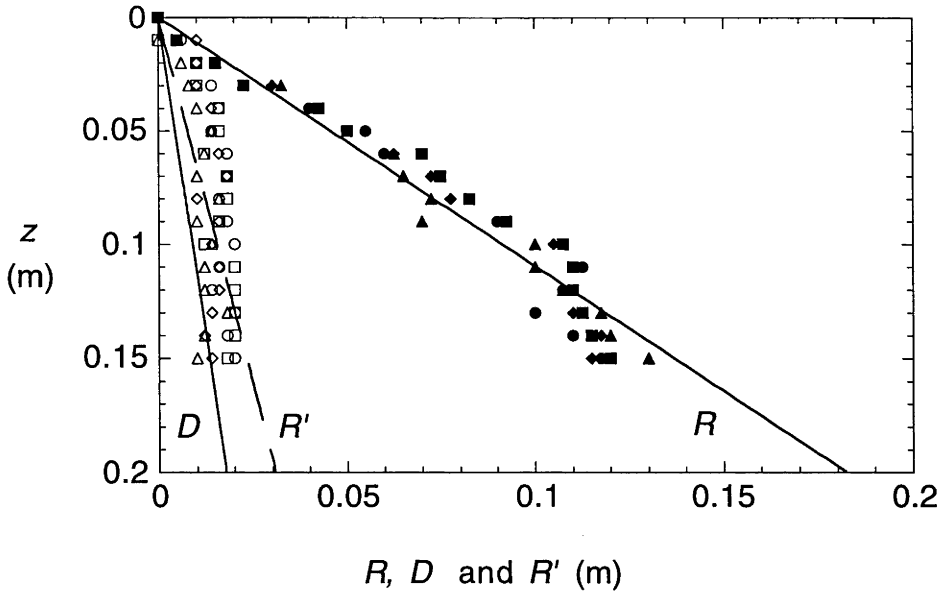

b)

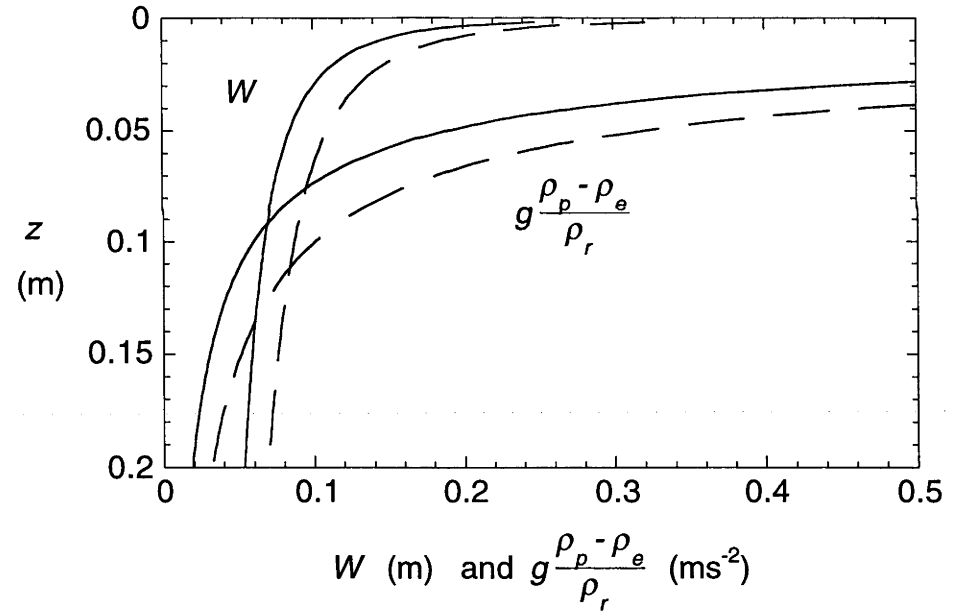

Figure 5.4. The dimensional downslope plume properties in a homogenous environment for the parameters of experiment 5.1 (————————) compared with the vertically-descending axisymmetric plume (—— ——). (a) The plume half width R and depth D in the downslope case and plume radius R' in the vertically-descending case. Also plotted are the data (half width and depth) from experiments 5.1 (● and ○), 5.2 (■ and □), 5.3 (◆ and ◇) and 5.4 (▲ and △). (b) The plume velocities W and buoyancies $g(\rho_p - \rho_e)/\rho_r$ in both cases.

the stratified environment, then (5.9), (5.10) and (5.12) may be non-dimensionalised using the scalings

$$z = s\sin\theta = H\zeta,$$

$$t = \frac{A\sin^{2/3}\theta}{2EF^{1/3}H^{2/3}\cos^{1/3}\theta}\tau,$$

$$R = \frac{2^{1/2}E^{1/2}H\cos^{1/2}\theta}{\sin^{3/2}\theta}r,$$

$$D = \frac{EH}{\sin\theta}d, \tag{5.13}$$

$$W = \frac{F^{1/3}\sin^{5/6}\theta}{2^{1/2}E^{1/2}H^{1/3}\cos^{1/6}\theta}w,$$

$$g\frac{\rho_p - \rho_r}{\rho_r} = \frac{F^{2/3}\sin^{5/3}\theta}{2EH^{5/3}\cos^{1/3}\theta}f_p,$$

$$g\frac{\rho_e - \rho_r}{\rho_r} = \frac{F^{2/3}\sin^{5/3}\theta}{2EH^{5/3}\cos^{1/3}\theta}f_e$$

to give

$$\frac{d}{d\zeta}(rdw) = rw, \tag{5.14a}$$

$$\frac{d}{d\zeta}\left(rdw^2\right) = rd\left(f_p - f_e\right), \tag{5.14b}$$

$$\frac{d}{d\zeta}\left\{rdw\left(f_p - f_e\right)\right\} = -rdw\frac{df_e}{d\zeta}, \tag{5.14c}$$

$$w\frac{dr}{d\zeta} = \left\{\left(f_p - f_e\right)d\right\}^{1/2} \tag{5.14d}$$

and

$$\frac{\partial f_e}{\partial\tau} = rdw\frac{\partial f_e}{\partial\zeta}. \tag{5.14e}$$

A solution may be found to (5.14), similar to (5.8), for the quasi-steady state that is asymptotically approached at large times. As with the asymptotic solutions for the two-dimensional downslope and the axisymmetric plumes, the three-dimensional downslope plume in this state has steady W, D and $f_p - f_e$ at a given ζ while f_p and f_e increase at a fixed rate. The power series solution to three terms is given by

$$r = 0.894\zeta - 0.0474\zeta^2 - 0.0277\zeta^3 + \ldots, \quad (5.15a)$$

$$d = 0.6\zeta + 0.0671\zeta^2 + 0.0456\zeta^3 + \ldots, \quad (5.15b)$$

$$w = 1.12\zeta^{-1/3} - 0.274\zeta^{2/3} - 0.0672\zeta^{5/3} + \ldots, \quad (5.15c)$$

$$f_p - f_e = 1.67\zeta^{-5/3} - 1.36\zeta^{-2/3} - 0.193\zeta^{1/3} + \ldots \quad (5.15d)$$

and

$$f_e^* = f_e(\tau,\zeta) - f_e(\tau,1) = 1.56 - 2.5\zeta^{-2/3} + 0.931\zeta^{1/3} + 0.00878\zeta^{4/3} + \ldots. \quad (5.15e)$$

Plots for r, d, w, f_p^* $(=f_p(\zeta) - f_p(1))$ and f_e^* are given in figure 5.2.

5.4. Experiments

Experiments for observing the flow in two-dimensional downslope plumes behind the head have been carried out by Ellison and Turner (1959) and by Baines (1997). The aims of the experiments in the present study are to test the theoretical results of §5.3 for three-dimensional downslope plumes and to investigate the circulation patterns generated. All the experiments were conducted using tanks that were initially filled with fresh water. A smooth piece of perspex rising from the base to a side-wall served as a slope for the plume to descend. The buoyancy sources consisted of salt solutions (of density 1180 kg m^{-3} and 1090 kg m^{-3}) supplied by a peristaltic pump through a nozzle of diameter 2.5 mm. The nozzle, smaller than the one used in the experiments of chapter 4, was fixed on the slope and extended just below the water surface. The source volume fluxes were generally larger than in the earlier experiments in order to give large Reynolds numbers and low Richardson numbers near the nozzle.

Only ten experiments were conducted in the time available, all on 30° and 45° slopes. The parameters of the experiments are given in table 5.1. In the first six experiments, the plume width and depth were measured as each plume descended the slope into a homogenous environment. The perspex tank was 1.1 m long, 0.3 m wide and 0.24 m deep with the slope extending across the whole width at one end of the tank. The source solution was dyed to make the plume visible. A 10 mm × 10 mm grid on the slope and a 2 mm × 10 mm grid on the side of the tank enabled measurements of the

Experiment	Slope	Buoyancy Flux (10^{-6} m^4 s^{-3})	Source Re	Source Ri_0	Duration (min)
5.1	30°	6.64	1910	0.00652	n/a
5.2	30°	1.70	978	0.0125	n/a
5.3	30°	3.32	1910	0.00326	n/a
5.4	30°	3.32	978	0.025	n/a
5.5	45°	6.27	1810	0.00597	n/a
5.6	45°	2.81	810	0.0298	n/a
5.7	30°	3.58	1030	0.0223	20
5.8	45°	3.19	922	0.0229	25
5.9	45°	2.03	585	0.0569	25
5.10	30°	4.73	1360	0.0128	30

Table 5.1. The parameters of the experiments. The effective tank dimensions in all experiments were 1.1 m × 0.3 m × 0.2 m except experiment 5.10 (0.7 m × 0.7 m × 0.2 m and experiment 5.7 (1.1 m × 0.3 m × 0.15 m). Experiments 5.1 – 5.6 were stopped when the plume outflow layer had reached the far end of the tank (a few minutes).

plume dimensions by means of photographs taken from the top and side. Examples of these photographs are shown in figure 5.5.

The next three experiments (5.7 – 5.9) revealed the horizontal velocity patterns in the environment. These experiments were also conducted in the 1.1 m × 0.3 m × 0.24 m tank using inclines of 30° and 45° that extended across the width of the tank. The depths of water were small to prevent the plume from reaching the side-walls until it had reached the bottom of the tank. Dense plume water filled the bottom of one end of the tank and spread to the other end in an outflow layer that was approximately two dimensional. In each case, the plume was allowed to stratify the environment for 20 – 25 minutes and to establish a circulation pattern in the environment. The horizontal velocities were again

a)

b)

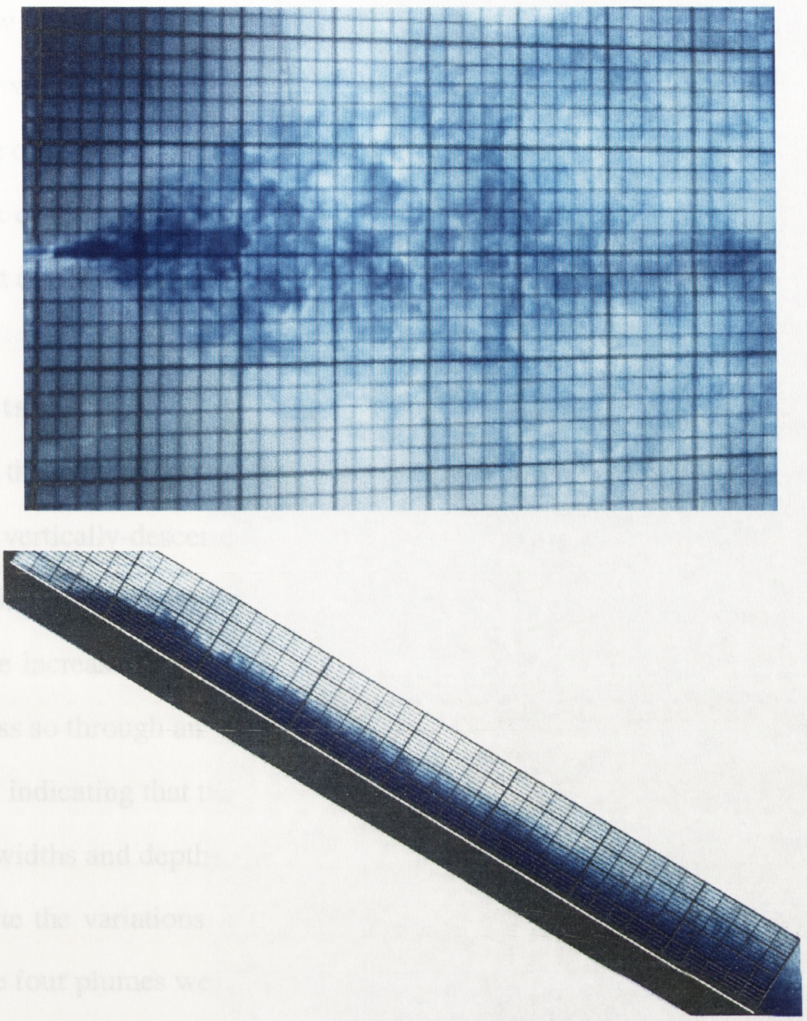

Figure 5.5. Photographs of a plume descending a 30° slope. (a) The view from the top (with 10 mm × 10 mm grid) and (b) from the side (with 10 mm × 2 mm grid).

measured from displacements of dye lines created by dropping potassium permanganate crystals into the tank.

A single experiment (5.10) was conducted to measure the "filling-box" stratification generated by the downslope plume. In this experiment, the effective dimensions of the tank were 0.7 m long, 0.7 m wide and 0.2 m deep. The 30° slope was formed by a plate 0.5 m long, 0.3 m wide and 0.01 m thick and so it did not extend across the full width of the tank. However, it was sufficiently wide so that the plume did not spill over its edges. It was placed in the middle of the tank (see figure 5.6) with the

region below open to the environment so that the horizontal cross-section of the environment was constant with depth. As the plume stratified the tank, conductivity profiles were obtained at three minute intervals using the traversing four-head probe and thermistor as described in chapter 4. Density profiles were collected up to 30 minutes from the start of the experiment.

5.5. Results

In all the experiments, the plume was turbulent immediately on leaving the nozzle. As with the vertically-descending axisymmetric plume, mixing between the downslope plume and the environment caused the plume to increase in volume and decrease in density. The increase in volume was accomplished mainly through a large increase in width and less so through an increase in depth. Successions of irregular eddies were seen at all depths, indicating that the Reynolds number was high throughout the plume.

The widths and depths of the plumes in experiments 5.1 – 5.4 are shown in figure 5.4a. Despite the variations in the source densities and volume fluxes, the widths and depths of the four plumes were very similar. This is consistent with the solutions (5.11) which show no dependency on the buoyancy flux F in the predictions for R and D. The width increased more or less linearly as expected by (5.11a), but the depth showed no

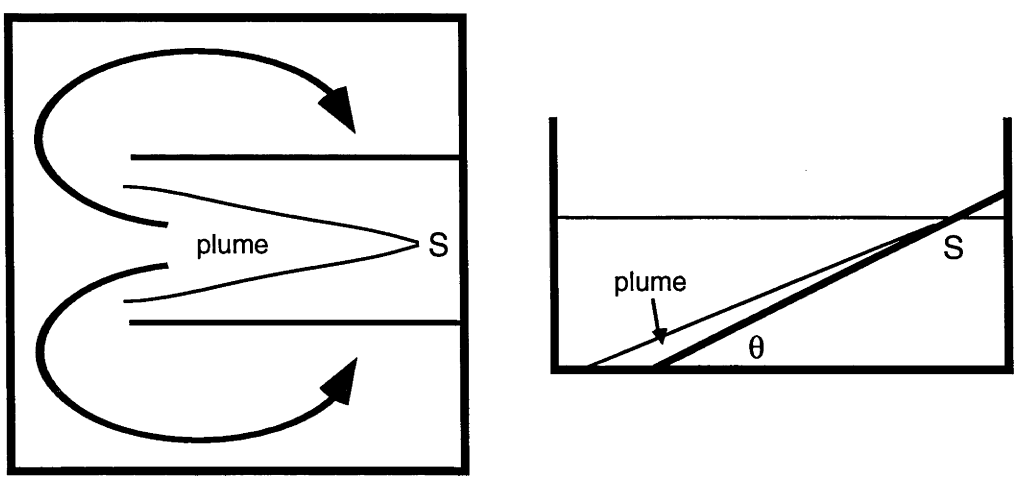

Figure 5.6. Top and side views of the tank in experiment 5.11 (not to scale) to measure the density profiles as the downslope plume stratified the environment. S indicates the location of the buoyancy source.

such linear trend as predicted by (5.11b). This is attributed to the method used in measuring the plume dimensions. For both the width and depth of the plume, the photographs gave the maximum dimension rather than the average dimension. In a downslope turbulent plume where the width was much larger than the depth and where many irregular eddies were present, the maximum depth as seen from the side at a given downslope distance s was larger than the average plume depth. In contrast the measurements of the plume width were more accurate because variations in plume width at a given s over the much smaller depth of the plume were generally small.

The measurements of the plume widths were used to calculate the entrainment coefficients for the three-dimensional downslope plume using (5.11a). For experiments 5.1 – 5.4 on the 30° slope, the entrainment coefficients were all similar and the average calculated as $E = 0.0748 \pm 0.0030$. This value was used in obtaining the plume properties of figure 5.4 and compares with $E \approx 0.033$ (see figure 5.1) found for the two-dimensional plume by Ellison and Turner (1959). Thus for this slope the entrainment coefficient for the three-dimensional downslope plume was smaller than that for the vertically-descending plume, but larger than for its two-dimensional equivalent. Experiments 5.5 and 5.6 showed that $E = 0.0944 \pm 0.0060$ for the 45° slope.

Experiments 5.7 – 5.9 examined the filling patterns of the tank. At the start, the three-dimensional downslope plume filled and stratified the box in a manner similar to the vertically-descending plume. As the source started, the plume water flowed to the bottom of the slope and an outflow layer formed in which dense plume water spread towards the opposite end of the tank. The top of this layer formed the first front, and as this moved up through the environment, a stratification was established throughout the tank.

While the stratification was developing, the circulation patterns in the tank were also similar to those for vertically-descending plumes. Above the bottom outflow layer, there were counterflowing layers with decreasing maximum velocities. However at large times, two circulation patterns appeared. In the first pattern, which was observed in experiment 5.8 and shown in figure 5.7, the plume outflow continued to spread at the bottom with several counterflowing shear layers lying above. In this experiment, the

velocity amplitudes of the layers decreased with distance from the bottom so that the horizontal velocity profile qualitatively resembled that of the vertically-descending case.

A different large-time circulation pattern was exhibited by experiments 5.7 and 5.9 after about 10 minutes from the start of the experiment. In this pattern, also shown in figure 5.7 for experiment 5.7, a thin boundary layer of very dense plume water formed along the incline and flowed to the bottom of the tank. This indicated that despite the turbulence and eddies seen in the plume, there were still large density differences within the depths of the plume. The very dense plume water fed a slow moving outflow which accounted for only a small fraction of the total plume volume flux. The majority of the plume (lying above the boundary layer) entered the environment as a broad mid-depth intrusion. This appears to be the "detrainment" noted by Baines (1997) in his experiments. Between the dense bottom layer and the broad mid-depth detraining layer was another layer which moved towards the plume. Above the detraining layer, there were several counterflowing layers of varying velocity scales.

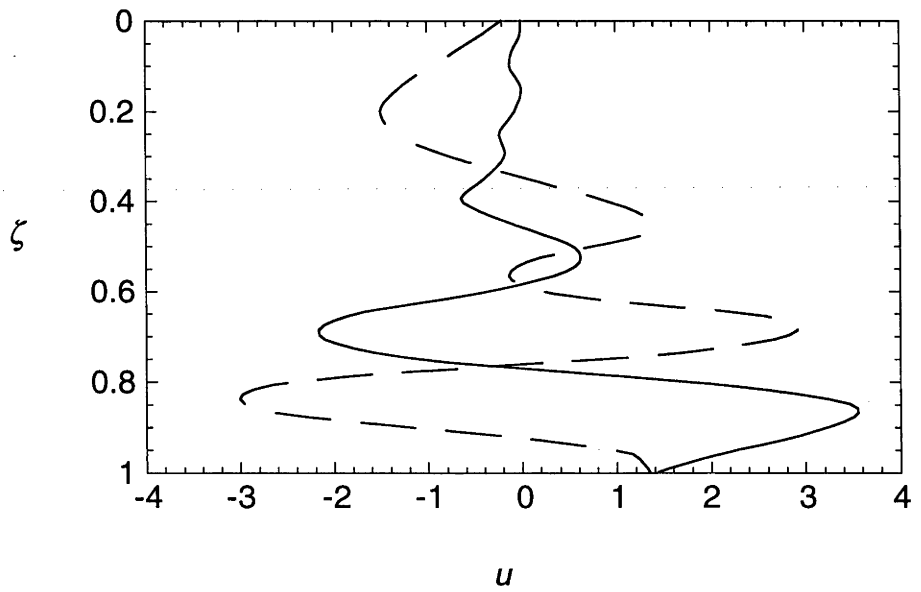

Figure 5.7. The dimensionless horizontal velocity u in the middle of the tank for experiment 5.7 at t = 20 min (—— ——) and for experiment 5.8 at t = 25 min (————————). The scale for the horizontal velocity is given by $U = EF^{1/3}H^{2/3}\cos^{1/3}\theta \sin^{-2/3}\theta B^{-1}u$, where the entrainment coefficients are taken as E = 0.0748 for experiment 5.7 and E = 0.0944 for experiment 5.8 (see §5.5).

The density profiles collected every three minutes during experiment 5.10 are plotted in figure 5.8a. At large times (> 18 minutes), the shape of the density (buoyancy) profiles over most of the tank (z < 0.13 m) resembled that of the "filling-box" profile created by a vertically-descending axisymmetric plume. However, in the region z > 0.13 m, there was a layer of very dense water at the bottom. The strong density gradients associated with this bottom layer are also seen in figure 5.8b where the observed 30 minute environmental buoyancy frequency is plotted along with the theoretically predicted profile for the same time. Over the duration of the experiment, the added volume of the input source solution had increased the total water depth by 1 cm (or 5% of the total). When the uplifting caused by the addition of input source solution is taken into account, the observed and predicted environment buoyancy profiles agree in the region above the dense bottom layer.

5.6 Discussion and Conclusion

5.6.1 The Current Results

The theoretical analysis in this chapter shows that, if a constant entrainment coefficient is assumed, then downslope plumes can be quantified in a similar way to vertically-descending plumes. The equations describing the properties of the two-dimensional downslope plume and the convection it generates in a "filling-box" environment reduce to those for a two-dimensional vertically-descending plume. In the three-dimensional case, a new streamtube model of the three-dimensional downslope plume has been formulated by likening the horizontal spreading of the downslope plume across the incline to the slumping of gravity currents on a horizontal plane. Previous streamtube models have been used to explain bottom slope currents in the oceans and incorporate the effects of rotation which turn the flow across the slope. The streamtube model in this chapter has ignored rotation to give a pure downslope flow, but has also extended the model to include the long-term changes to the "filling-box" environment.

Compared to the two-dimensional downslope plume, the three-dimensional downslope plume is more closely related to the vertically-descending axisymmetric plume

(a)

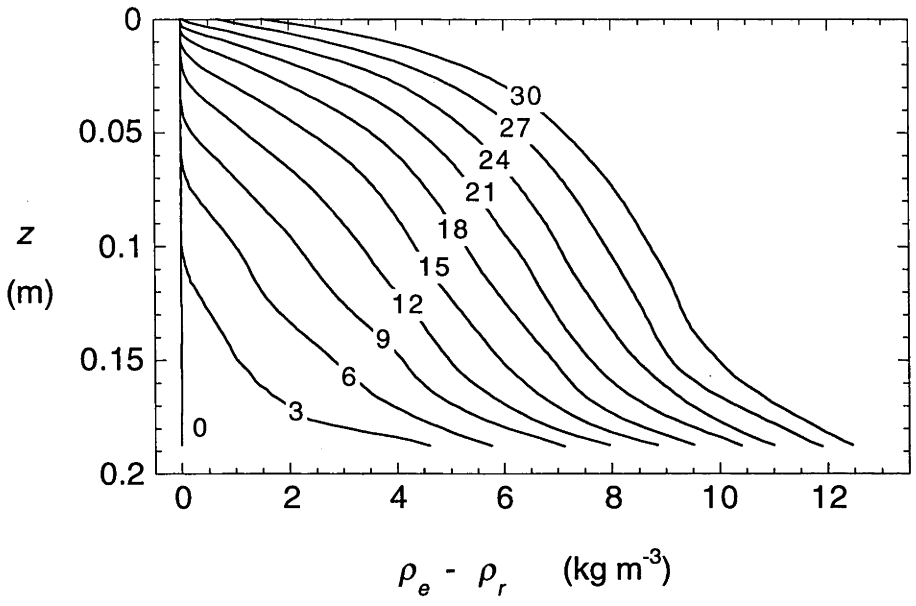

(b)

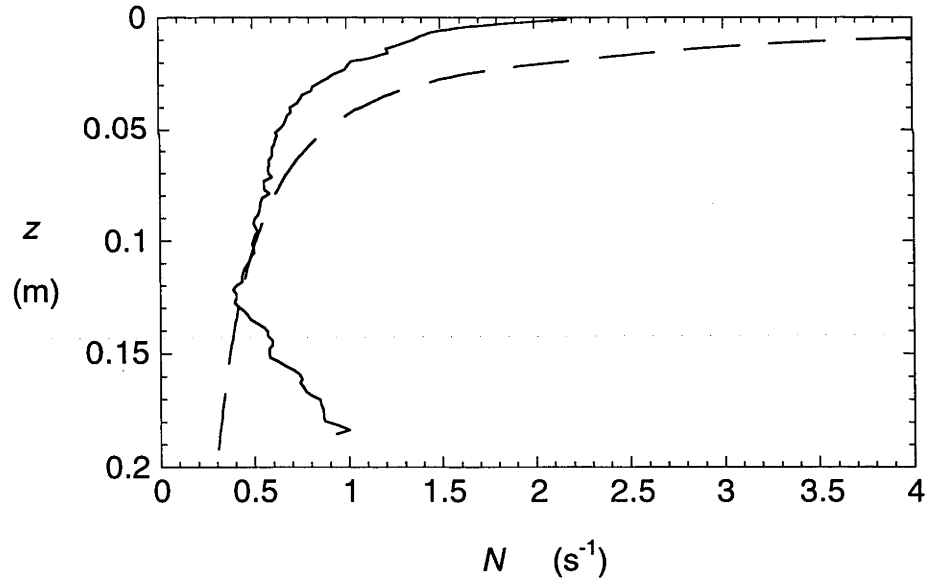

Figure 5.8. (a) The evolution of environment density profiles during experiment 5.10. The labels refer to time in minutes from the start of the experiment. At 30 min the familiar shape of the plume stratification can be recognised in the region $z < 0.13$ m (corresponding to $\zeta < 0.65$). (b) The observed (————) and predicted (— —) buoyancy frequency N at 30 min in experiment 5.10.

of chapters 2 and 4. The increasing depth and width of the three-dimensional downslope plume parallel the increasing radius of the vertical axisymmetric plume. The description of the downslope plume with a rectangular cross-section is expected to be valid for gentle and moderate slopes where the horizontal spreading of the plume is largely responsible for the increasing width. In these cases, the plume width is much larger than the plume depth and the entrainment terms in (5.9) only depend on the plume width. However, on steep slopes, where the plume behaves more like a vertical plume, the changes in both the width and depth of the plume are influenced more by an increase in the plume volume flux due to entrainment than by the slumping across the slope. In this situation, the rectangular shape of the plume is not expected to be valid and a semi-ellipsoidal shape may be more appropriate. Modifications to equations (5.9) and (5.10) will result from both the change in plume shape and, for steep slopes where the depth is comparable to the width, entrainment terms that depend on both the plume width and depth.

The entrainment coefficients for the three-dimensional downslope plume have been calculated for 30° and 45° slopes. In light of the large scatter in the entrainment coefficients measured for the two-dimensional downslope plume (figure 5.1; Ellison and Turner, 1959) and the small number of experiments in the present study, there is plenty of scope for the measurements of E to be further refined. Further experiments on other slope angles will also be required to determine the variation of E with θ and Ri_0.

Experiments 5.7 – 5.9 show that at least two circulation patterns may be generated by downslope plumes. A downslope plume generating a single broad outflow at the bottom of the tank formed shear layers similar to those produced by a vertically-descending plume. This pattern was observed in an experiment on a 45° slope with a relatively high source Reynolds number (Re = 922). In contrast, a downslope plume generating a small and very dense bottom outflow as well as a broad mid-depth intrusion (a "detraining" downslope current) formed more complex layers of counterflowing regions. This pattern was observed in an experiment also on a 45° slope, but with a lower source Reynolds number (Re = 585) and also on a 30° slope with a high source Reynolds number (Re = 1030). From these three experiments, it appears that both a highly

turbulent plume and steep slope are required for the plume to produce a single bottom outflow at all times and to generate a circulation pattern similar to that found in chapter 4.

The predictions of the density profiles using the assumption that the entrainment coefficient is constant are broadly consistent with the experimental data in the case of experiment 5.10 on a 30° slope (figure 5.8). The experimental density profiles for that case also showed that the plume gave rise to a very dense bottom outflow. Despite the high source Reynolds number (Re = 1360), it is speculated that thorough mixing of water in the plume did not occur as the plume flowed down the slope, resulting in a variation of density within the thickness of the plume. When such a plume flows into a homogenous environment, it continues to sink to the bottom because every part of the plume is still denser than the surroundings. However, when such a plume descends into a stratified environment, as it did in experiments 5.7, 5.9 and 5.10, it encounters progressively denser surroundings and as the less dense water in the plume reaches its neutral buoyancy level, detrainment occurs. The densest water, however, continues to descend to its own neutral buoyancy level or to the bottom. Thus at large times, when a pool of very dense water is collected at the bottom of a filling-box, the very dense bottom outflow separates from the broad detraining outflow at mid-depths.

5.6.2 Other Research

In flows on very gentle slopes or with low Reynolds number, the mid-depth spreading or detrainment of downslope plume water has been observed previously. Baines (1997) conducted a number of experiments on two-dimensional plumes descending a 6° slope into an uniformly stratified environment, including some with high Reynolds and low Richardson numbers ($Re > 1000$ and $Ri_0 < 0.1$) at the source. He identified three regions of flow type in each experiment: an initial adjustment region where the flow only entrained environmental water and adjusted to an approximately uniform depth; this led to the second region where there was both entrainment and detrainment from the plume; and a third region where the remaining plume water entered the environment at its neutral buoyancy level. The detrainment and spreading in the second

region in his experiments were similar to the mid-depth intrusions in some of the experiments described in this chapter. Mid depth intrusions were also seen in the dipolar experiment of Pierce and Rhines (1996). In their experiment there were two sources of opposite buoyancy fluxes with the denser plume descending along a 45° slope. The source leading to the sinking plume had low Reynolds and high Richardson numbers (Re ~ 10 and Ri_0 ~ 1). They observed that the sinking plume first entered the environment at the bottom but, as the experiment progressed, the plume outflow detached from the bottom and rose to form a mid-depth intrusion. There was also a strong density gradient at the bottom with gentler gradients found at mid-depths.

The experiments in this chapter provide some directions for further work. Direct measurements on the plume density structure will be able to confirm or dispel the speculation that incomplete mixing occurs in plumes on gentle slopes or with low Reynolds number. The results of such measurements will also lead to increased understanding into the mixing processes in downslope flows and provide clues on why detrainment occurs in some cases but is absent in others. A detailed study of the conditions which lead to detrainment may also allow more precise predictions of the horizontal velocity profile generated by downslope flows in filling-boxes.

Despite opening a range of problems that require more research, the analysis and experiments of this chapter show that in at least some cases, the "filling-box" convection by which a vertically-descending plume fills the environment can be extended to downslope plumes. In these cases, the shear layers and their associated horizontal velocities are similar to those seen in chapter 4 and the downslope plume may be approximated by a vertically-descending plume. It is also speculated that with thorough mixing induced in the plume many other occurrences of downslope plumes may also be approximated by a vertically-descending one.

Chapter 6

Multiple Plume Systems

6.1. Introduction

In this chapter, the "filling-box" model is extended to include multiple sources of buoyancy. In many applications, for example that of oceanic deep water production, there are a number of independent buoyancy sources. Each of the sources drives a (vertically-descending) plume that contributes to the stratification and circulation in the environment, but each plume is also modified by the environment. Although a study of the multiple plume case appeared in an unpublished paper by Peterson (personal communication), diffusion was induced in that study in order to balance the combined buoyancy fluxes of the plumes and the vertical advection in the environment and allow a true steady state to be reached. However, the large differences in the timescales for diffusion and advection in laboratory experiments rendered the model difficult to validate. In the present study, diffusion is not included and a very different solution is obtained. In §6.2, numerical and analytical solutions to the case of two buoyancy sources are presented. In §6.3 experiments designed to test the model and reveal circulation patterns are described. The results are presented in §6.4 and discussed in §6.5.

6.2. "Filling-Box" Model for Multiple Plumes

Each buoyancy source is assumed to produce a dense and turbulent plume that descends into a finite basin as described in chapter 2. If the basin initially contains homogenous water, each plume reaches the bottom and spreads out in an outflow layer. The least dense plume outflow overlies all the other outflows. The top of this outflow forms the "first front", a discontinuity in density distinguishing the overlying

homogenous water from water that has passed through one or more plumes. As each plume penetrates the first front and entrains water from below, each outflow becomes progressively denser. A vertical advection is generated in the environment which lifts the first front and establishes a stable stratification in the basin.

For large times, the results of Baines and Turner (1969) indicate that only the plume from the source with the largest buoyancy flux will reach the bottom. In general, plumes from sources with smaller buoyancy fluxes descend only to an intermediate depth and their outflows form mid-depth intrusions into the stratification. Figure 6.1 gives a schematic diagram of the general two plume situation.

6.2.1 Theory

Buoyancy-driven convection is assumed to be the dominant transport mechanism in the plumes while passive advection and entrainment-driven inflow towards the plumes are assumed to be the only processes in the environment that influence the stratification. Motions due to internal gravity waves and baroclinic modes (chapter 4) were found to greatly influence the horizontal velocity field, but have little or no consequence on the stratification. It is assumed that they have no effect on entrainment into the plume and hence no effect on the plume properties. It is also assumed that each of the n plumes is

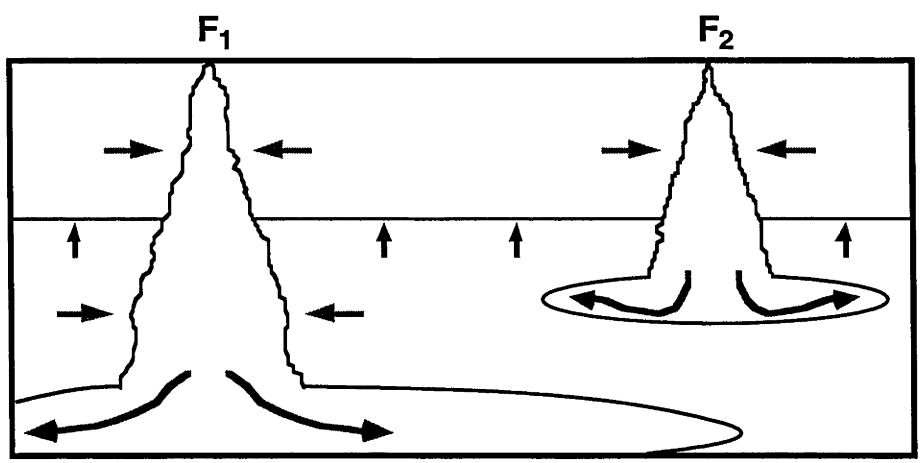

Figure 6.1. A schematic diagram of the two plume filling-box. The strong plume outflow (left) spreads into the environment at the bottom while the weak plume outflow (right) spreads at an intermediate depth.

well separated from one another and from the side walls so that each is able to descend unimpeded. In the case of a single plume Manins (1979) observed that the aspect ratio (width/depth) of a basin has to be at least 1.2 to prevent an inertial overturning that mixes the environment water from top to bottom. Thus for n plumes and a basin of height H, a lower bound to the cross-sectional area of a rectangular basin is $1.44nH^2$.

For each plume, the equations representing the conservation of volume, momentum and mass deficiency are described by (2.1). The equation representing conservation of volume in the environment is altered to take into account the vertical advection generated by all the plumes. Thus (2.3a) is replaced by

$$AV = -\sum_i \pi R_i^2 W_i, \tag{6.1}$$

where the subscript i refers to plume i. However, (2.3b) representing conservation of density in the environment remains unchanged.

The spreading depth z_i^{sp} for plume i is defined as either its neutral buoyancy level or the bottom if that is reached first. These two conditions correspond to

$$\rho_{ip}(z,t) = \rho_e(z,t) \text{ at } z = z_i^{sp}(t) \tag{6.2a}$$

and

$$z_i^{sp}(t) = H \tag{6.2b}$$

respectively (Killworth and Turner, 1982). The definition of the spreading depth as the neutral buoyancy level is the simplest form for analysis because the plume can be assumed to immediately spread into environment waters of the same density. In reality, the neutral buoyancy level is an underestimation of the actual spreading depth because the downward momentum of the plume at the neutral buoyancy level carries it deeper to the neutral momentum level (where $w_i = 0$). Mixing with the environment between the neutral buoyancy level and the neutral momentum level increases the density of the plume so that when the outflow spreads, its density is somewhere between the environment densities of the neutral buoyancy and neutral momentum levels. Consequently, the outflow settles at some depth between the two neutral levels.

The non-dimensional scalings (2.4) are also valid for the multiple plume case except that the buoyancy flux F is replaced by $F = \sum_i F_i = \sum_i \pi R_i^2 W_i g(\rho_{ip} - \rho_e)/\rho_r$, the sum of all the buoyancy fluxes. With these scalings and the Boussinesq approximation, the equations for each plume are

$$\frac{d}{d\zeta}\left(r_i^2 w_i\right) = r_i w_i, \tag{6.3a}$$

$$\frac{d}{d\zeta}\left(r_i^2 w_i^2\right) = r_i^2\left(f_{ip} - f_e\right) \tag{6.3b}$$

and

$$\frac{d}{d\zeta}\left(r_i^2 w_i f_{ip}\right) = r_i w_i f_e, \tag{6.3c}$$

while the equations for the environment are

$$v = -\sum_i r_i^2 w_i \tag{6.4a}$$

and

$$\frac{df_e}{d\tau} = -v\frac{df_e}{d\zeta}. \tag{6.4b}$$

As before, an alternative form of (6.3c) is obtained by combining with (6.3a) to give

$$\frac{d}{d\zeta}\left\{r_i^2 w_i\left(f_{ip} - f_e\right)\right\} = -r_i^2 w_i \frac{df_e}{d\zeta}. \tag{6.3c'}$$

The conditions (6.2) for spreading at the neutral buoyancy level and the bottom are now

$$f_{ip}(\zeta,\tau) = f_e(\zeta,\tau) \text{ at } \zeta = \zeta_i^{sp}(\tau) \tag{6.5a}$$

and

$$\zeta_i^{sp}(\tau) = 1. \tag{6.5b}$$

The scalings (2.4) ensure that the dimensionless sum of the buoyancy fluxes of all the sources is one unit. The convention used is that plumes are ordered by the strength of the sources so that $F_i \geq F_{i+1}$. In the case of two plumes, the split in buoyancy flux between the two sources is indicated by $\Phi = F_2/F$, the ratio of the flux of the weak source to the total buoyancy flux. Thus, for instance, $\Phi = 0.1$ refers to the two plume case where $F_1 = 0.9F$ and $F_2 = 0.1F$.

6.2.2 Solutions

With n buoyancy sources, the equations to be solved consist of n sets of (6.3) and (6.5) for the n plumes and the single set (6.4) for the environment. This system of equations is too complicated to be solved analytically except for the cases mentioned in chapter 2 for a single plume. Instead, a finite-difference scheme based on that used by Killworth and Turner (1982) is used. Given an environmental buoyancy profile f_e each of the n sets of (6.3) is solved separately using a fourth-order Runge-Kutta method. The buoyancy flux of each source is specified at the first gridpoint below the source's level where the integration is started using the analytic solution (2.7) for a plume descending in a homogenous environment. The use of (2.7) very close to the source is valid because the environment between the source and the first front, which reaches $\zeta = 0$ only at $\tau = \infty$, can be considered homogenous. The Runge-Kutta integration is performed to obtain r_i, w_i and f_{ip} from the second gridpoint until either of the conditions in (6.5) is met. If the plume does not reach the bottom, the spreading depth is taken as the first gridpoint below the neutral buoyancy level. The spreading into the environment is assumed to be an injection of volume into the spreading gridpoint. Once (6.3) has been solved, the system is stepped forward in time using (6.4) by advecting f_e to give the new buoyancy profile for the next timestep. The new profile is then used to calculate the plume properties and the cycle repeats.

I have obtained results for the case of two buoyancy sources for a selected set of Φ. The solutions for $\Phi = 0.1$, 0.25 and 0.5 are given in figure 6.2 at time $\tau = 10$, when the first front is located close to $\zeta = 0.1$. At this time the solution is approaching the large time steady state similar to the asymptotic solution (2.10), (2.11) and (2.12) for a single plume. Compared with the weak plume, the vertical velocity and buoyancy of the strong plume are larger at a given depth, with the difference between the two plumes increasing for smaller Φ. Figure 6.2 also shows that the weak plume has a marginally larger radius than the strong plume, particularly as its descent slows near the neutral buoyancy level; however the radii of the strong and weak plumes remain similar for all Φ. Furthermore, the stratification produced by two buoyancy sources is very similar to that produced by a

single source having the combined buoyancy flux. Figure 6.3 gives a plot of the neutral buoyancy level of the weaker plume as a function of Φ. For small Φ, the neutral buoyancy level of the weak plume is located near the top. As the weak source becomes stronger (larger Φ), the neutral buoyancy level becomes lower and reaches the bottom at the limiting case of two equal sources ($\Phi = 0.5$). As with the single plume case, the environment density at a given depth increases linearly at large times. This indicates that at large times the sources supply buoyancy uniformly to the whole tank and so the shape of the buoyancy or density profile approaches a steady state. The steady state buoyancy profile has a similar shape for all Φ.

(a)

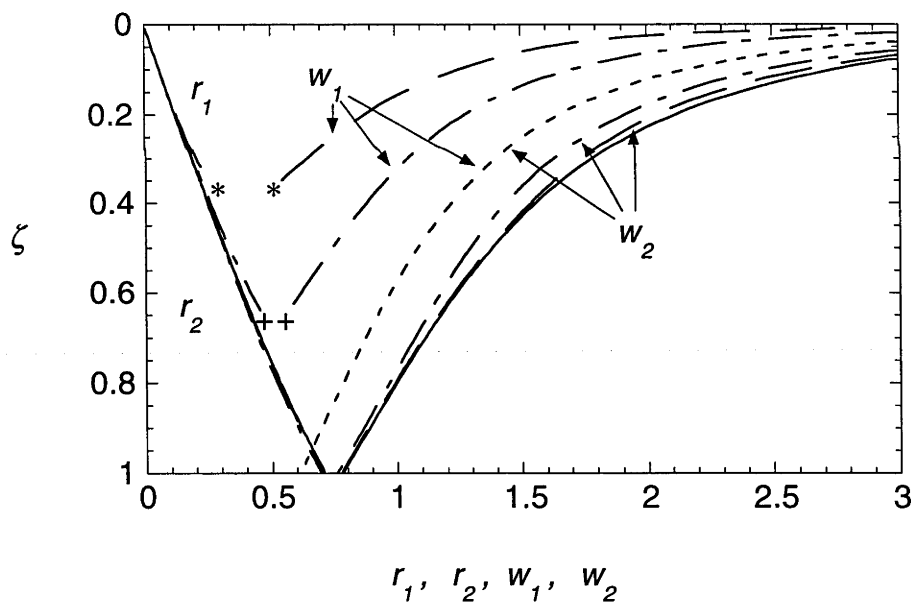

Figure 6.2 (on this page and the next). The numerically computed solutions to (6.3), (6.4) and (6.5) for three ratios of buoyancy fluxes at $\tau = 10$: —— —— $\Phi = 0.1$, - — - — $\Phi = 0.25$ and - - - - - - - - $\Phi = 0.5$. The control case of a single plume (————) is also plotted. (a) Plume radii r_1 and r_2, and vertical velocities w_1 and w_2. (b) Plume buoyancies f_{1p} and f_{2p} (c) Environment buoyancy f_e. In (a) and (b) the symbols * and + refer to the neutral buoyancy levels of the weak plume in the $\Phi = 0.1$ and $\Phi = 0.25$ cases respectively. In the $\Phi = 0.5$ case, each pair of plots for r_1 and r_2, w_1 and w_2 as well as f_{1p} and f_{2p} coincide.

(b)

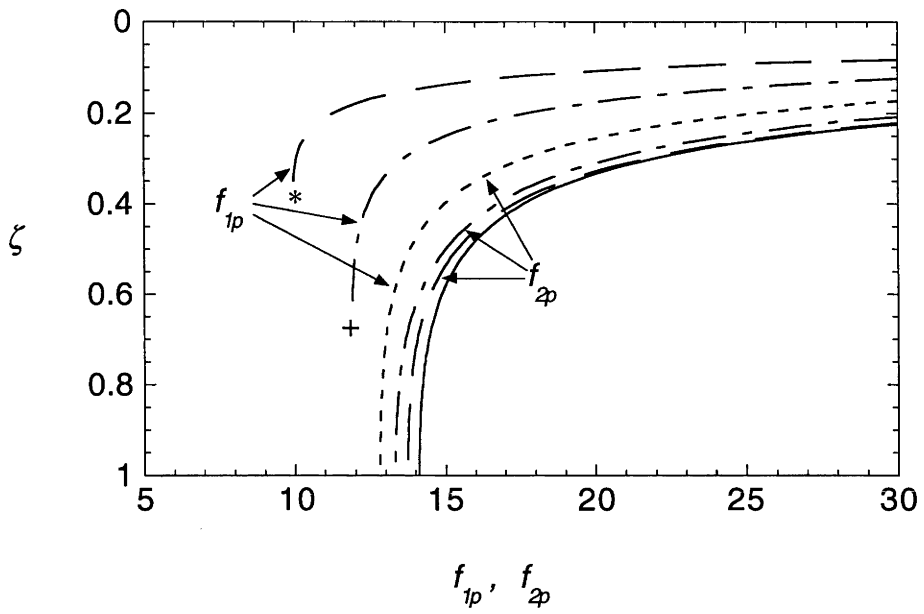

(c)

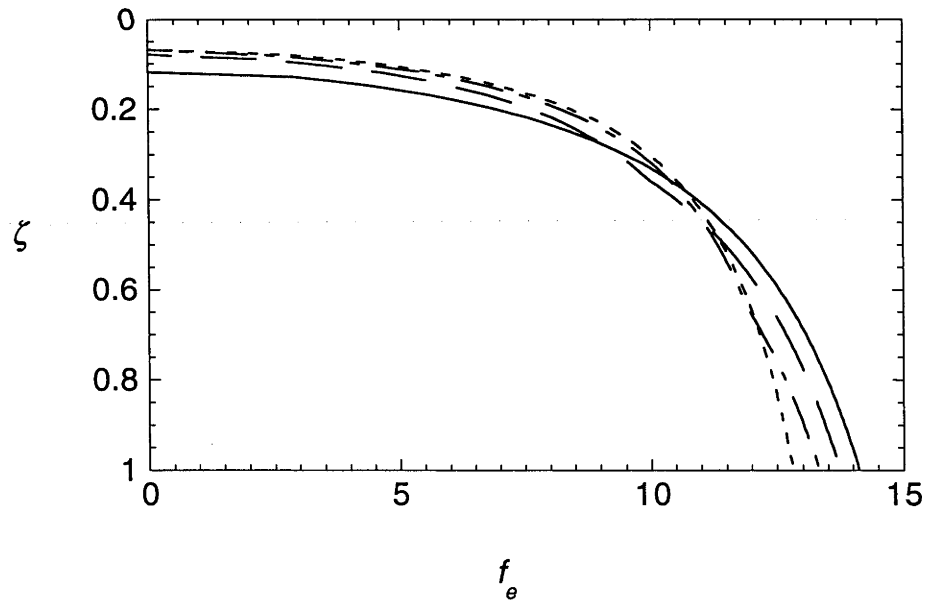

Figure 6.2. See previous page for caption.

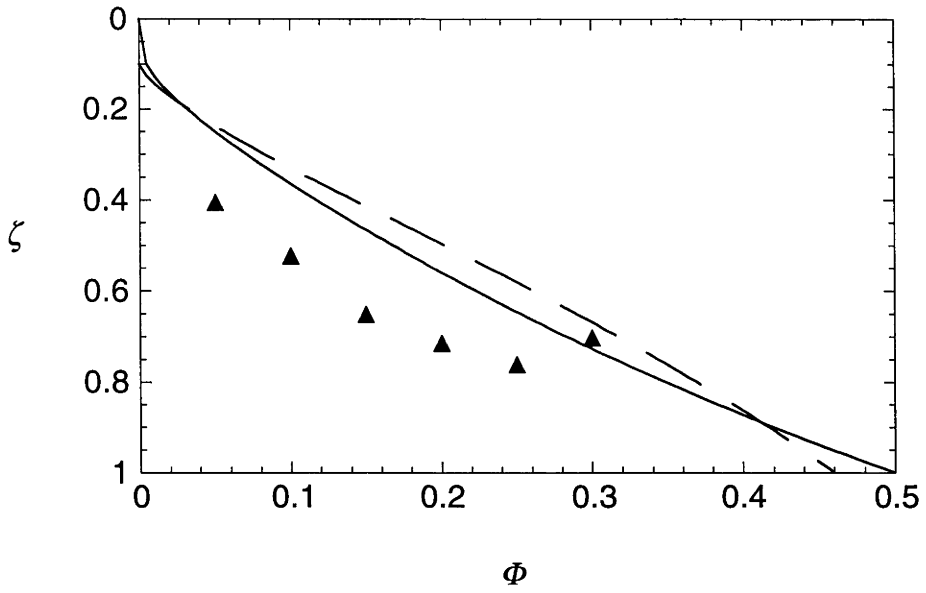

Figure 6.3. The neutral buoyancy level of the weak plume calculated numerically (————) and from the approximate analytic solution (6.8) (—— ——). Both neutral buoyancy levels are taken when the first front reaches $\zeta_f = 0.1$ and are plotted as functions of Φ. Also plotted are the depths of the lower extent of the weak plume intrusion (▲) at the end of each tank A experiment.

6.2.3 Approximate Analytic Solution

In the two plume case, the weak plume has a slightly larger radius but much lower vertical velocity than the strong plume (figure 6.2) and thus provides a smaller contribution to the ventilation of the filling box. An approximate spreading level of the weak plume at large times may be found analytically by assuming that the strong plume is solely responsible for establishing the stratification and can thus be determined by (2.12). This stratification can then be applied to determine the weak plume properties. However, when using the dimensionless equations and solutions to describe the strong and weak plumes separately, it must be noted that the non-dimensional scalings are different in each case. Thus to apply the stratification produced by the strong plume to equations (6.3) and (6.4) for the weak plume, it is necessary to rescale the solution obtained for the strong plume to that appropriate for the weak plume. The dimensional large-time stratification produced by the strong plume is given by (2.12) and (2.4) as

$$\frac{2^{4/3}E^{4/3}\pi^{2/3}H^{5/3}}{F_1^{2/3}}g\frac{\rho_e-\rho_r}{\rho_r}$$

$$=-\left(\frac{z}{H}\right)^{-2/3}\left\{3.27-0.837\left(\frac{z}{H}\right)-0.0623\left(\frac{z}{H}\right)^2\right\}+c \qquad (6.6)$$

and is valid below the first front ($z \geq z_f$). The constant c can be determined by setting the left hand side to zero at $z = z_f$. Rescaling (6.6) using the parameters of the weak plume gives the new dimensionless environmental buoyancy profile as

$$\begin{aligned} f_e &= -\frac{F_1^{2/3}}{F_2^{2/3}}\left\{\zeta^{-2/3}\left(3.27-0.837\zeta-0.0623\zeta^2\right)-c\right\}, \qquad \zeta \geq \zeta_f \\ f_e &= 0, \qquad \zeta \leq \zeta_f. \end{aligned} \qquad (6.7)$$

Equations (6.3a), (6.3b) and (6.3c′) can now be solved using (6.7). The right hand side of (6.3c′) can be approximated by assuming that the dimensionless volume transport, $r_i^2 w_i$, is given by the asymptotic solution (2.11a) for the weak plume descending in its own stratification rather than the strong plume's stratification. (The dimensionless volume flux of a plume varies with distance from the source, but is not greatly changed when the plume travels through stratifications of different strengths.) With this assumption, equation (6.3c′) becomes

$$\frac{d}{d\zeta}\left\{r_2^2 w_2\left(f_{2p}-f_e\right)\right\} = -r_2^2 w_2 \frac{\partial f_e}{\partial \zeta} \approx -\frac{F_1^{2/3}}{F_2^{2/3}}$$

for $\zeta \geq \zeta_f$ and, noting that $r_2^2 w_2(f_{2p} - f_e) = 1$ at $\zeta = \zeta_f$ (see Morton et al., 1956), this gives

$$r_2^2 w_2\left(f_{2p}-f_e\right) = -\frac{F_1^{2/3}}{F_2^{2/3}}\left(\zeta-\zeta_f\right)+1.$$

The neutral buoyancy level, ζ_2^{sp}, occurs when $f_{2p} = f_e$ and so

$$\zeta_2^{sp} = \left(\frac{F_2}{F_1}\right)^{2/3} + \zeta_f. \qquad (6.8)$$

Because $\zeta_f \to 0$ at very large times $\zeta_2^{sp} \to (F_2/F_1)^{2/3}$. However, in practical situations where the first front has not reached the top, it is useful to keep the neutral buoyancy level as defined by (6.8). A plot of (6.8) against Φ when $\zeta_f = 0.1$ is given in figure 6.3.

The result may also be generalised to n sources. If the ith source has buoyancy flux F_i and the first source is the strongest source, then the large time spreading depth of the ith plume is estimated as

$$\zeta_i^{sp} = \left(\frac{F_i}{F_1}\right)^{2/3} + \zeta_f .$$

6.3. Experiments

The experiments consisted of releasing two dense salt solutions at a steady rate through two small nozzles, each as in the chapter 4 experiments. Differences in buoyancy fluxes between the two sources were achieved by using salt solutions of different densities ranging from 1010 to 1190 kg m^{-3}. Two tanks were used. The first (tank A) was 0.7 m long, 0.7 m wide and 0.5 m deep while the second (tank B) was 1.1 m long, 0.3 m wide and 0.24 m deep. In both tanks, experiments were conducted with the nozzles placed on the centre line running along the length of the tank and 0.15 m from each end. An additional set of experiments in tank B was conducted with the strong source's nozzle placed at 0.15 m from one end as in the other experiments and the weak source's nozzle at 0.4 m from the opposite end. The effective water depths were approximately 0.3 m in tank A and 0.23 m in tank B. For the durations of the experiments in all cases, the total volumes of salt water added were insignificant compared to the volumes in the tank.

The plumes were viewed by the shadowgraph method in which a sheet of translucent paper was placed in front of the tank with a parallel light source from behind. Further enhancements were made by dyeing one or both of the source solutions. However, the shadowgraph view was not an accurate method to measure the positions of the fronts and intrusions because refraction of the light as it passed through the tank caused errors (up to 1 cm) in vertical position on the screen. A more accurate method was possible if the paper was used as a translucent diffusing screen on the back of the tank, with dye revealing the location of water which had passed through the plume.

As before, measurements of the vertical density profiles through the tank were collected using a traversing conductivity probe and a thermistor and then converted to density using the equations of Ruddick and Shirtcliffe (1979). The density profiles were taken in the tank approximately equidistant from the two sources.

All the experiments were started in homogenous tanks to study both the evolution and large time behaviour of the systems. The first six experiments were carried out in tank A where $F \approx 8.97 \times 10^{-7}$ m^4 s^{-3} and Φ ranged from 0.05 to 0.3. In these experiments, the salt solution of the weak source was dyed at all times. This procedure enabled the measurement of both the first front (uppermost dye in environment) and the bottom of the weak plume outflow into the stratification (bottom of deeply-dyed water). The depth of the weak plume outflow was taken at a distance of 0.15 m from the plume axis where the outflow appeared to level out soon after rising from the neutral momentum level. Originally this was to minimise the effects of advection which acted to lift the whole environment, but it was later found that this was also important in minimising the effects of the horizontal motions in the basin on the apparent spreading level (see §6.5.1). In two of the experiments ($\Phi = 0.1$ and 0.25), the sources were also stopped every three minutes; the tank was then rested for ten minutes to allow all motions to decay and a density profile taken with the water at rest before the sources were restarted. All six experiments ran for 30 minutes, the time required for the depth of the weak plume outflow to approach the final steady-state depth.

When these six experiments were carried out, the significance of shear layers driven by turbulent plumes (chapter 4) was not known. As it became apparent that the horizontal motions induced by the strong plume outflow would affect the spreading of the weak plume into the environment, the six experiments were each repeated twice in the longer and narrower tank B as described earlier, but with $F \approx 7.55 \times 10^{-7}$ m^4 s^{-3}. In each of the twelve experiments the sources were allowed to stratify the environment for 90 minutes to the steady state and to set up the horizontal motions for this stratification. Both source solutions were then dyed with different colours and the experiment videotaped to reveal the outflow positions and thicknesses, and to examine the circulation and its implications for water transport in the basin. Horizontal velocities were once again measured from displacements of a dissolved potassium permanganate dye line. Figure 6.4 is a photograph of a typical experiment in tank B.

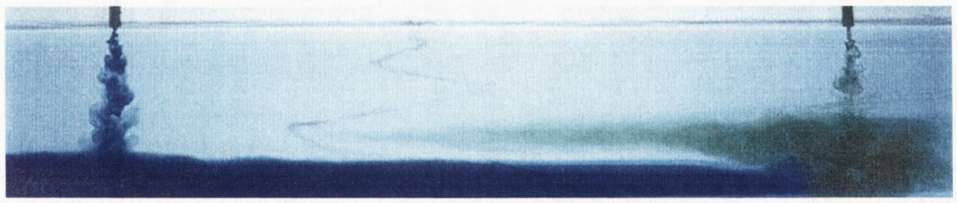

Figure 6.4. A photograph of an experiment in tank B where the two sources were placed at opposite ends of the tank and $\Phi = 0.25$. The strong plume (left) spread at the bottom while the weak plume (right) spread at an intermediate depth. Blue and green dyes were introduced into the strong and weak source solutions respectively shortly before this photograph was taken. In this experiment, the movement of an initially vertical dye line produced by dropping potassium permangante crystals into the tank also revealed shear layers.

6.4. Results

When the sources were started simultaneously, both plumes initially descended to the bottom of the tank. As the outflows spread along the bottom and collided, the weak plume outflow rose over the strong plume outflow. The strong plume continued to spread at the bottom of the tank as more plume water entered the environment, but the weak plume outflow lifted slowly until it eventually settled at a depth that depended on the ratio of the two buoyancy fluxes. If $\Phi > 0.25$, the weak plume remained sufficiently dense to reach the bottom, even though its outflow spread at an intermediate depth. If $\Phi < 0.25$, the weak plume was eventually not dense enough to reach the bottom; it overshot its neutral buoyancy level and sank to its neutral momentum level before rising a small distance and spreading at its final depth. At the same time the upwelling in the environment filled the basin with water from both outflows to give the familiar plume stratification. Thus at large times the lower regions of the tank were filled with water from the strong plume while the intermediate depths were filled with both water from the weak plume and water upwelled from the strong plume. In all cases and for all Φ, the time required for the first front to pass through 90% of the tank was approximately 50 minutes. The times taken for the spreading level of the weak plume to approach its final asymptotic level were approximately half the filling times. From chapter 2, the entrainment constant found was 0.129 ± 0.004.

The first six experiments using tank A provided data on the evolution of the system from the start of the experiment to the steady state. In figure 6.5 the observed and the numerically predicted positions of the first front and the bottom of the weak plume outflow are given for $\Phi = 0.3$, 0.25, 0.2, 0.15, 0.1 and 0.05. The positions of the weak plume outflow at the end of each experiment are also plotted in figure 6.3. In each case, the plots for the position of the first front show extremely good agreement between the experiments and theory. As expected, the bottom of the weak plume outflow was consistently lower than the neutral buoyancy level at large times due to an excess of momentum in the weak plume as it passed the neutral buoyancy level, but there was close agreement for $\Phi = 0.3$.

Several environmental buoyancy profiles from the $\Phi = 0.1$ experiment are given in figure 6.6 along with the corresponding theoretical profiles. For small times the theory predicted sharp density jumps at the first front and between the outflows of the two plumes. A continuous density profile was measured instead because the plume outflow was not uniformly dense as assumed in the top-hat plume profile and because sharp density jumps were most likely eroded by mixing between the outflows and the surrounding water. At large times neither effect altered the density profile because the plume outflows were spreading in stratified environments of densities similar to themselves and thus the observed density profile is very similar to the theoretical profile.

The experiments in tank B provided data on horizontal velocities and positions of the outflow intrusion layers. Figure 6.7 gives the horizontal velocities at the center of the basin for $\Phi = 0.25$ and 0.1 where the sources were placed at opposite ends of the tank. Also plotted are the horizontal velocities from the single plume case in the same tank (figure 4.3a). (For comparison with the single plume case, the horizontal velocity u is non-dimensionalised as though the circulation was forced by the outflow of the strong plume only. Thus the horizontal velocity u at the centre of the tank is related to the observed velocity U by

$$U = 2^{1/3}\pi^{2/3}E^{4/3}F_1^{1/3}H^{2/3}B^{-1}u,$$

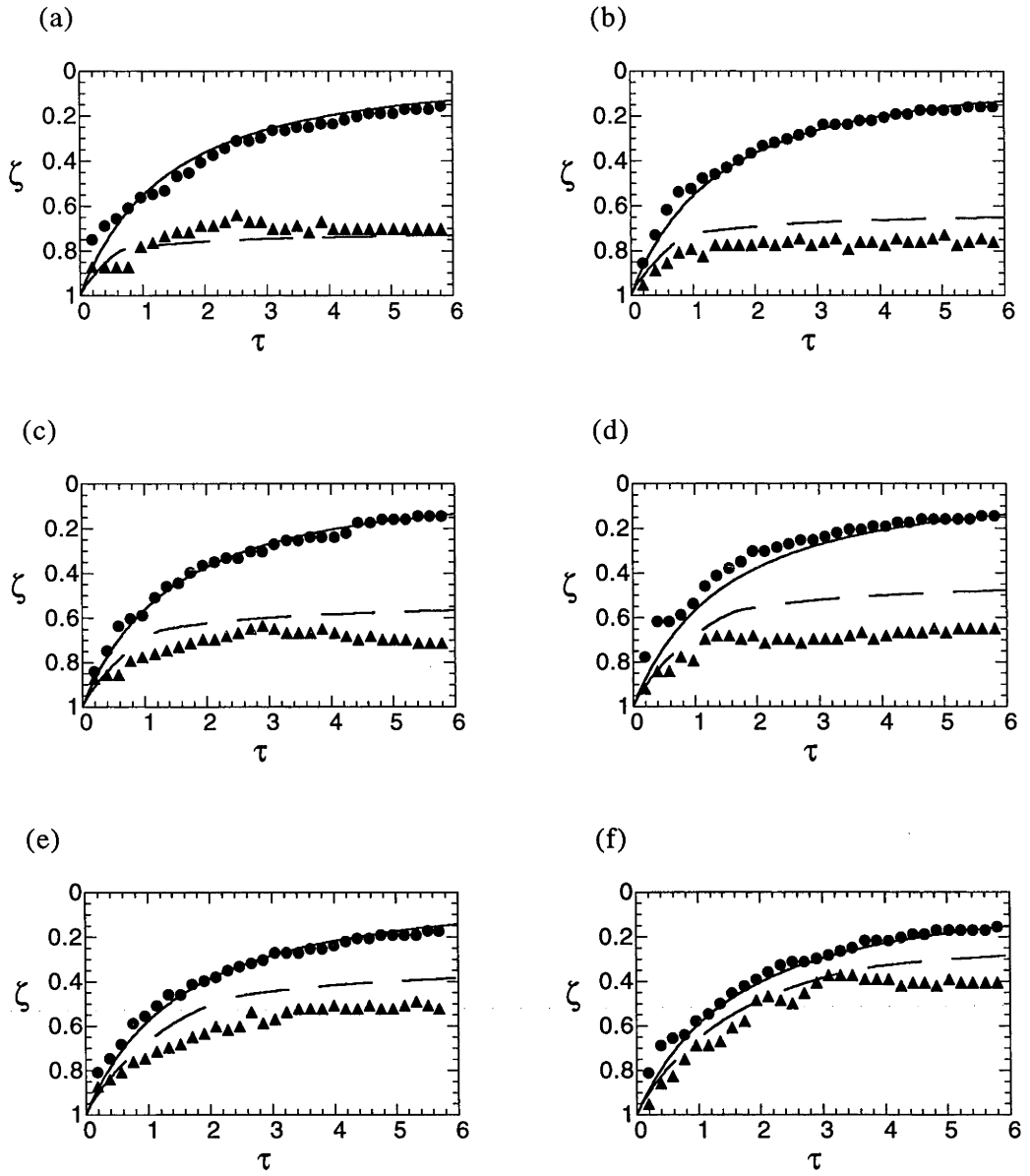

Figure 6.5. The positions of the first front (●) and the lower extent of the weak plume intrusion (▲) into the environment from tank A experiments. (a) $\Phi = 0.3$, (b) $\Phi = 0.25$, (c) $\Phi = 0.2$, (d) $\Phi = 0.15$, (e) $\Phi = 0.1$ and (f) $\Phi = 0.05$. Also shown are the theoretical predictions (———— for first front positions and —— —— for neutral buoyancy levels).

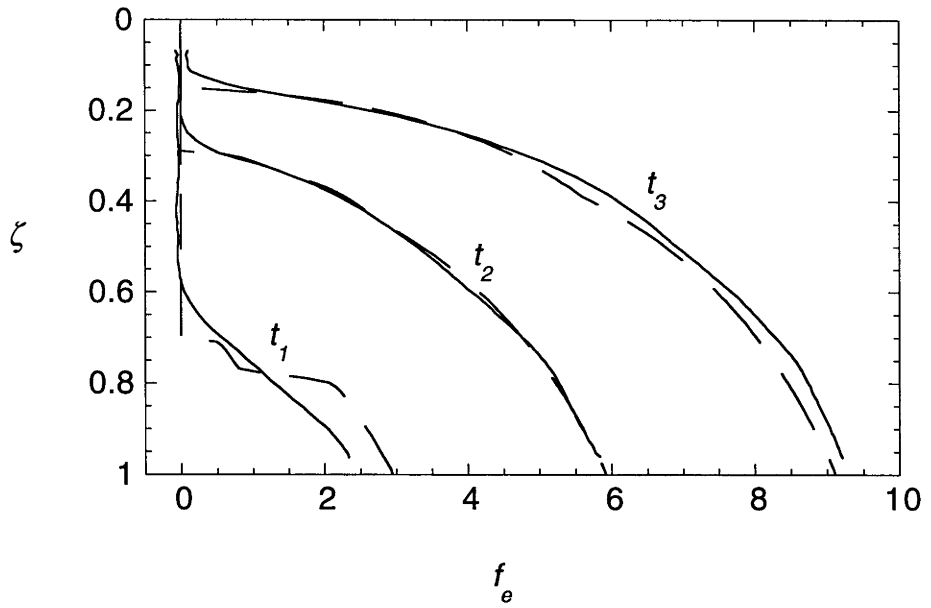

Figure 6.6. The environment buoyancy profiles f_e (———— for experiment and —— —— for theory) for $\Phi = 0.1$ at times $t_1 = 3$ min ($\tau = 0.6$), $t_2 = 15$ min ($\tau = 2.9$) and $t_3 = 30$ min ($\tau = 5.7$).

where B is the width of the tank; see (4.2).) The horizontal velocities for the two plume cases show a number of shear layers qualitatively similar to that of the single plume case. However, the bottom layer is thicker in the single plume experiment.

From the shape of the horizontal velocity profile, it can be deduced that the outflow of the strong plume was the main force behind the formation of the shear layers. The weak plume outflow moved in the direction of the shear layer it intruded in, as though it was moving passively in the background circulation. Figure 6.8a is a photograph showing the dyed outflow of the weak plume ($\Phi = 0.1$) spreading at approximately $\zeta = 0.4$, a depth where the direction of horizontal motion in the background shear layers was away from the strong plume and towards the weak plume. The outflow was unable to spread against the backgound motion and as it was also constrained by the end-wall, it languished near the weak plume. Only after the outflow water had been advected up into a shear layer which flowed in the opposite direction did the intrusion begin to spread across the tank. When the weak source was instead placed near the center of the tank (figure 6.8b), the outflow from the weak plume was not

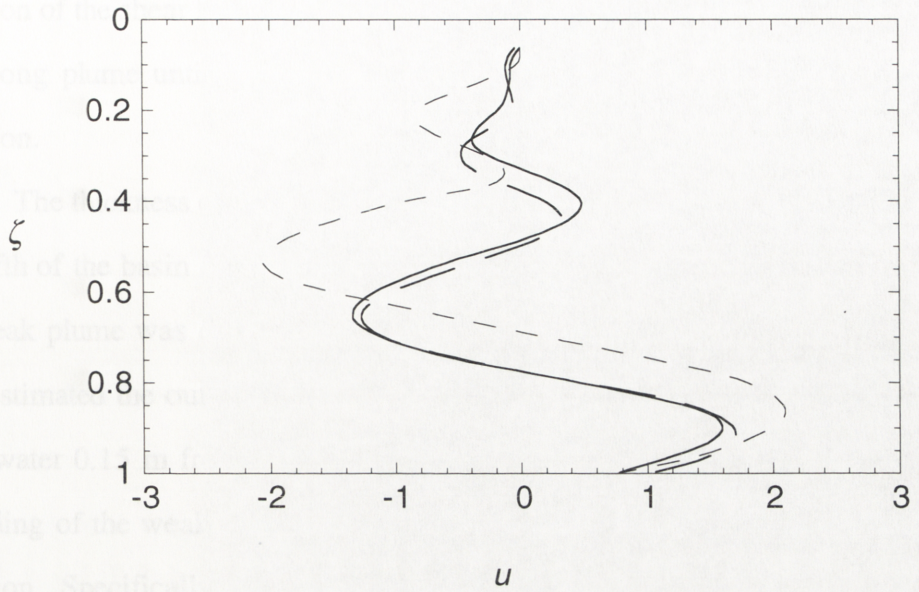

Figure 6.7. Dimensionless horizontal velocities at the centre of the basin in tank B experiments where the sources were at opposite ends of the tank: ———— for $\Phi = 0.25$ and — — for $\Phi = 0.1$. The dimensionless horizontal velocities for the case of a single plume in this tank (experiment 4.10, figure 4.3a) are also given by — — — — .

(a)

(b)

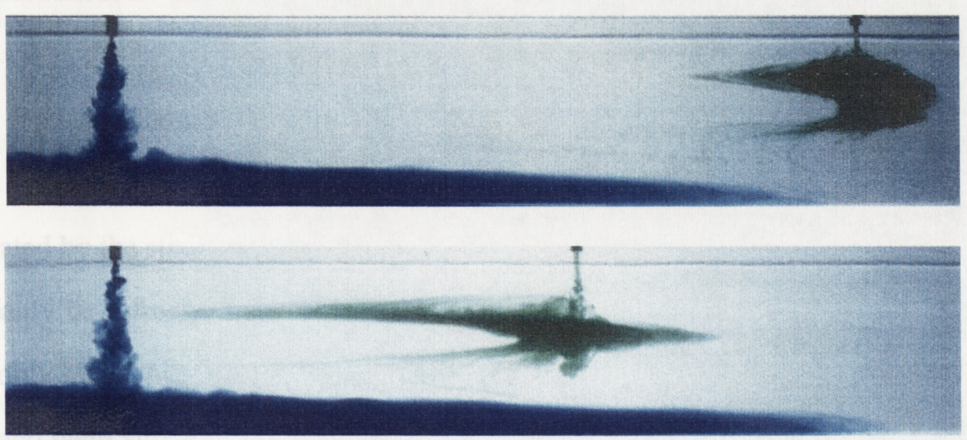

Figure 6.8. Photographs of two experiments which show that the weak plume outflow (right) is strongly influenced by the shear layers driven primarily by the strong plume outflow (left). Both (a) and (b) show $\Phi = 0.1$ experiments, the two differing only in the position of the weak source. As with figure 6.4, blue and green dyes were introduced in the strong and weak source solutions respectively shortly before these photographs were taken.

constrained by an end-wall and spread away from both plumes, following the prevailing direction of the shear layers at that depth. Again, the outflow water did not flow towards the strong plume until it had upwelled to a level where the shear layer flowed in that direction.

The thickness of the strong plume outflow at the bottom of the basin was a quarter to a fifth of the basin depth for all the experiments. Measuring the outflow thickness of the weak plume was difficult because the shear layers altered its velocity and shape. I have estimated the outflow thicknesses by measuring the upper and lower extents of the dyed water 0.15 m from the middle of the plume (table 6.1). For each experiment any spreading of the weak plume outflow at a given depth was nearly always in the same direction. Specifically, intrusions at depths $0.40 < \zeta < 0.47$ and $0.77 < \zeta < 0.87$ were always directed away from the strong plume while intrusions in depths $0.32 < \zeta < 0.40$ and $0.51 < \zeta < 0.74$ were always directed towards the strong plume. The thickness of the weak plume outflow also varied depending on Φ. For small Φ, the weak plume intrusions were at shallower depths leading to outflows of smaller volume fluxes and thinner intrusion layers.

6.5. Discussion and Conclusion

6.5.1 The Two-Plume Model

Both the theoretical predictions and experiments in the two plume "filling-box" model indicate that the environmental density profiles and circulation patterns were dominated by the strong plume. The region below the spreading depth of the weak plume could only be refreshed by the strong plume. Waters and tracers from the weak plume could only reach this lower region if they first spread into the environment at a shallower depth and were subsequently entrained into the strong plume. As a result, the influence of the weak plume on this lower region was rather limited.

The dominance of the strong plume complements the findings for a time-varying single buoyancy source (Killworth and Turner, 1982). They found that at large times the plume from the time-varying source reached the bottom only when the source flux was

	weak plume at end of tank	weak plume in middle of tank	
Φ	spreading towards strong plume	spreading towards strong plume	spreading away from strong plume
0.30	0.64 - 0.77	0.66 - 0.74	0.74 - 0.87
0.25	0.62 - 0. 74	0.60 - 0.72	0.74 - 0.87
0.20	0.51 - 0.68	0.51 - 0.68	none
0.15	0.53 - 0.64	0.53 - 0.70	none
0.10	0.32 - 0.40	0.36 - 0.38	0.40 - 0.47
0.05	0.32 - 0.38	0.34 - 0.36	0.40 - 0.47

Table 6.1. The spreading depths of the weak plume outflow at large times at 0.15 m from the weak plume in tank B experiments. Where the weak plume was placed at the end of the tank opposite the strong plume the spreading depths are given for the outflow moving towards the strong plume. Where the weak plume was placed in the middle of the tank the spreading depths are given separately for the outflow moving towards and away from the strong plume.

maximal. During the remainder of the cycle, when the buoyancy flux was smaller, the plume was no longer dense enough to reach the bottom and produced an intermediate-depth outflow that was smaller in volume flux and left the bottom waters untouched. Thus the bottom waters were replenished only during the maximal phase of the buoyancy source. The time-varying single source during the maximal phase provides an analogy for the strong plume in the two plume case while at other times, it behaves like a weak plume.

In the experiments, where the buoyancy sources supplied a small volume flux of dense water into the tank, the volume of water in the system increased at all times. If an experiment was allowed to continue to very large times, the first front would rise above the depth of the nozzles. If this occurred, density differences between the source solutions and the environment would be reduced and the sources would effectively have smaller buoyancy fluxes. However, in the theoretical model the sources originate from points where the volume fluxes are zero and so the first front never reaches the depth of

the sources; hence each source has a constant buoyancy flux at all times. Therefore the experiments at very large times are expected to be different to the theory. Fortunately, in each of the experiments, the steady state stratification in the environment was established well before the first front had reached the depth of the nozzles and the theoretical model is expected to be valid.

For the two plume case the predicted neutral buoyancy level of the weak plume gave a reasonable indication, although usually an underestimation, of the spreading depth for the weak plume outflow. However, the experiments also indicated that the background motions in the basin had a major influence on the spreading depth of the weak plume outflow. In tank B experiments for $\Phi = 0.3$, 0.25, 0.10 and 0.05 the bottom of the weak plume outflow was at a shallower depth if the weak plume was placed at one end of the tank instead of the middle of the tank. This was because the end wall prevented the outflow from spreading in a shear layer moving towards the weak plume. It spread only after it had been advected to the level of the next shear layer. In the long channel, the increased vertical advection near the end wall where the flow reflected to return in the layer above (chapter 4) might also have contributed to the shallower spreading depth.

Besides confining the weak outflow to spread in a particular direction at a given depth, the shear layers also influenced the spreading speed of an intrusion. The maximal horizontal velocity occurred at the centre of a shear layer. This also influenced the measurement of the spreading depth because often only the faster spreading parts of an intrusion were seen far away from the plume at their original spreading depths before being carried upward by vertical advection. For example, in the $\Phi = 0.3$ experiment of tank A, the plume outflow was mainly spreading at the bottom half of the second shear layer where there was strong shearing. The top of the plume outflow was seen to spread rapidly, but the bottom was observed at a shallower depth and was brought unusually close to the predicted neutral buoyancy level. The more rapid spreading of intrusions at the centre of shear layers might also have been responsible for the oscillations in the spreading depth observed for $\Phi = 0.05$ (figure 6.5f).

It is speculated that temporal variations in the background velocity profiles of the shear layers were responsible for the spreading depths in some tank A experiments to ascend to a peak before descending to their large-time depths (figures 6a and 6c, corresponding to $\Phi = 0.3$ and 0.2). It was shown in chapter 4 that shear layers were formed in a pre-stratified tank on a time-scale that depended on the travel time of internal waves through the tank. It was also found that the dominant vertical scale of the horizontal velocity structure decreased during the evolution of the shear layers. There were initially two shear layers and additional layers appeared until five or six layers were established. The evolution of shear layers in a stratification that is also developing is expected to be similar in structure to the pre-stratified system. However they are also expected to develop more slowly than in the pre-stratified system because the depth of the stratification during the early stages of the evolution is smaller. Therefore the shear layers in the present experiments were not fully established until most of the tank had been stratified. The increase in the outflow spreading depths in the $\Phi = 0.3$ and 0.2 experiments after $\tau \approx 3$ is consistent with the presence of shear layers that had not been fully established. The early shear layers were thicker and thus the maximal horizontal velocity in the second layer, where the outflow spread quickest, was found at shallower depths.

The results of Killworth and Turner (1982) indicated that stopping the sources and restarting them at a later time would have little effect on the environment density. This was exploited in two of the experiments in tank A ($\Phi = 0.25$ and $\Phi = 0.1$) where the sources were stopped every third minute to allow density profiles to be taken after all motions had ceased. In these two cases, the shear layers had insufficient time to develop while the sources were active and thus had no effect on the spreading of the weak plume outflow. As a result, the spreading depths for these two experiments (figures 6b and 6e) followed more closely the trend of the predicted neutral buoyancy level.

6.5.2 Multiple Plumes

The results and observations may be easily extended to cases where there are more than two plumes. In these cases, the plume from the strongest buoyancy source will establish the stratification and shear layers while each of the weaker plumes will descend to an intermediate depth and spread into the environment. The depths of the plume outflows can be predicted by the approximate analytical solution in §6.2.3 or by extending the numerical scheme described in §6.2.2 to include additional plumes. Lateral transport of the intrusions will again be largely controlled by the shear layer structure generated by the strongest plume. The distribution of tracers from the sources will depend also on where the plumes are located relative to one another. For example, one plume outflow may spread into the path of an outflow from another plume and mixing between the two outflows causes tracers to be found together.

6.5.3 Comparisons With Peterson's Multiple Plume Model

Peterson's study (unpublished, personal communication) of multiple plumes differed substantially from the approach described in this paper. He included a buoyancy flux attributed to vertical diffusion that at each depth balanced the combined downward flux of the sinking plumes and the upward flux of environmental advection and obtained a solution for a true steady state where the plume and environment properties do not change with time. The solution incorporated the character of a surface boundary layer through which the environment properties varied from the surface conditions to an asymptotically homogenous interior. This boundary layer had a thickness that depended on the buoyancy flux of the sources, the diffusivity constant and the length of the box but, importantly, not on the total depth of the box.

Two important consequences of the independence of the boundary layer from the box depth are that the stratification (and hence spreading depth of the weak plume) was a function of a depth that scaled with the boundary layer thickness rather than the total depth. The only similarities between Peterson's solution and the one presented in this paper are that both feature buoyancy frequencies that weakened with distance from the

surface and, for the two plume case, a lower weak plume spreading depth for increasing Φ. In Peterson's model the inclusion of diffusion removed the infinite density gradient found near the surface of the non-diffusive filling-box model. However, the assumption that the net buoyancy flux at a given depth is zero allows only the steady state to be calculated.

6.5.4 Conclusion

The "filling-box" equations of Baines and Turner (1969) have been extended to describe the case of two or more turbulent, well-separated plumes. For two plumes, the numerical solution confirms that the density profile of the environment is similar to that produced by a single plume. The predicted spreading depth for the weak plume, taken as its neutral buoyancy level, is a function of the ratio of buoyancy fluxes between the two sources.

Experiments showed the predictions for spreading depths of the weak plume need some adjustment. Firstly, the neutral buoyancy level is an underestimation of the actual spreading depth because excess momentum carries the plume to greater depths, resulting in some additional entrainment. Secondly, horizontal motions associated with shear layers influence the spreading of the weak plume's intrusion. These shear layers are primarily generated by the outflow from the strongest plume and are supported by the stratification generated by all the plumes. Weak outflows are forced to spread with the shear layer in which they are intruding, with the greatest lateral dispersion occuring at the depth of the maximal horizontal velocity in that layer. Thus small differences in the effective spreading depth of the plume accompany changes in the horizontal velocity profile. For the case of multiple plumes, a more complex model that takes into account of disturbances from a number of plume outflows is required to predict the shear layer velocity structure and dispersion of the weak plume outflows.

Chapter 7

Two-Basin Systems

7.1 Introduction

Naturally occurring basins are rarely the simple rectangular box as assumed in many studies, but instead have complex topographies that affect the convection within them. In this chapter I look at plumes in filling-boxes where there is a simple topographic feature in the form of a ridge that rises from the bottom to some depth in the interior. The ridge divides the box into two separate basins so that any exchange of water between the two basins is possible only over the sill, that is, the depth between the water surface and the top of the ridge. The presence of two basins alters the way in which plumes ventilate the box and therefore has implications for the stratification and water properties.

There are many multi-basin systems in the natural world. In the oceans, mid-ocean ridges separate the deep ocean to form many ocean basins of varying sizes. These basins act to collect water and restrict spreading to other parts of the oceans. For instance, the water properties of the deep Atlantic (figure 3.2) indicate that Antarctic Bottom Water is mainly found west of the mid-Atlantic ridge. On a smaller scale, marginal seas often collect dense water behind a ridge and, as the dense water overflows across the sill, they form outflows into the open ocean. Examples include the four outflows mentioned in table 3.1.

In this chapter, I show that the properties of the plumes and the environment are modified in the "filling-box" process by the presence of a ridge. In particular, I show how these properties depend on the height and position of the ridge. The method is formulated in §7.2. I look at single plume systems in §7.3 and two plume systems in §7.4. Discussions and conclusions are given in §7.5.

7.2 Methodology

The findings of this chapter are mainly theoretical and complemented by several experiments. The numerical scheme of chapter 6, which describes two plumes in a single-basin filling-box, is modified to take into account the constraints placed on the convection by the ridge. Let H be the total water depth as before and z_s the depth of the sill from the water surface (figure 7.1). The first and second basins (lying below the sill-depth) are assumed to have horizontal cross-sectional areas A_1 (> 0) and A_2 (> 0) independent of depth. The region above the ridge lies over both basins and is referred to as the common region. The buoyancy sources giving rise to the plumes descending into the first and second basin have fluxes F_1 and F_2 respectively, where $F_1 \geq F_2$. Furthermore, it is assumed that as each plume descends, it does not strike the side-walls or the ridge.

The system is assumed to be homogenous initially. Where there is a single plume ($F_2 = 0$), non-trivial cases occur only if the first basin is finite ($A_1 < \infty$). If $A_1 = \infty$, then no stratification is formed in the first basin and no dense plume water reaches the sill to overflow into the second basin. It is therefore assumed that $A_1 < \infty$, where a "filling-box" convection is immediately established in the first basin. An overflow into the second basin is eventually formed (figure 7.1). The plume, environment and overflow properties all evolve with time.

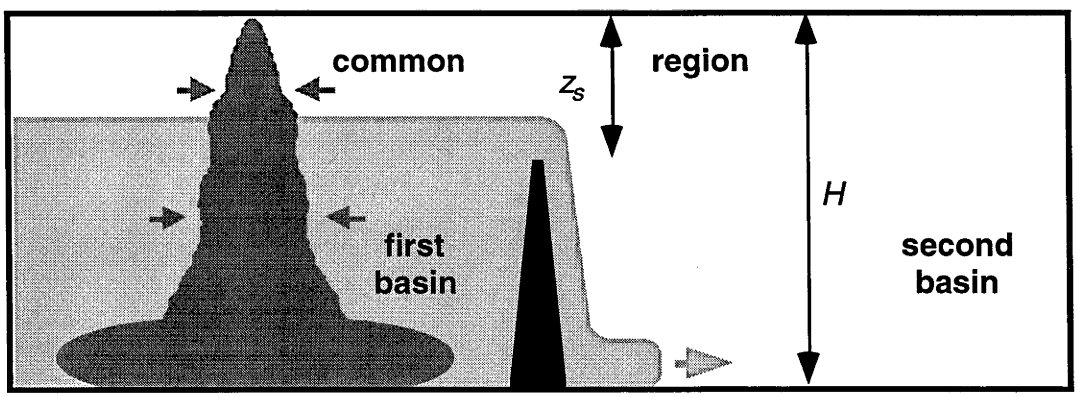

Figure 7.1. The single plume in a two-basin system showing the overflow across the sill.

Where there are two plumes, solutions which are non-trivial and effectively different to the single plume case occur only if both basins are finite. In this situation, each basin is initially stratified separately and as one or both basins fill, an overflow is generated from the basin that has the denser water at the sill-depth. The basin from which the overflow occurs contributes a buoyancy flux to the other basin through an injection of dense water. The time-dependent properties of the overflow depend upon the sill-depth, the strengths of the two sources and the cross-sectional areas of the two basins.

In this study, the overflow from one basin is assumed to descend into the other basin without entraining surrounding water. The overflow is likely to be only slightly denser than its surroundings and when compared to a plume, which is often much denser than its surroundings, buoyancy forces acting on the overflowing water are much smaller. The overflowing current attains comparatively small velocities and leads to relatively smaller Reynolds numbers. Therefore both the mixing with environment water and entrainment into the overflow are likely to be unimportant. In applications where the overflowing current descends slopes, entrainment will be even less important.

The presence of the ridge directly affects the environmental density and the advection of water. The variables describing the plume properties are as in chapter 6, but in the environment there are, for each basin, separate buoyancies f_{1e} and f_{2e} as well as advection velocities v_1 and v_2. The non-dimensional scalings (2.4) are carried over, but with $F = F_1 + F_2$ (as in chapter 6) and the cross-sectional area A replaced by A_1. Thus dimensionless times in the two-basin system are scaled as for a single-basin filling-box with the same size as the first basin. The split in buoyancy fluxes between the two sources is indicated by $\Phi = F_2/F$ (as in chapter 6) and the relative area of the two basins is indicated by $\alpha = A_1/A_2$. The sill-depth is also non-dimensionalised to $\zeta_s = z_s/H$.

The numerical scheme in chapter 6 is adapted to two-basin systems as follows: the plume equations (6.3) and (6.5) are unchanged and integrated separately as before, but using the appropriate environment buoyancy f_{1e} or f_{2e}. After taking into account the overflow and the different horizontal cross-sections of the basins and regions, the advection equations (6.4a) are replaced by

$$v_1 = -\left(r_1^2 w_1 + \sigma_2\right) \qquad \text{for } \zeta \geq \zeta_s \text{ in basin 1,}$$

$$v_2 = -\alpha\left(r_2^2 w_2 + \sigma_1\right) \qquad \text{for } \zeta \geq \zeta_s \text{ in basin 2} \tag{7.1}$$

and

$$v = -\frac{\alpha}{\alpha+1}\left(r_1^2 w_1 + r_2^2 w_2\right) \qquad \text{for } \zeta < \zeta_s \text{ in the common region.}$$

The σ_i represent the volume flux of the overflow from the ith basin if that basin has the denser environment water at the sill-depth. The overflow is assumed to inject its volume into the neutral buoyancy level in the other basin (or the bottom if it is denser than all the water of that basin) to create additional upwelling between the sill-depth and the injection level. Since the overflow volume flux is the same as the volume flux entering the overflowing basin through the plume in that basin, σ_i is defined as

$$\sigma_1(\zeta) = r_1^2(\zeta_s) w_1(\zeta_s) \qquad \text{if } f_{2e}(\zeta_s) < f_{1e}(\zeta_s) \text{ and } f_{2e}(\zeta) < f_{1e}(\zeta_s),$$

$$\sigma_1(\zeta) = 0 \qquad \text{otherwise,}$$

and

$$\sigma_2(\zeta) = r_2^2(\zeta_s) w_2(\zeta_s) \qquad \text{if } f_{1e}(\zeta_s) < f_{2e}(\zeta_s) \text{ and } f_{1e}(\zeta) < f_{2e}(\zeta_s),$$

$$\sigma_2(\zeta) = 0 \qquad \text{otherwise.}$$

The second environment equation (6.4b), stating that changes in buoyancy are the result of advection only, remains valid within each basin or region. The environment equations are integrated first for the overflowing basin from the bottom to the sill-depth to give the buoyancy in that basin. Integration in the other basin and in the common region gives the environment buoyancy in the other parts of the system. Because water is removed from the overflowing basin at the sill-depth and injected at some depth in the other basin, there is a discontinuity of buoyancy between the overflowing basin and the common region.

The overflow buoyancy flux F_o is defined as the product of the overflow volume flux and the buoyancy difference at the sill between the two basins. To distinguish between the two overflow directions, F_o is assumed to be positive if the overflow is from the first basin to the second basin so that

$$\frac{F_o}{F} = r_1^2(\zeta_s) w_1(\zeta_s)\left\{f_{1e}(\zeta_s) - f_{2e}(\zeta_s)\right\},$$

and negative if the overflow is from the second basin to the first basin, giving

$$\frac{F_o}{F} = -r_2^2(\zeta_s)w_2(\zeta_s)\{f_{2e}(\zeta_s) - f_{1e}(\zeta_s)\}.$$

7.3 Single-Plume Systems

When a single plume descends into an unstratified two-basin system, its properties and that of the basin it is sinking into are initially the same as if the plume is descending in the usual single-basin filling-box. The first front's position in the first basin is therefore given by (2.8) until it reaches the sill-depth where the front remains while the dense water drains away in the overflow. Thus for a sill-depth of ζ_s, the dimensionless time τ_o taken for the first overflow to occur is

$$\tau_o = \frac{5^{4/3}}{2^{1/3}3^{2/3}}\left(\zeta_s^{-2/3} - 1\right). \tag{7.2}$$

Figure 7.2 gives a plot of τ_o as a function of ζ_s. For $\tau > \tau_o$, the first basin supplies to the second basin a (dimensionless) volume flux q_o equivalent to the volume flux entering the first basin through the (only) plume, $r^2(\zeta_s)w(\zeta_s)$. Therefore, while the common region remains unstratified, (2.7) gives

$$q_o = \frac{3^{5/3}}{2^{2/3}5^{4/3}}\zeta_s^{5/3}.$$

If $\alpha = 0$ (that is, $A_2 = \infty$), the stratification in the second basin is not affected by the overflow and so the first basin resembles a "leaking" filling-box where the water in the overflow is released into the second basin but never returns to affect the plume nor the first basin. Through entrainment of dense water in the first basin, both the plume outflow and first basin become progressively denser, as does the overflow. However, the volume flux of the overflow q_0 remains constant because the common region continues to be unstratified. Furthermore, the buoyancy flux leaving the basin in the overflow is limited by the buoyancy flux entering the first basin through the plume, which is the same as the buoyancy flux of the source (one dimensionless unit). If at large times, the buoyancy flux leaving in the overflow is also one dimensionless unit and f_o^∞ is the dimensionless buoyancy of the overflow, then

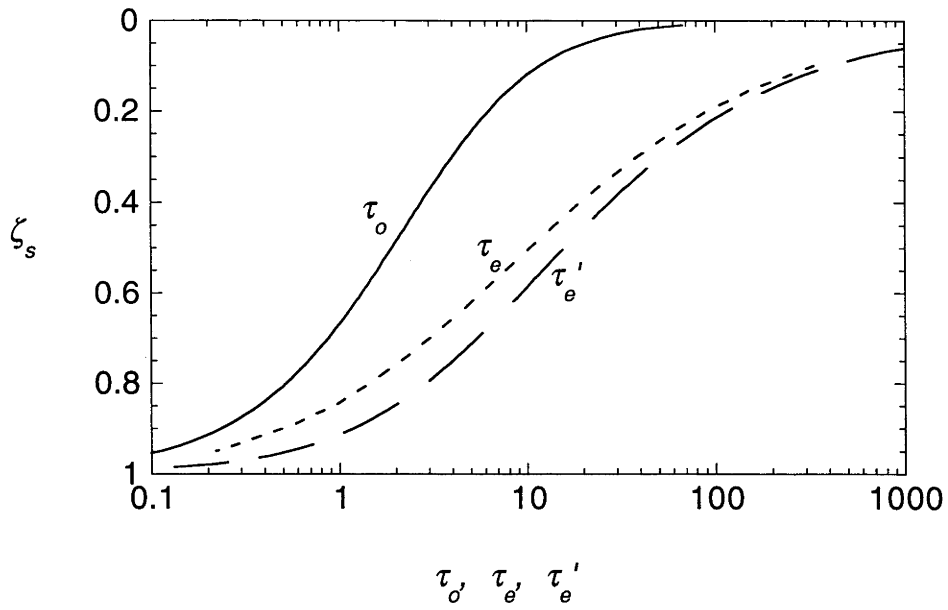

Figure 7.2. The time for the overflow to first occur τ_o (————) in a single plume two-basin system as a function of sill-depth ζ_s. The time is the analytical prediction (7.2) which assumes that the system is initially unstratified. For the case where the second basin is infinitely large, the time taken for the system to approach the two-layered steady state is also plotted as τ_e (- - - - - - - - -), which is numerically obtained, and τ_e' (—— ——), which is the analytical approximation (7.3).

$$f_o^\infty = \frac{1}{q_o}.$$

Since water in the overflow originates from a plume outflow that is originally at the bottom of the first basin, the large-time environment buoyancy f_{1e}^∞ also approaches the uniform value f_o^∞. The numerical results confirm that the first basin becomes homogenous with buoyancy f_o^∞.

The buoyancy profiles obtained numerically for $\zeta_s = 0.5$ (figure 7.3) show the evolution of the stratification in the first basin. Because the system asymptotically approaches the steady state, an evolution time τ_e can be assumed to be the time taken for the overflow buoyancy flux to reach say 99% of the source flux. Figure 7.2 includes a plot of τ_e against ζ_s. As the sill-depth decreases, the evolution time increases rapidly.

The time taken for the asymptotic two-layered system to develop from the initially unstratified system can also be estimated analytically by assuming that the first basin is

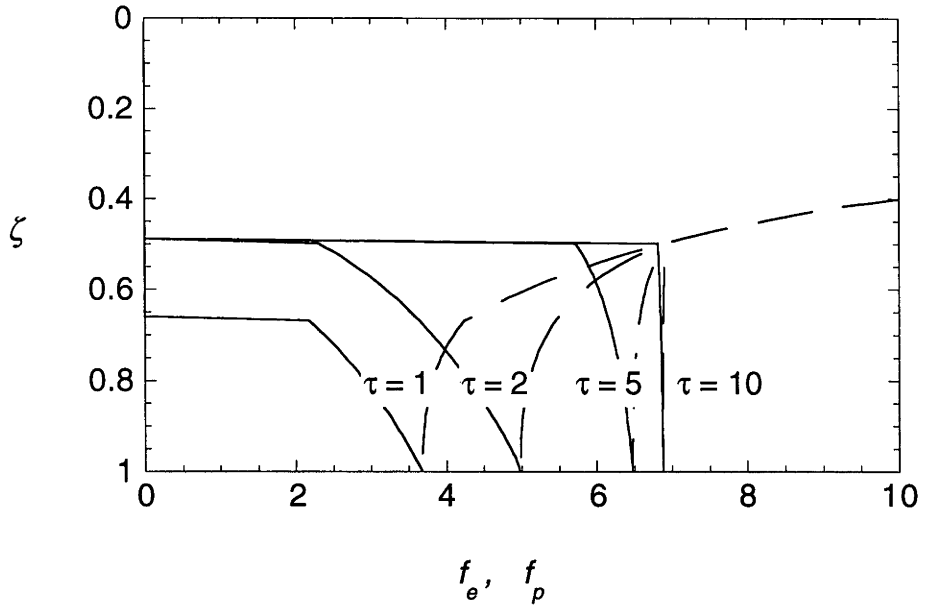

Figure 7.3. The profiles of the environment buoyancy f_e (————) and plume buoyancy f_p (—— ——) during their evolution to the two-layered state where $\zeta_s = 0.5$.

homogenous throughout the evolution of its stratification. Let $f_{1e}(\tau)$ be the buoyancy in the first basin. If the increase in buoyancy in the first basin as a result of the plume is assumed to be evenly distributed through the first basin then it can be calculated as $1/(1-\zeta_s)$. The decrease in buoyancy as a result of the overflow is similarly calculated as $f_{1e}(\tau)q_o/(1-\zeta_s)$. Hence

$$\frac{df_{1e}}{d\tau} = \left(\frac{1-f_{1e}(\tau)q_o}{1-\zeta_s}\right)$$

for which

$$\tau = \frac{\zeta_s - 1}{q_o}\ln\left(1-f_{1e}(\tau)q_o\right).$$

The time taken to reach the true steady state where $f_{1e}(\tau)q_o = 1$ is infinite, but if it is again assumed that the steady state is approached when $f_{1e}(\tau)q_o = 0.99$, then an estimate for the evolution time τ_e' is given by

$$\tau_e' = \ln(100)\frac{2^{2/3}5^{4/3}}{3^{5/3}}\zeta_s^{-5/3}(1-\zeta_s) \qquad (7.3)$$

(figure 7.2). Agreement with τ_e is reasonably good, especially for small ζ_s.

A totally different solution appears when $A_2 < \infty$. In this case, the second basin is stratified by the sill overflow. A density front forms in the second basin between the dense overflow water and the overlying homogenous water. It advects up to pass the sill and travel through the common region. A continuous buoyancy profile carries through from the second basin into the common region, but the density front between the first basin and the common region remains near the sill-depth to separate the overflowing water and the relatively lighter water above coming from the second basin. As the plume entrains stratified water from the common region the buoyancy of the whole system increases with time and the system resembles the usual filling-box.

Figure 7.4 shows the evolution of the environment buoyancy profile in the case of $\zeta_s = 0.5$ and $\alpha = 1$. The first overflow occurs just before $\tau = 2$. The front in the second basin passes the top of the ridge just after $\tau = 5$. Its rate of movement slows abruptly on passing the sill-depth because the cross-sectional area over which the front advects increases suddenly on reaching the larger common region. At large times the familiar "filling-box" stratification is found in the common region. Below the ridge denser water is found in the first basin and less dense water in the second basin.

In the single-basin filling-box the supply of buoyancy by the plume increases the buoyancy evenly through the box at large times. Numerical results indicate that this also occurs in the two-basin filling-box. Thus the large-time buoyancy flux across the sill, which is the sole supply of buoyancy to the second basin, depends on the volume of the second basin relative to the whole box. The large-time buoyancy flux F_o of the overflow is given by

$$F_o = \frac{F}{\alpha + 1}(1 - \zeta_s). \tag{7.4}$$

For $\alpha = 1$, figure 7.5 gives plots of F_o as functions of τ / τ_o for $\zeta_s = 0.25,\ 0.5$ and 0.75. In each case, the overflow buoyancy flux first becomes larger as the water in the first basin becomes denser. But as the overflow fills the second basin and denser plume-derived water reaches the sill-depth in the second basin, the density difference between the waters in the overflow and in the second basin at the sill-depth decreases and the

(a)

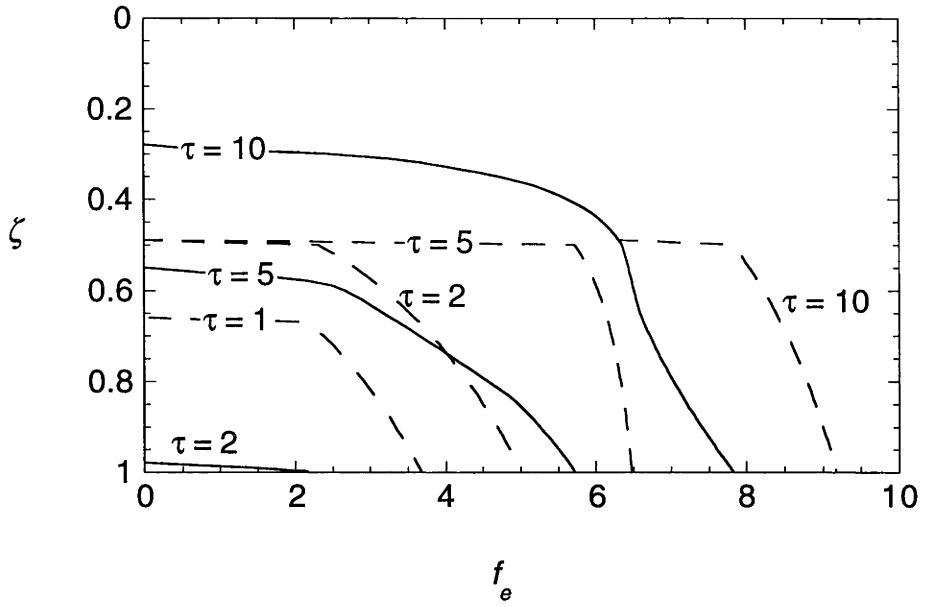

(b)

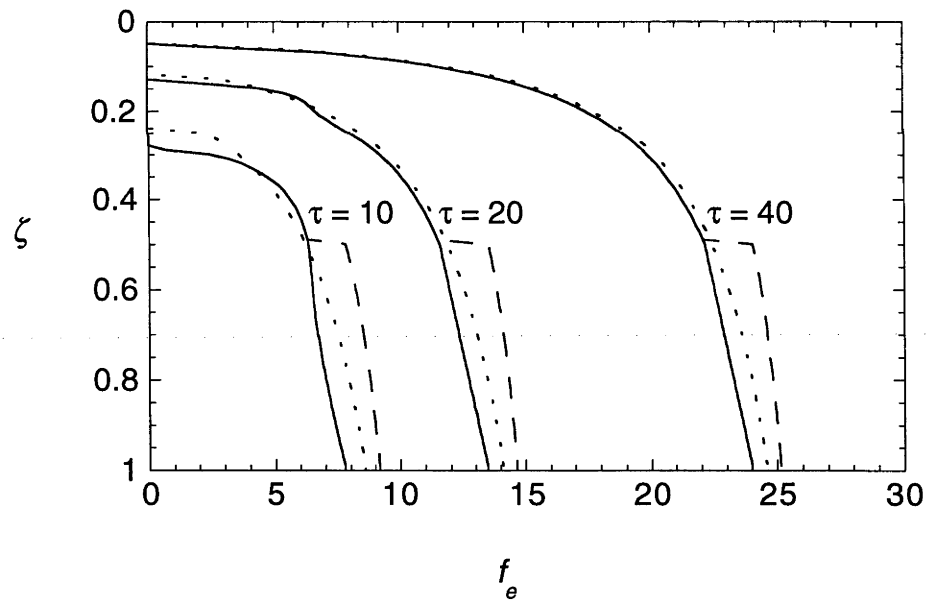

Figure 7.4. The buoyancy profiles in the environment for the single-plume two-basin system where $\zeta_s = 0.5$ and $\alpha = 1$. In both graphs, the profiles for the first basin are given by —— —— while the profiles for the second basin below $\zeta = 0.5$ and for the common region above $\zeta = 0.5$ are given by ——————. In (b), the profile for the single-plume in the usual single-basin filling-box (of area $A_1 + A_2$) is also given for comparison (- - - - - - - -).

overflow buoyancy flux drops abruptly. Smaller adjustments to F_o also occur as denser water arrives in the common region and is entrained by the plume In each case, F_o asymptotically approaches the predicted large-time flux (7.4).

7.4 Two-Plume Systems

When two plumes descend into two basins, the properties of the system not only depend on the sill-depth and the relative cross-sectional areas of the two basins, but also on the relative buoyancy fluxes of the two sources. As the number of possibilities is large, I only give a limited set of results to illustrate the trends that occur as each of the parameters is varied. Because the first basin contains the plume from the stronger source the overflow is usually from the first basin into the second. However, as I show later, an exception to this occurs when the size of the second basin is very small.

When both basins are of equal sizes ($\alpha = 1$), the overflow is always from the first basin into the second. At the start each basin is filled by the plume descending into it in the usual "filling-box" manner. The first basin fills up before the second basin because the strong plume has a higher volume flux at the sill-depth. When the overflow forms,

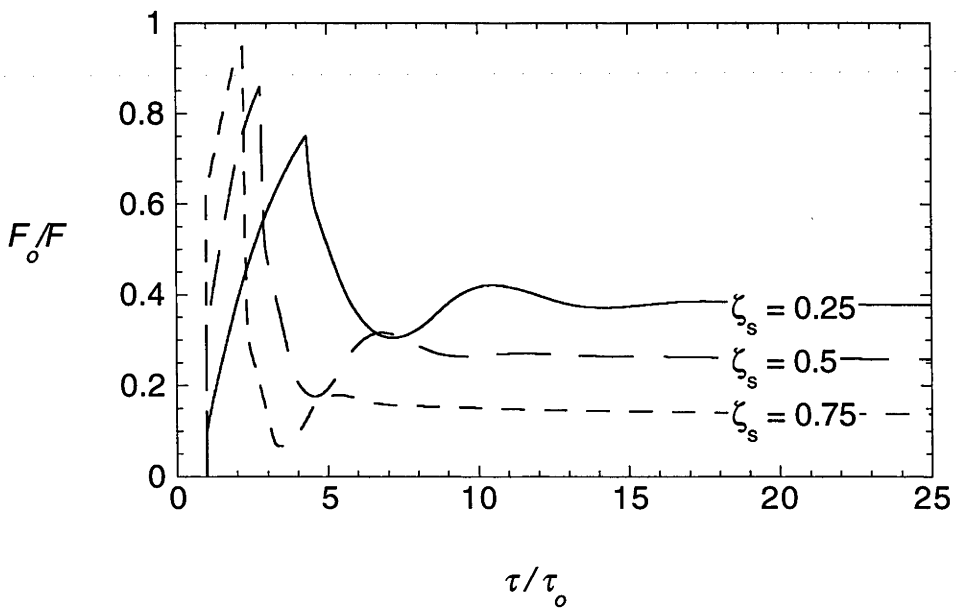

Figure 7.5. The buoyancy flux F_o in the overflow for the single-plume two-basin system for $\zeta_s = 0.25$, 0.5 and 0.75 where $\alpha = 1$.

the depth to which it sinks depends on the stratification in the second basin. This is illustrated by the neutral buoyancy levels of the overflow and the weak plume for $\zeta_s = 0.5$ (figure 7.6) for $\Phi = 0.1$, 0.25, 0.35 and 0.45. In the case of $\Phi = 0.45$, the plumes are similar in strength and hence the buoyancy profiles are fairly similar in both basins. Initially, the water in the overflow, which comes from the top of the first basin, is only as dense as the water in the second basin at $\zeta = 0.55$. At later times, when the stratifications in the two basins have developed further, the overflow neutral buoyancy level is deeper (at a depth just below $\zeta = 0.65$). For $\Phi = 0.35$, the overflow initially spreads at $\zeta \approx 0.72$ but quickly descends all the way to the bottom. As soon as the overflow reaches the bottom, the weak plume is no longer sufficiently dense to sink to the bottom and its outflow forms an intrusion into the interior of the second basin. For $\Phi = 0.25$ and 0.1, the overflow is sufficiently dense to sink to the bottom as soon as it is formed and changes the weak plume bottom outflow in the second basin into a mid-depth intrusion. In these cases, the neutral buoyancy level of the weak plume rapidly rises as dense overflow water gathers at the bottom of the second basin, but the level asymptotically approaches a final steady depth. At large times the weak plume in the $\Phi = 0.25$ case is still dense enough to sink into the second basin, but in the $\Phi = 0.1$ case, it is too light and instead forms an intrusion into the common region.

In figure 7.7, the stratifications in both basins for $\zeta_s = 0.5$ and $\Phi = 0.1$ at $\tau = 1.74$, 3.48, 8.70 and 13.92 are shown. Although neither density front in the two basins has reached the sill at $\tau = 1.74$, the differences in the advection speeds of the two fronts and the buoyancies in the two basins are very distinct. At $\tau = 3.48$, the effects of the dense overflow can be seen at the bottom of the second basin. By $\tau = 8.70$, overflowing water from the first basin has advected through the depths of the second basin to move into the common region above the sill, pushing ahead of it the less dense water collected in the second basin at earlier times. This volume of less dense water is responsible for the relatively linear buoyancy profile in the common region. As additional dense water reaches depths above the sill and entrainment into both plumes withdraws water from the common region, the buoyancy profile changes to approach the familiar

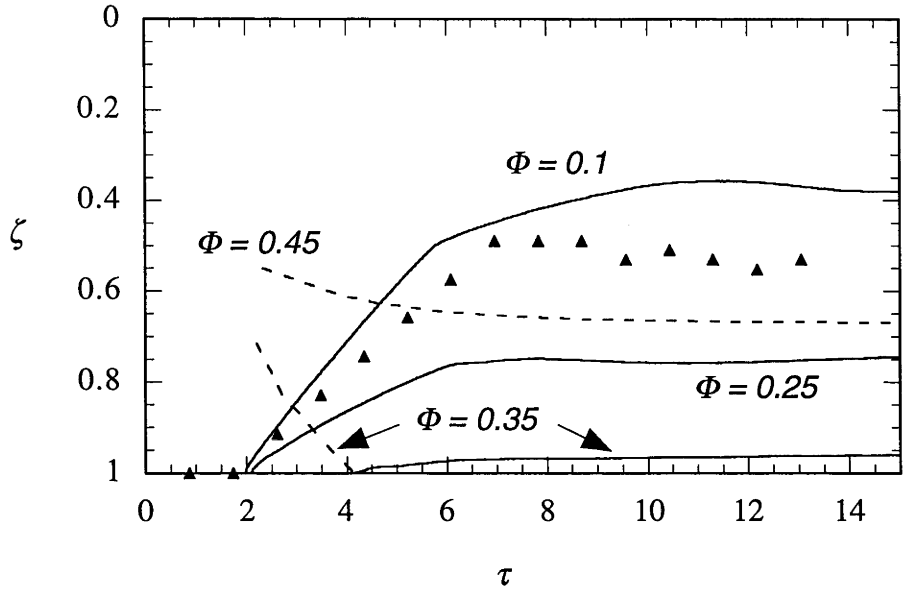

Figure 7.6. For $\zeta_s = 0.5$, $\alpha = 1$ and $\Phi = 0.45$, 0.35, 0.25 and 0.1, the neutral buoyancy levels of the overflow (- - - - - - - -) and weak plume (————) in the second basin. The plots for the neutral buoyancy level of the overflow for $\Phi = 0.25$ and 0.1 and for the weak plume for $\Phi = 0.45$ lie exclusively on $\zeta = 1$. Also plotted is the bottom of the weak plume's outflow (▲) for a $\Phi = 0.1$ experiment described in §7.4.

plume-shape stratification of single-basin filling-boxes ($\tau = 13.92$). The rapid sharpening of the buoyancy gradients just below the advancing density front, which accompanies the change to a plume-shape stratification, is responsible for the small change in the spreading depth of the weak plume between $\tau = 10$ and 14 (figure 7.6). During this period buoyancies at different depths increase unevenly so that the neutral buoyancy depth of the weak plume is lowered slightly. Although the descent is small and is not likely to be noticed in applications, it is nevertheless an interesting feature of many two-plume two-basin systems. In comparison, when two plumes descend into a single basin, the weak plume outflow is not collected separately in a basin, but interacts with the strong plume. In that case the environment attains the familiar plume stratification quickly and no increase of the weak plume's neutral buoyancy depth is seen at any time.

I conducted a single experiment to verify the numerical predictions for environment buoyancies and weak plume spreading depths in two-basin systems. The

a)

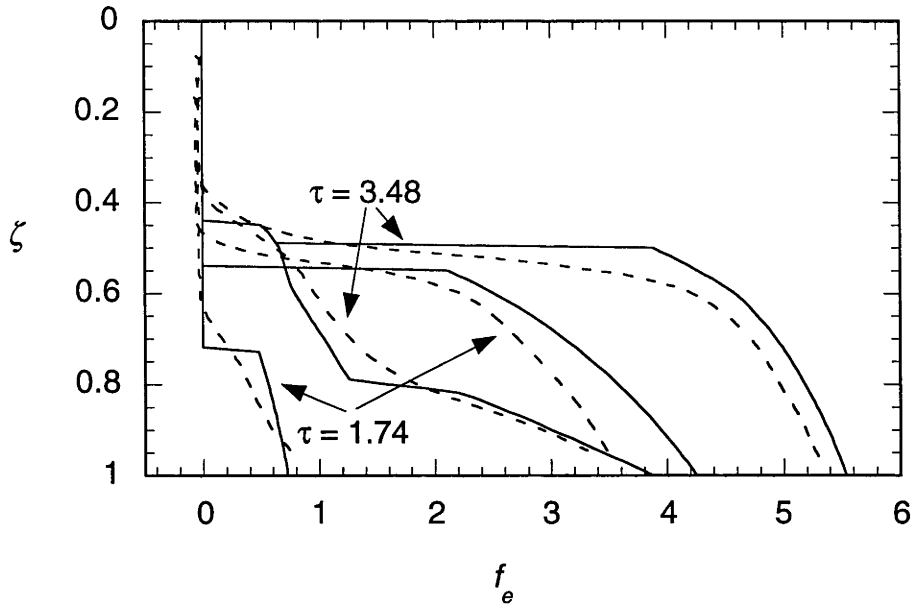

b)

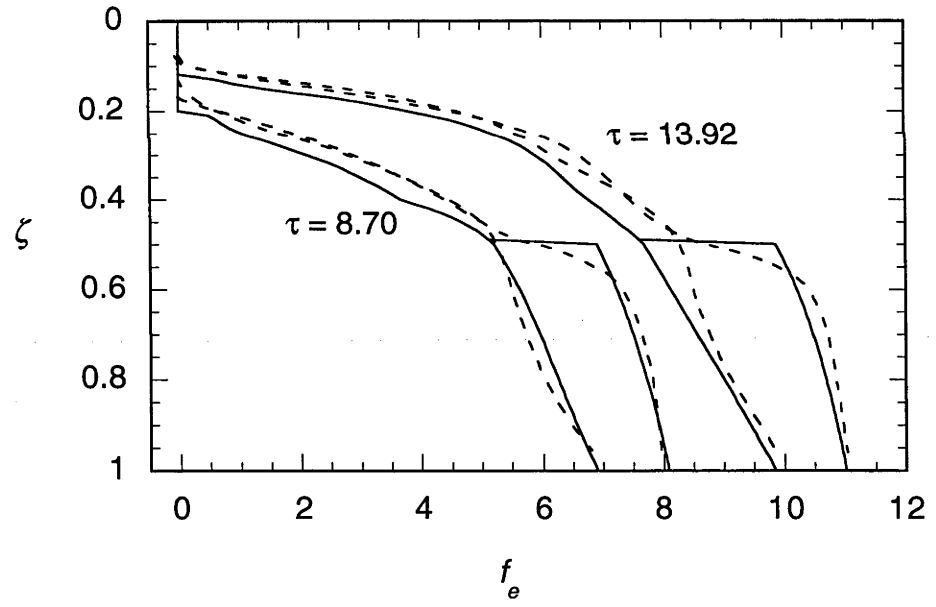

Figure 7.7. The predicted (————————) and experimentally observed (- - - - - - - - -) environment buoyancies, f_{1e} and f_{2e}, in the case where $\zeta_s = 0.5$, $\alpha = 1$ and $\Phi = 0.1$ at (a) $\tau = 1.74$ and 3.48 and (b) $\tau = 8.70$ and 13.92. Below the bifurcation in each plot, the right and left branches refer to buoyancy in the first and second basins respectively. Above the bifurcation, the plot refers to the common region ($\zeta < 0.5$) or to both basins ($\zeta > 0.5$).

experiment used a 1.1 m × 0.3 m × 0.24 m tank initially filled with fresh water. The two basins were separated by a ridge that rose 0.12 m from the bottom, vertical on the side of the first basin but at a 45° angle on the side of the second basin. It separated the tank into two basins of roughly equal size, although the top of the second basin was approximately 20% larger than the bottom. The slope reduced any entrainment into the overflow. The sources in the first and second basins injected salt water of density 1180 kg m^{-3} and 1020 kg m^{-3} respectively, both at a volume flux of 0.395×10^{-6} m^3 s^{-1}. The parameters of this experiment were therefore $\zeta_s = 0.5$, $\Phi = 0.1$ and $\alpha = 1$. During the 30 min duration of this experiment, the depth at which the bottom of the weak plume's outflow spread into the second basin was measured every two minutes; the data are plotted in figure 7.6. Every four minutes, buoyancy profiles were obtained in both basins and a selection of these corresponding to $\tau = 1.74$, 3.48, 8.70 and 13.92 are plotted in figure 7.7. Agreement between the predicted and experimentally observed results is good.

Figure 7.6 identifies four main flow regimes that exist for two-plume two-basin systems. The four regimes are displayed in figure 7.8. Regime I exists in all cases at the start when the overflow across the sill has not yet developed and each plume descends to the bottom to fill and stratify its own basin independently. When the overflow occurs, either regime II or III develops. In regime II, the overflow spreads at an intermediate depth while the plume in the basin receiving the overflow continues to spread at the bottom. In regime III, the overflow spreads at the bottom while the plume in the basin receiving the overflow lifts off to spread at an intermediate depth. Regime IV is an extension to regime III where the plume has lifted so far that it spreads above the ridge. Thus for $\zeta_s = 0.5$ and $\alpha = 1$ (figure 7.6), the $\Phi = 0.45$ case displays regime I initially and regime II after the overflow occurs. The $\Phi = 0.35$ case also displays regime I initially and regime II immediately after the overflow forms, but evolves to regime III. The $\Phi = 0.25$ and 0.1 cases jump directly from regime I to regime III, with the $\Phi = 0.1$ case also progressing to regime IV.

For $\alpha = 1$ the flow regimes exhibited for different ζ_s and Φ are given in a phase diagram shown in figure 7.9. The flow regimes are deduced from numerical simulations

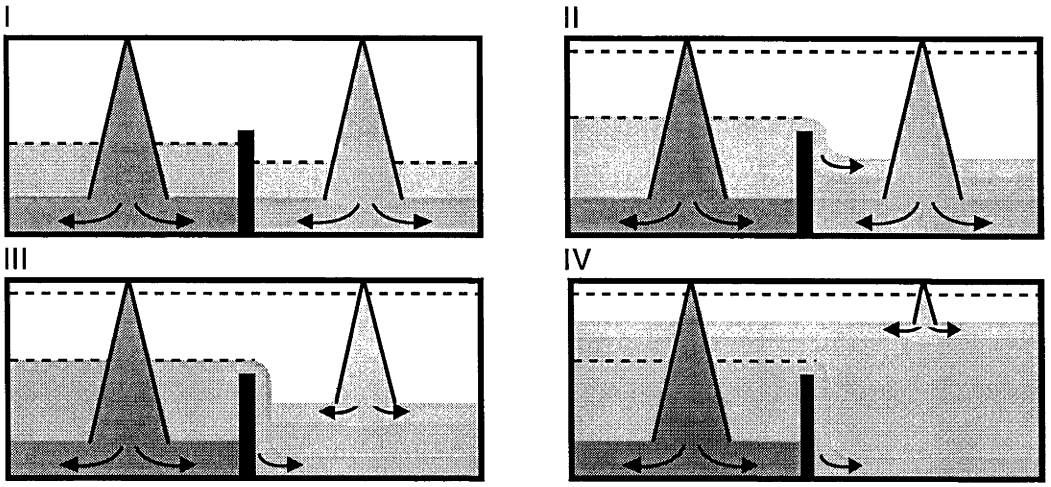

Figure 7.8. The four flow regimes of two-plume two-basin systems, showing the type of spreading of the plume outflows and sill overflow. In the diagrams for regimes II, III and IV the left basin is the overflowing basin. Density fronts are indicated by broken lines. Note that the diagrams are not drawn to scale.

from the start to the time when the first front has advected to $\zeta = 0.05$. During this time, the system has effectively evolved to the steady state for cases where $\zeta_s > 0.4$ and the regime at the end of the simulation is representative of that at even larger times. However, for $\zeta_s < 0.4$, the steady state has not yet been reached when the simulation is stopped and the boundaries for transition between different steady state regimes are only approximate for $0.2 < \zeta_s < 0.4$. For $\zeta_s < 0.2$, the time required for the system to reach the steady state is much longer than the time required for the first front to reach $\zeta = 0.05$ and it was impractical to calculate the boundaries for the flow regimes.

When the first front is at $\zeta = 0.05$, the depth to which the weak plume descends is given in figure 7.10 for $\alpha = 1$ and $\zeta_s > 0.4$. Starting from the single-basin situation ($\zeta_s = 1$), the spreading depth of the weak plume is unchanged if the ridge height is as high as the spreading depth of that particular weak plume in the single-basin case. This is because the stratification above the ridge is virtually the same as in the single-basin system. However, if the ridge is higher, then the spreading depth is lowered; in these situations the weak plume penetrates the second basin where, compared to the same depths in the single-basin system, the water is less dense.

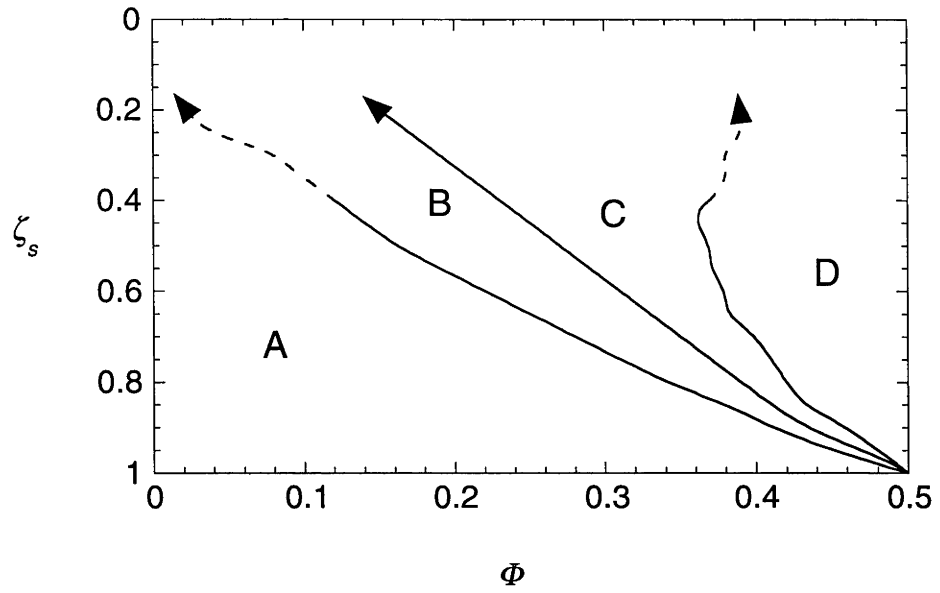

Legend:

Area	Regimes from start to steady state (refer figure 7.8)
A	I → III → IV
B	I → III
C	I → II → III
D	I → II

Figure 7.9. The flow regime phase diagram for $\alpha = 1$. The vertical axis is the sill-depth ζ_s while the horizontal axis is the ratio of the buoyancy flux of the weak source to the total flux, Φ. The two dotted boundaries for $0.2 < \zeta_s < 0.4$ indicate the transition in the large time flow regimes are only approximate (see text).

The (dimensionless) steady state buoyancy flux F_o/F across the sill for $\Phi = 0.4$, 0.25 and 0.1 is plotted in figure 7.11 for different ζ_s. Where the weak plume spreads above the ridge, the increase in buoyancy in the second basin is solely supplied by the overflow from the first basin and F_o is given by (7.4). Where the weak plume spreads below the ridge, part of the buoyancy in the second basin is supplied by the weak plume and F_o is therefore less than that predicted by (7.4).

I now consider the effects of varying the sizes of the two basins. The first overflow is from the second basin into the first basin if the filling-time of the second basin is less than that for the first basin. Noting that the dimensionless time τ is scaled to the

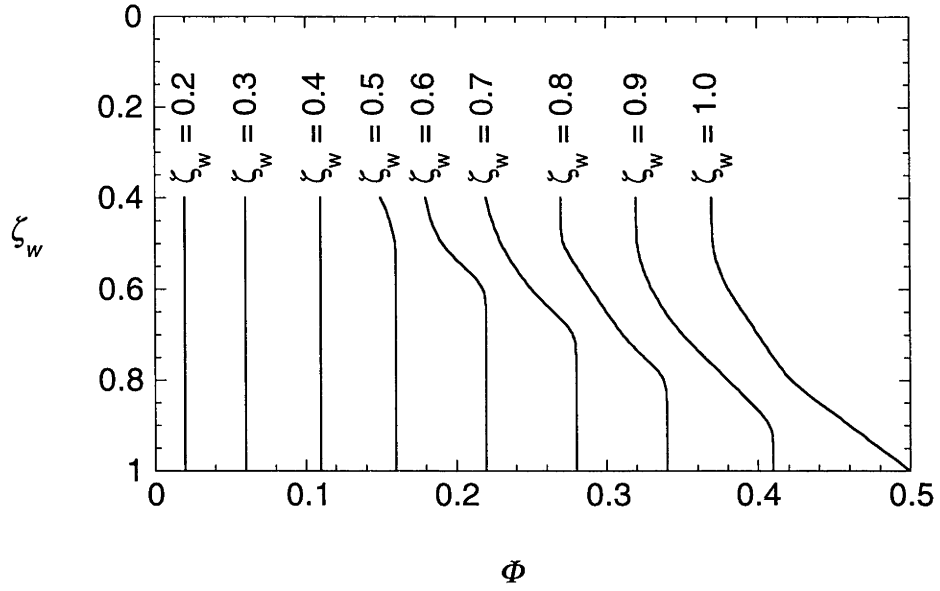

Figure 7.10. For $\alpha = 1$, the loci of constant spreading depth of the weak plume ζ_w at the steady state. The vertical axis is the sill-depth ζ_s while the horizontal axis is the dimensionless buoyancy flux of the weak source Φ.

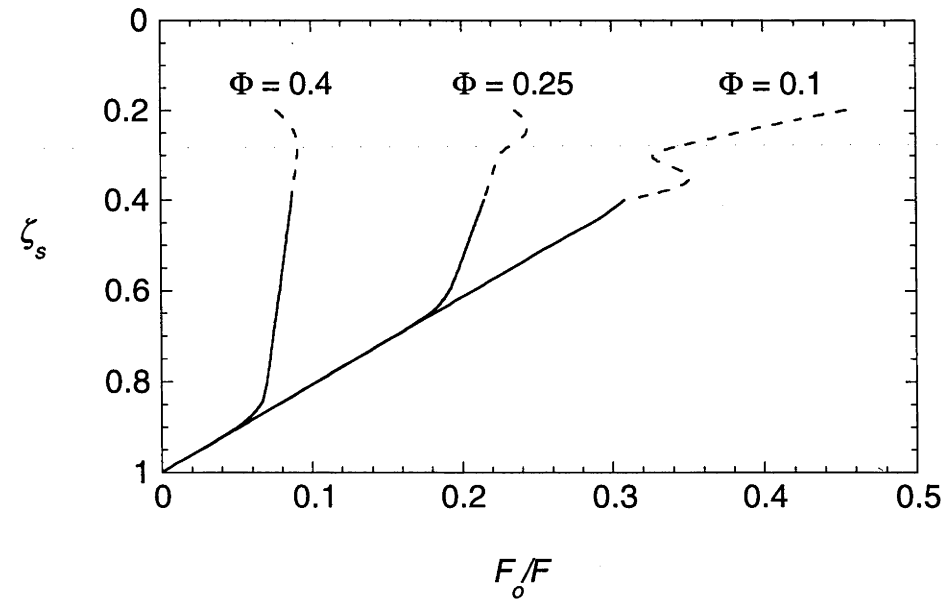

Figure 7.11. For $\alpha = 1$ and $\Phi = 0.1$, 0.25 and 0.4, the variation of the dimensionless overflow buoyancy flux F_o/F with ζ_s at a time when the first front is at $\zeta = 0.05$. For $0.2 < \zeta_s < 0.4$ (dotted lines), the overflow buoyancy flux had not yet fully evolved to its steady state flux.

area of the first basin A_1, the dimensionless times τ_{1o} and τ_{2o} required for the first and second basins to be filled are respectively

$$\tau_{1o} = \frac{5^{4/3}}{2^{1/3}3^{2/3}} \frac{F^{1/3}}{F_1^{1/3}} \left(\zeta_s^{-2/3} - 1\right)$$

and

$$\tau_{2o} = \frac{5^{4/3}}{2^{1/3}3^{2/3}} \frac{F^{1/3}}{F_2^{1/3}} \frac{1}{\alpha} \left(\zeta_s^{-2/3} - 1\right).$$

Thus the first overflow is from the second basin to the first basin if $\tau_{1o} > \tau_{2o}$, or equivalently, if

$$\alpha = A_1/A_2 > (F_1/F_2)^{1/3}. \tag{7.5}$$

If the overflow is from the first basin to the second basin, the overflow remains in that direction at all times. However, if the first overflow is from the second basin to the first basin, the overflow may switch to the opposite direction. I illustrate this with the $\zeta_s = 0.5$ case where the α–Φ phase diagram for the overflow direction is given in figure 7.12. In region A the overflow is always from the first basin to the second. An overflow from the second basin into the first occurs for any Φ if the second basin is filled faster than the first basin (regions B and C). A steady state overflow from the second basin only exists for sufficiently large Φ and α (region C). A neccessary but not sufficient condition for a steady state overflow from the second basin is a steady state bottom spreading of the weak plume. Because the stratification in the common region is very similar to that of the single-basin system, it is virtually independent of α. Hence, an approximate limiting value of Φ for steady state outflows from the second basin can be found from figure 7.9. Combinations of Φ and ζ_s which lie in region A of figure 7.9 have weak plume spreading depths above the ridge at large times ($\zeta_w < \zeta_s$) and these cannot lead to steady state overflows from the second basin for any α. For $\zeta_s = 0.5$, the condition is therefore $\Phi > 0.16$, a limit that is approached as $\alpha \to \infty$.

Three experiments were conducted in the case of $\alpha = 2.89$ with $\Phi = 0.1$, 0.25 and 0.45. As expected, the second basin filled up first in all three cases and resulted in overflows into the first basin. These overflows were weak and settled near the sill-depth

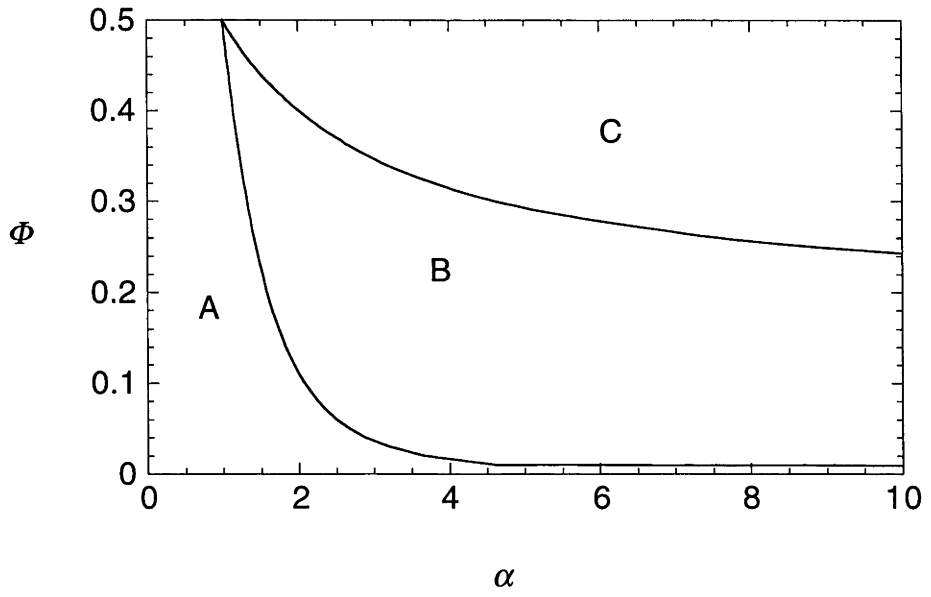

Figure 7.12. The α–Φ phase diagram for the direction of overflow across the sill in the case of $\zeta_s = 0.5$ when the first front is at $\zeta = 0.05$. In region A the overflow is always from the first basin into the second basin while in region C the overflow is always from the second basin into the first. In region B the initial overflow is from the second basin into the first, but switches to the other direction later.

in the first basin (for example, figure 7.13a). For $\Phi = 0.1$ and 0.25, the overflows from the second basin were brief and changed direction quickly to form overflows from the first basin into the second (figure 7.13b); this new overflow direction was maintained as the system evolved to the steady state. In the $\Phi = 0.1$ case, the subsequent overflow from the first basin lifted the weak plume from the bottom, causing it to spread as a mid-depth intrusion. For the $\Phi = 0.45$ case, the weak overflow from the second basin into the first persisted into the steady state. The overflow directions in these experiments are consistent with predictions given in the phase diagram of figure 7.12.

Plots for the large-time environmental buoyancy profiles for $\zeta_s = 0.5$, $\Phi = 0.25$ and $\alpha = 0.5$, 1, 3 and 20 are given in figure 7.14. When a basin is smaller, the ventilation of the environment by the plume and overflow is faster and hence density gradients become weaker; this applies to both basins. The densest water is always found at the bottom of the first basin, even if the second basin is supplying the overflow

a) b)

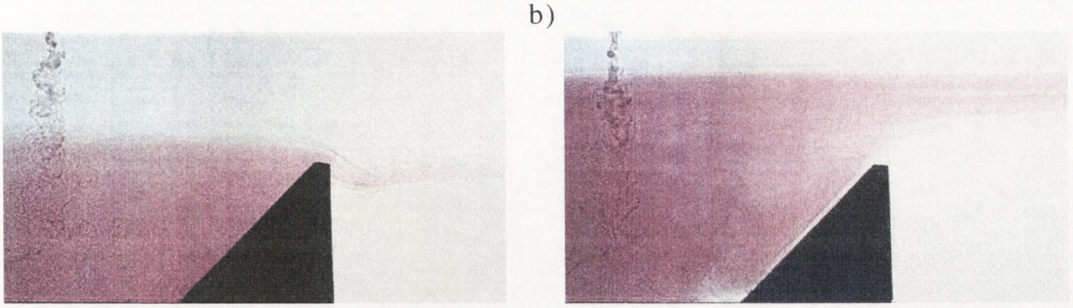

Figure 7.13. Two photographs from an experiment where $\zeta_s = 0.5$, $\Phi = 0.25$ and $\alpha = 2.89$. The source solution giving rise to the weak plume in the second basin (left of ridge) was dyed red. (a). A close up of the sill region early in the experiment which shows that the overflow of weak plume water is from the second basin (left) to the first basin (right). (b) The overflow reversed in direction so that at large times a small volume of undyed (clear) strong plume water was seen descending the sloping wall of the ridge.

($\alpha = 20$). The weakening of the density gradient in the second basin when α is larger also lowers the spreading depth of the weak plume ζ_w (figure 7.15).

Changes to the α–Φ phase diagram for ζ_s other than 0.5 are briefly discussed. Region A remains unchanged for all ζ_s because the condition (7.5) for the first overflow to originate from the second basin is independent of ζ_s. In the limiting case of $\zeta_s = 1$ where the "ridge" has zero height, the strong plume provides the bottom outflow at large times so that the "overflow" across the "ridge" is from the "first basin" into the "second". In this situation region C disappears and region B comprises the area defined by (7.5) and $\Phi < 0.5$. As the ridge height increases and ζ_s becomes smaller, region C expands from the line $\Phi = 0.5$ for $\alpha > 1$. At a given α (> 1) the boundary between regions B and C shifts to smaller Φ. When $\zeta_s \to 0$, region B disappears altogether, leaving only regions A and C. The limiting value for Φ on the boundary as $\alpha \to \infty$ changes from $\Phi = 0.5$ at $\zeta_s = 1$ to $\Phi = 0$ at $\zeta_s = 0$. Thus in the phase diagram, steady state overflows from the second basin grow in prevalence as ridge heights increase. The expansion of region C over region B occurs because when the two basins grow in depth, the inter-basin convection is increasingly restricted by the taller ridge. Ventilation times of the two basins then become more important in determining the direction of the steady-state overflow.

a)

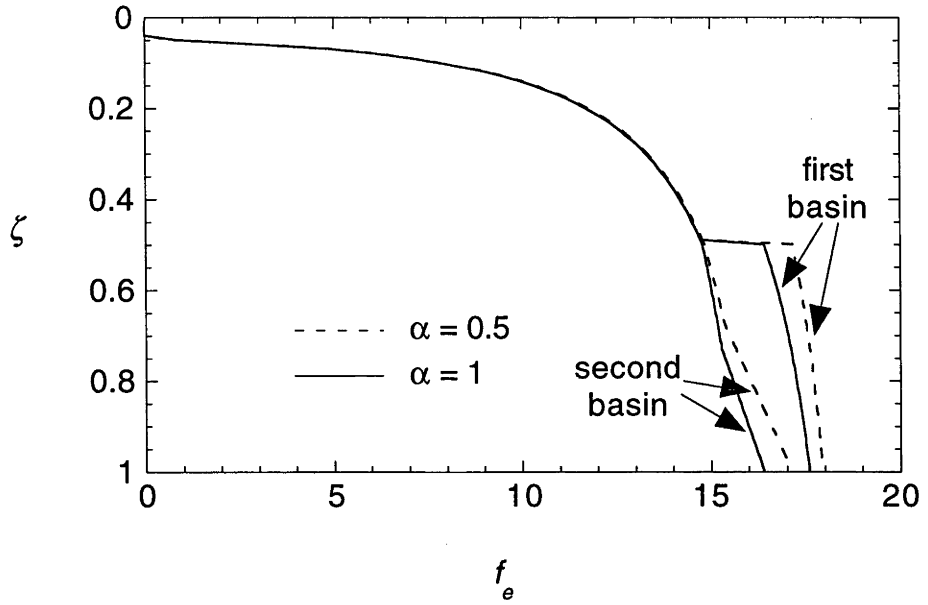

b)

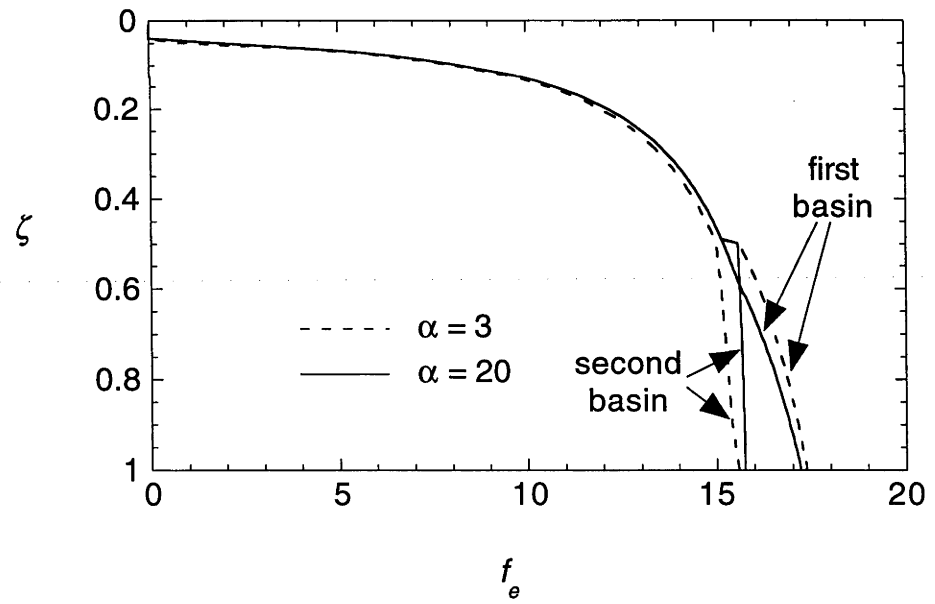

Figure 7.14. The environment buoyancy profiles for $\zeta_s = 0.5$ and $\Phi = 0.25$ when the first front is at $\zeta = 0.05$. (a) $\alpha = 0.5$ and 1. (b) $\alpha = 3$ and 20.

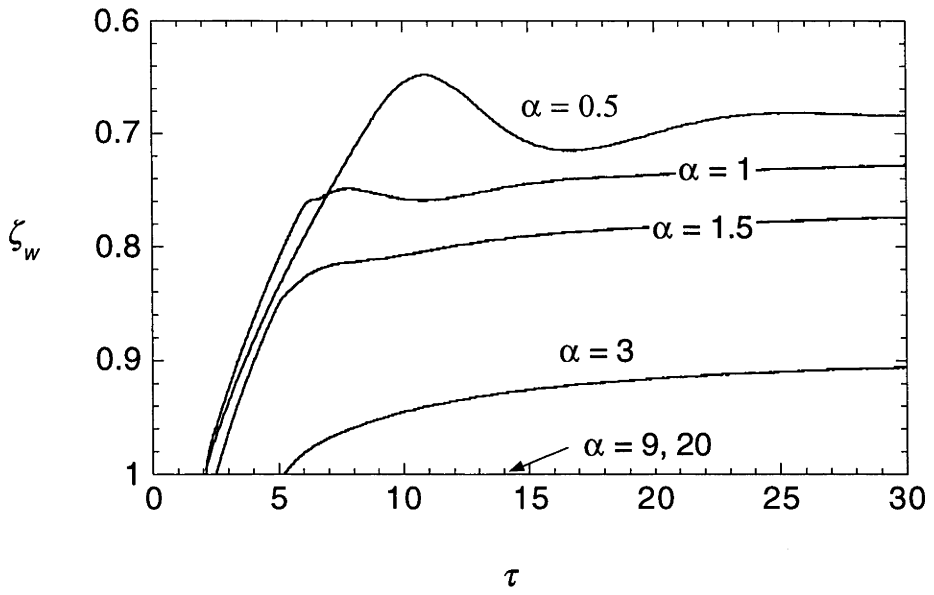

Figure 7.15. The neutral buoyancy level of the weak plume ζ_w for ζ_s = 0.5, Φ = 0.25 and α = 0.5, 1, 1.5, 3, 9 and 20.

7.5 Discussion and Conclusion

The model presented in this chapter shows that modifications to the properties of the plume and environment result when the lower depths of the filling-box are divided by a ridge into two basins. The ridge causes plume outflows to be collected separately in the two basins, often producing waters with very different densities in each. In addition, as ridge heights increase, more restriction on the inter-basin exchange is imposed through deeper basins so that not only are density differences between the two basins larger, but also the time required to evolve to the steady state.

For a single plume descending into a two-basin system, the properties depend on whether the size of the second basin (without the plume) is infinite or not. The homogenous first basin that forms when the second basin is infinite is similar to studies of "ventilated filling-box" models of Linden et al. (1990) and of convection produced by buoyancy sources in enclosures (Cooper and Linden, 1996; Linden and Cooper, 1996). In the "ventilated filling-box" model, openings at the top and bottom allow water to enter and exit the box. In that study, the exchange of water is limited by the size of the openings and a single plume was found to create a two layered environment within that

box. In the single plume two-basin system where the second basin is infinite, the first basin, together with part of the common region directly above it, may be considered a "leaking" or "quasi-ventilated" filling-box. Water leaves this "quasi-ventilated" filling-box through the overflow and enters it by way of entrainment into the plume above the ridge. Both exchanges are limited in volume (ultimately by the plume volume flux entering the first basin) and hence it is not surprising that a two layered system, in the form of homogenous regions above and below the ridge, is also generated.

On the other hand, if the second basin is finite, then there is no complete ventilation of the first basin because the overflowing water fills up the second basin, advects into the common region and returns to the first basin through entrainment into the plume. This convection cycle through the system is comparable to that of the single-basin filling-box. Above the ridge, the large-time stratification is virtually identical to the single-basin system. Below the ridge, the newest plume outflow water, which is also the densest water in the environment, is now found in the first basin while slightly less dense water is found in the second basin. A similar system is also formed when there are two plumes, one descending into each basin. The spreading depth of the weak plume is modified from the single-basin case and also depends on the relative cross-sectional areas of the two basins and the ridge height.

With experiments in §7.4 providing general agreement with the theoretical results for the density structure of the environment, spreading depths of the weak plume and direction of overflows across the sill, it is anticipated that experimental verification will extend to all the theoretical results. However, there will be some important differences in any application of the theory. As in chapter 6, the mid-depth intrusions of plumes and overflows are often lower than the neutral buoyancy level. They are also influenced by background horizontal motions such as those generated by shear layers. Furthermore, the water in the overflowing basin may rise to some distance above the sill before spilling into the other basin (the overflow has finite depth). The dynamics of the overflow, such as its thickness, are also determined by hydraulic control and should be incorporated into the numerical scheme for use in specific applications.

Chapter 8

Conclusions

This thesis has presented theory and experiments designed to investigate the fundamental processes in turbulent plume convection and the resulting stratification and circulation in enclosed boxes. The interest for this work stems from its potential relevance to convection and stratification in the oceans. The major conclusions are:

(i) Counterflowing shear layers result when the outflow from a turbulent plume spreads in a stratified environment. These shear layers are established by the continuous excitation of baroclinic normal modes and have vertical scales set by the depth of the outflow layer. In the non-linear stratification produced by the "filling-box" process, viscous dissipation of momentum causes the amplitudes of the horizontal velocities in the shear layers to decrease with distance from the bottom.

(ii) An analysis is presented for turbulent plumes on slopes. The properties of downslope plumes, when averaged over their cross-section, depend similarly on the distance from the source as do those of vertically-descending plumes far from side boundaries. However, the rate of entrainment of surrounding water is reduced and depends on the angle of the slope.

(iii) Where the downslope plume forms a highly turbulent flow down a steep slope, the convective circulation and stratification generated are similar to those produced by a vertically-descending plume. Under such conditions, "filling-box" models for downslope plumes may be assumed to be forced by equivalent vertically-descending plumes.

(iv) When two well-separated plumes fill a single basin, the spreading depth of the weak plume at large times is roughly dependent on the two-thirds power of the ratio of buoyancy fluxes between the two sources. However, the overall stratification in the basin

is similar to that produced by a single plume from a source with the combined flux.

(v) Where a number of plumes descend into a single basin, shear layers are mainly forced by the outflow of the strongest plume. The spreading paths of intermediate-depth outflows from weaker plumes are strongly modified by their passive advection in the horizontal velocities of the shear layers.

(vi) When a filling-box is divided by a ridge into two basins, convection is restricted by the topography. Density differences between the two basins build up and result in overflows across the ridge. The modifications to the stratification and plume spreading depths increase with the height of the ridge and also depend on the relative horizontal areas of the two basins.

More research is required in establishing the differences in the "filling-box" circulation between downslope plumes and vertically-descending plumes. The experiments suggest that plumes on very gentle slopes lead to "detrainment" and the formation of very dense bottom layers. It is suggested that this is caused by insufficient mixing over the vertical cross-section of the plume. Further knowledge on the mixing processes and density distribution within downslope flows will assist investigations of the circulation patterns driven by such currents. In any application of the model, the precise mixing processes and density distribution in the flow may also influence the circulation patterns. For example, complex bottom topographies and rotation of the earth alter the course and velocity of currents in the oceans and will therefore influence the properties of the flow.

The "filling-box" models presented in this thesis may also be relevant to the circulation of the oceans and semi-enclosed seas. The shear layers of chapter 4 were observed in rectangular basins and were generated primarily by the outflow of the strongest plume. The lateral dispersion of outflows from weaker plumes was shown to be affected by these shear layers and only slightly modify the overall horizontal velocity structure. Should similar counterflowing shear layers be generated in the oceans by bottom and deep water convection, a direct extrapolation of the present results would imply that horizontal velocities at all depths are mainly forced by the largest outflows of

dense water in the deep ocean. However, further work would be necessary to determine the circulation patterns in basins with complex ocean-like topographies. For example, observations of circulation patterns in the two-basin filling-box of chapter 7 would reveal some of the effects of sills and mid-ocean ridges. However, in the oceans there are other processes that have not been included here, such as the effects of the earth's rotation, and these are also expected to be significant.

Another possible extension to the "filling-box" theory is a generalised multiple plume model where each plume descends slopes of different angles. This model would assist investigations of the convection where different rates of mixing and entrainment occur in different plumes. In these situations it is anticipated that modifications to the plume properties will result in slightly altered spreading depths and circulation patterns. For the oceans, rotation will once again play a role in directing flows along slopes at an angle from the downslope direction and will therefore alter the amount of entrainment from each depth interval and change the neutral buoyancy level.

The theory of multi-basin filling-boxes may also be applicable to marginal seas, where dense water is collected in basins and drained into oceans through sill overflows. Knowledge of the convection and inter-basin exchange in these systems will extend understanding of the processes involved in the production of dense water in a number of regions including the Mediterranean Sea and Arctic Ocean. However, the collection and interpretation of suitable field data sets is a large task and beyond the aims of this thesis. Seasonal buoyancy sources may also be imposed on the forcing of such systems, further modifying the stratification and resulting in time dependent exchanges between basins.

In summary, this study has identified that active shear layers are an integral part of the "filling-box" circulation produced by both vertically-descending and downslope plumes. It has also been shown that the plume properties and the environment stratification can be calculated for a number of plumes descending in multi-basin geometries. The results presented in this thesis provide useful insights into some of the important processes that may contribute to the deep ocean stratification and to buoyancy-driven flows between basins.

References

ACHESON, D.J. 1990. *Elementary Fluid Dynamics*. Oxford University Press, 397pp.

BAINES, P.G. 1995. *Topographic Effects in Stratified Flows*. Cambridge University Press, 482pp.

BAINES, P.G. 1997. Downslope flows into a stratified environment - structure and detrainment. *Proceedings of 5th IMA Conference on Stratified Flows. Dundee, September 1996.* Editor: P.A. Davies. Institute of Mathematics and its Applications.

BAINES, W. D. and TURNER, J. S. 1969. Turbulent buoyant convection from a source in a confined region. *J. Fluid Mech.*, **37**: 51-80.

BATCHELOR, G.K. 1967. *An Introduction to Fluid Dynamics*. Cambridge University Press, 615pp.

BRETHERTON, F.P. 1967. The time-dependent motion due to a cylinder moving in an unbounded rotating or stratified fluid. *J. Fluid Mech.*, **28**: 545-570.

BRITTER, R.E. and LINDEN, P.F. 1980. The motion of a front of a gravity current travelling down an incline. *J. Fluid Mech.*, **99**: 532-543.

CARDOSO, S.S.S., and WOODS, A.W. 1993. Mixing by a turbulent plume in a confined stratified region. *J. Fluid Mech.*, **250**: 277-305.

COOPER, P. and LINDEN, P.F. 1996. Natural ventilation of an enclosure containing two buoyancy sources. *J. Fluid Mech.*, **311**: 153-176.

EMMS, P.W. 1997. Streamtube models of gravity currents in the ocean. *Deep-Sea Res.*, **44**: 1575-1610.

ELLISON, T.H. and TURNER, J.S. 1959. Turbulent entrainment in stratified flows. *J. Fluid Mech.*, **6**: 423-448.

GILL, A.E. 1982. *Atmosphere-Ocean Dynamics*. Academic Press, 662pp.

GERMELES, A.E. 1975. Forced plumes and mixing of liquids in tanks. *J. Fluid Mech.*, **71**: 601-623.

IMBERGER, J., THOMPSON, R. and FANDRY, C. 1976. Selective withdrawal from a finite rectangular tank. *J. Fluid Mech.*, **78**: 489-512.

KAWASE, M. 1987. Establishment of deep ocean circulation driven by deep-water production. *J. Phys. Ocean.*, **17**: 2294-2317.

KAWASE, M. and STRAUB, D. 1991. Spinup of source-driven circulation in an abyssal basin in the presence of topography. *J. Phys. Ocean.*, **21**: 1501-1514.

KILLWORTH, P.D. 1977. Mixing on the Weddell Sea continental slope. *Deep-Sea Res.*, **24**: 427-448.

KILLWORTH, P.D. 1979. On "chimney" formations in the ocean. *J. Phys. Ocean.*, **9**: 531-554.

KILLWORTH, P.D. 1983. Deep convection in the world ocean. *Rev. Geophys. Space Phys.*, **21**: 1-26.

KILLWORTH, P.D. and TURNER, J.S. 1982. Plumes with time-varying buoyancy in a confined region. *Geophys. Astrophys. Fluid Dyn.*, **20**: 265-291.

LEVITUS, S. 1982. *Climatological Atlas of the World Ocean.* NOAA Professional Paper No. 13., U.S. Government Printing Office.

LIGHTHILL, J. 1978. *Waves in Fluids*. Cambridge University Press, 504pp.

LINDEN, P.F. and COOPER, P. 1996. Multiple sources of buoyancy in a naturally ventilated enclosure. *J. Fluid Mech.*, **311**: 177-192.

LINDEN, P.F., LANE-SERFF, G.F. and SMEED, D.A. 1990. Emptying filling boxes: the fluid mechanics of natural ventilation. *J. Fluid Mech.*, **212**: 309-355.

MAGNELL, B. 1976. Salt fingers observed in the Mediterranean Outflow region (34°N, 11°W) using a towed sensor. *J. Phys. Ocean.*, **6**: 511-523.

MANINS, P.C. 1976. Intrusion into a stratified fluid. *J. Fluid Mech.*, **74**: 547-560.

MANINS, P.C. 1979. Turbulent buoyant convection from a source in a confined region. *J. Fluid Mech.*, **91**: 765-781.

MARTIN, S. and LONG, R.R. 1968. The slow motion of a flat plate in a viscous stratified fluid. *J. Fluid Mech.*, **31**: 669-88.

MOWBRAY, D.E. and RARITY, B.S.H. 1967. A theoretical and experimental investigation of the phase configuration of internal waves of small amplitude in a density stratified liquid. *J. Fluid Mech.*, **28**: 1-16.

MORTON, B.R., TAYLOR, G.I. and TURNER, J.S. 1956. Turbulent gravitational convection from maintained and instantaneous sources. *Proc. R. Soc. Lond. A*, **234**: 1-23.

NEAL, V.T., NESHYBA, S. and DENNER, W. 1969. Thermal Stratification in the Arctic Ocean. *Science*, **166**: 373-374.

PEIXOTO, J.P. and OORT, A.H. 1992. *Physics of Climate*. American Institute of Physics, 520pp.

PIERCE, D.W. and RHINES, P.B. 1996. Convective building of a pynocline: laboratory experiments. *J. Phys. Ocean.*, **26**: 176-190.

PRANDTL, L. 1952. *Essentails of Fluid Dynamics*. Blackie.

PRICE, J.F. and O'NEIL-BARINGER, M. 1994. Outflows and deep water production by marginal seas. *Prog. Ocean.*, **33**: 161-200.

PRICE, J.F., O'NEIL-BARINGER, M.T., LUECK, R.G., JOHNSON, G.C., AMBAR, I., PARRILLA, G., CANTOS, A., KENNELY, M.A. and SANFORD, T.B. 1993. Mediterranean Outflow mixing and dynamics. *Science*, **259**: 1277-1282.

ROBINSON, A.R. and STOMMEL, H. 1959. The oceanic thermocline and the associated thermohaline circulation. *Tellus*, **11**: 295-308.

ROUSE, H., YIH, C.S. and HUMPHREYS, H.W. 1952. Gravitation convection from a boundary source. *Tellus*, **4**: 201-210.

RUDDICK, B.R. and SHIRTCLIFFE, T.G.L. 1979. Data for double diffusers: physical properties of aqueous salt-sugar solutions. *Deep-Sea Res.*, **26**: 775-787.

SCHMITT, R.W. 1994. Double diffusion in oceanography. *Ann. Rev. Fluid Mech.*, **26**: 255-285.

SEND, U., FONT, J. and MERTENS, C. 1996. Recent observation indicates convection's role in deep water circulation. *EOS*, **77**: 7.

SMITH, P.C. 1975. A streamtube model for bottom boundary currents in the ocean. *Deep-Sea Res.*, **22**: 853-873.

SQUIRES, P. and TURNER, J.S. 1962. An entraining jet model for cumulonimbus updraughts. *Tellus*, **14**: 422-434.

STOMMEL, H. 1958. The abyssal circulation. *Deep-Sea Res.*, **5**: 80-82.

STOMMEL, H. and ARONS, A.B. 1960. On the abyssal circulation of the world ocean - II. An idealized model of the circulation pattern and amplitude in oceanic basins. *Deep-Sea Res.*, **6**: 217-233.

THORPE, S.A. 1968. On standing internal gravity waves of finite amplitude. *J. Fluid Mech.*, **32**: 489-528.

TURNER, J.S. 1973. *Buoyancy Effects in Fluids*. Cambridge University Press, 368pp.

TURNER, J.S. 1980. Differentiation and layering in magma chambers. *Nature*, **285**: 213-215.

TURNER, J.S. 1986. Turbulent entrainment: the development of the entrainment assumption, and its application to geophysical flows. *J. Fluid Mech.*, **173**: 431-471.

TURNER, J.S. 1997. G. I. Taylor in his later years. *Annu. Rev. Fluid Mech.*, **29**: 1-25.

WARREN, B.A. 1981. Deep circulation of the world ocean. *Evolution of Physical Oceanography - Scientific Surveys in Honor of Henry Stommel.* Editors: B.A. Warren and C. Wunsch, MIT Press, 623pp.

WHITEHEAD, J.A. 1989. Giant ocean cataracts. *Sci. Amer.*, **260**: 50-57.

WORSTER, M.G. and HUPPERT, H. E. 1982. Time-dependent density profiles in a filling box. *J. Fluid Mech.*, **132**: 457-466.